THE STATIC AND DYNAMIC STABILITY OF CLAMPED SHALLOW CIRCULAR ARCHES

Thesis by

Man Cheong Cheung

In Partial Fulfillment of the Requirement
For the Degree of
Doctor of Philosophy

California Institute of Technology
Pasadena, California
1969

ACKNOWLEDGMENT

The author is deeply indebted to Dr. C. D. Babcock, Jr. for guidance and encouragement received during the course of this investigation. The valuable suggestions of Dr. E. E. Sechler are gratefully acknowledged.

Appreciation is expressed for the help received from Mr. George Carlson of the Aeronautics Shop, Mr. Marvin Jessey of the Electronics Laboratory. Very much appreciated was the help of Miss Helen Burrus for the typing and of Mrs. Betty Wood for the graphs and figures.

This study was supported by the Air Force Office of Scientific Research, Office of Aerospace Research, United States Air Force under Grant No. AFOSR 68-1424. The financial aid of a GALCIT Fellowship is also deeply appreciated.

ABSTRACT

An experimental investigation of the relationship between the dynamic buckling and the static buckling phenomenon was carried out.

The first half of the paper studies the stability of shallow arches subjected to lateral forces. Concentrated static and step loads were applied to circular arches with geometric parameters $7 < \gamma < 20$. Equilibrium path and the dynamic response at the loading position were recorded. Dynamic buckling is distinct. Supercritical and subcritical responses were separated by 0.5 °/o of the total load. The sensitivity of the arch to loading imperfection was studied. The effect was pronounced in the static tests but moderate in the dynamic responses.

The second half of the paper studies the response of clamped circular arches under lateral impulse. The motion of the arch was recorded by a high speed camera and the deflected arch shape was measured in detail. The response was expressed in terms of the average displacement and three generalized displacement coordinates representing the amplitudes of the assumed mode shapes. The critical impulse is defined as the impulse level at the inflection point of the curve of maximum response versus impulse.

NOMENCLATURE

A	Cross sectional area of the arch (in^2)
b	Arch width (in)
E	Young's Modulus (psi)
h	Arch thickness (in)
H	Central arch rise (in)
I	Specific impulse ($lb\text{-}sec/in^2$)
I_m	Moment of inertia (in^4)
$\overline{I}$	Nondimensional impulse $= \frac{4I^2R^2}{h^4E\rho}$
L	Arch length (in)
ΔL	Distance between load and center of arch (in)
P	Concentrated load (lb)
$\overline{P}$	Nondimensional load $= \frac{P(\frac{L}{2})^3}{4EI_m}(\frac{A}{I_m})^{1/2}$
q_1, q_2, q_3	Generalized displacement coordinates
R	Arch radius (in)
t	Time (sec)
W	Arch displacement (in)
W^a	Nondimensional average displacement
W_e	Weight of explosive (gm)
α	Arch coordinate (radians)
β	Arch half angle (radians)
γ	Geometric parameter $= \frac{L^2}{4Rh}$
ϵ	Percentage of eccentricity $= \frac{\Delta L}{L}$
ρ	Mass density ($slug/in^3$)

NOMENCLATURE (Cont'd)

Subscripts:

CR	Experimental critical value
CL	Classical theoretical value
MAX	Maximum value

TABLE OF CONTENTS

LIST OF TABLES

LIST OF FIGURES

LIST OF FIGURES (Cont'd)

Figure Page

LIST OF FIGURES (Cont'd)

I. INTRODUCTION

A prominent scientist, Kirchhoff, once said that "Dynamics" is a science of motion and forces. Thus dynamics includes statics which deals with the state of equilibrium. This relationship stimulated this research work. It is focused on the understanding of the dynamic buckling phenomenon of nonlinear structures as related to their static buckling.

The static stability of cylindrical and spherical shells was studied intensively not long after the invention of the airplane. However, the experimental results had considerable scatter and were only 30-50 °/o of the classical buckling load* (Ref. 1) for some loading conditions. Tsien (Ref. 2) proposed an energy criterion** which seemed to be in better agreement with the experiments. However, to achieve buckling at the load given by the energy criterion, a perturbation of unspecified magnitude is required. But how and where to apply this perturbation is not prescribed. Therefore, this criterion is believed to be built on an unsound basis. In the past few years,

---

* The classical buckling load of a shell is defined as the lowest eigenvalue of the linearized theory. The linearized theory is derived by perturbing the nonlinear equations of the perfect shell about a membrane prebuckling equilibrium state. For the arch problems which will be considered later, the exact solution of the nonlinear equations is the classical solution. The critical condition is reached when either the equilibrium path yields a local maximum of the loading parameter or the path bifurcates into additional branches.

** The buckling load is reached when the total energy in a possible equilibrium state is equal to the total energy in the unbuckled state.

experimental techniques have improved. Experimental results for cylindrical shells under axial compression are closer to the classical solution than to the energy solution (Ref. 3). On the other hand, if initial geometric imperfections are included in the analysis, the experimental buckling loads can be predicted reasonably well (Ref. 4).

The classical analysis and the energy criterion were also applied to other nonlinear structures. Fung and Kaplan (Ref. 5) found that the classical solution compares well with experiments on simply supported arches. Gjelsvik and Bodner found that the experimental results for the clamped shallow arch subjected to a concentrated load lie in between the two theories (Refs. 6 and 7). To confirm this point, similar tests were performed in this investigation.

The problem of dynamic buckling or nonlinear response of shell structures has been widely discussed in the past few years. The question of dynamic buckling is of concern since this phenomenon is associated with a large change in the structural response with a small change in the loading conditions. This change of response character with load is similar to the stability problem of static loading and hence the name dynamic buckling has often been adopted. However, since the loading and response are functions of time, the analogy is not quite complete. This has led to a variety of definitions of dynamic buckling. The definition of stability used here is not in the conventional sense of a bounded or unbounded motion. It should be stated as a finite increase of maximum response due to an infinitesimal increase of the loading parameter. No matter how small this discontinuity may be, as long as it exists, the load level at which it occurs is defined as the dynamic buckling load.

The differential equations that govern the motion of the shell structures are time dependent and nonlinear. The exact solution of these equations is the counterpart of the static classical analysis. However, to solve these hyperbolic nonlinear equations is not an easy matter. No exact solution has been obtained so far for those structures of interest. Numerical integration of the equations seems to be the only alternative. Specifying the initial values for the structure, the type of loading and the boundary conditions, the differential equation can be integrated with various schemes. Due to the nature of the equations, the convergence of most schemes is a serious matter. The stability of the integration error should be investigated thoroughly before the results become trustworthy. The computation time is another major problem. Iterations are necessary for each time step and space coordinate. Depending on the complexity of the structure, the computation time may vary from moderate to enormous.

For these apparent reasons, one is inclined to use the much simpler energy approach. Although the energy criterion lost its influence in static stability studies, under some loading conditions, the extended energy analysis is very convenient in the analysis of the dynamic response (Refs. 8-11). Unfortunately, there has been no experimental data to compare with these analytical results. Therefore, some step loading and impulsive loading experiments were carried out. The shallow arch was chosen as a model because this simple structure has nonlinear characteristics similar to much more complicated shell structures. A wide range of this nonlinear behavior can be exhibited by changing the end conditions, loading, or geometry of the arch.

The energy method is built up by using the static equilibrium states. Knowing the static response, one can derive some of the interesting features of the dynamic response. Let us start with the simplest example. Figure 1 shows the response of a linear spring mass system. The amount of force applied to the mass is P and q is the displacement of the mass. On the force-displacement diagram, a linear static equilibrium path OA is traced. If the force is applied as a Heaviside step function, the response will be a simple harmonic motion around the static equilibrium position. The dynamic response is illustrated at two load levels P_D and P_E. The dotted lines along the time axis are the corresponding equilibrium positions. In this case, the maximum dynamic response is twice the static response. This is shown as the straight line OEDB.

The relationship of the static and dynamic response can be clarified by the potential energy (U) of the system. The potential energy is a function of the external load and the displacement. It can be decomposed into two parts. The first part is the strain energy stored in the spring. This strain energy is proportional to the square of the displacement, and is always positive. The second part is the potential of the external load. This term is linearly proportional to the displacement and is negative for positive displacement. For small deformation, the second term dominates and the total potential energy decreases until a minimum is reached which corresponds to the stable static equilibrium position. There are two energy curves shown for

P_E and P_D. The dynamic response is analogous to a ball rolling along these energy curves. If no energy is dissipated or supplied during the course of oscillation, the ball will rise to a position of the same elevation as the initial position and oscillates thereafter. Therefore, positions E and D are the maximum dynamic responses at the step load level P_E and P_D respectively.

Next, we consider a nonlinear one degree of freedom system. Assume the static load deflection curve has the form OABC as shown on Figure 2a. OA and BC represent stable branches while the AB branch is statically unstable under dead weight loading. Starting at the origin, with half the initial slope, the maximum dynamic response is shown by the dotted line. Influenced by the softening nonlinearity, the curve extends with ever-lessening slope. The intersection of this curve with the branch AB is significant, because this determines the unique position at which the arch snaps under step load. This statement will be proved by using the potential energy curves (Figure 2b).

Point D is a local maximum in the energy curve because it is on the AB branch. This local maximum has zero potential energy since point D is on the maximum dynamic response curve. Hence, if a ball rolls along the energy curve corresponding to $P = P_D$, it takes an infinite amount of time to arrive at the static equilibrium position D. Should the load be increased infinitesimally, the energy of the local maximum will drop below zero and the ball will cover an additional territory. P_D is therefore defined as the critical load.

The response histories at a supercritical and subcritical load level are illustrated at the left part of Figure 2a where time is plotted as the third axis perpendicular to the P-q_1 plane. The supercritical response has a bell shape curve since the kinetic energy is low when the response crosses the local maximum of the energy curve. Thus the system moves slower through such a range.

When a two degrees-of-freedom system is considered, the potential energy can no longer be expressed as a single curve, but as a continuous surface. On a surface, one can move from one point to another along an infinite number of paths. Therefore, the energy method fails to yield a unique critical condition. The alternative is to obtain necessary or sufficient conditions for the lower and upper bounds respectively. This is illustrated by Figure 3. A typical three-dimensional static equilibrium path is shown on the left part of Figure 3a. The elliptic path between A and B represents the bifurcated branch which is on a plane perpendicular to the POq_1 plane. The maximum dynamic response is shown as OED. Three energy surfaces for load levels between P_A and P_B are shown in Figure 3b, c, d. These surfaces have five equilibrium positions: the center one is unstable (hill), the left and right ones are stable (depression), and the upper and lower ones are unstable (saddle). It is again easier to visualize the dynamic response by using the analogy of the motion of a ball on the energy surface. Figure 3b shows the energy surface at $P = P_D$. The local maximum D has zero energy. If the response is restricted to the q_1 component, the ball will take an infinite amount of time to arrive at D. Should the load be increased infinitesimally, the local maximum has negative potential energy and all interior points bounded by $U = 0$ have $U < 0$. With a little higher energy, the ball can leap over the local maximum and gets to the far side of the region. This sudden increase of response entitles P_D to be the upper critical load.

The energy surface for $P = P_E$ is shown in Figure 3c. The domain $U \leq 0$ becomes doubly connected. If the response is restricted to the q_1 component, the ball can not reach the far side of the region. Hence, P_E is not significant. The lower bound for the load, using this energy method is shown in Figure 3d where the energy at the saddle points is zero. An infinitesimal increase of the load decreases the energy at the saddle points below zero and allows the ball to roll over to the far side through one of the two saddle points.

With the above concept in mind, a generalization to a multiple degree-of-freedom system is straightforward. At each load level, the multiple dimensional energy surface is examined. The lower bound will be determined by a load such that the first static equilibrium position appears in the zero potential energy surface. The upper bound will be defined at a load level where the potential energy of all local maximums is below or equal to zero.

So far, the upper bound is clearly defined provided the static critical load is higher than P_D. If this is not satisfied, the static critical load will be the governing upper bound. At such a load level, two saddle points merge with the near stable equilibrium position and convert this stable position to another saddle point. This conversion of an equilibrium position makes all points on the left of the local maximum unstable. A perturbation of any magnitude causes the ball to diverge from the q_1 axis, to by-pass the hill and finally to arrive at the far stable region. This bound is named by Simitses as the "Minimum Guaranteed Critical Load".

Furthermore, necessary or sufficient conditions discussed earlier are for elastic structures without damping. Should damping be present, the picture would be a little different. The estimation of the necessary condition is not affected because energy is needed to account for dissipation. If the undamped system can not escape from the near stable region, it is reasonable to think that the damped system also will not escape. However, the sufficient condition must be reconsidered. The upper bound for the undamped system would be an under-estimated upper bound for the damped system. As a matter of fact, the energy dissipated is a function of the dynamic path and thus depends on the initial conditions. An upper bound similar to the undamped case seems to be meaningless unless one can find a descending path on the energy surface that connects the original position to the far stable region. This is exactly the case for the static critical load as discussed in the previous paragraph. Therefore, the static critical load is the upper bound for the damped system.

The experiments were carried out with many objectives. The static tests were to confirm Gjelsvik and Bodner's experiments and to compare with the analyses. The step loading tests supplied data for comparison with the results obtained by the numerical integration of the nonlinear differential equation (Ref. 12) and the results from the energy analysis (Ref. 9). The sensitivity of the arch to loading imperfections was studied. Finally, a valuable by-product of the experiment showed the non-existence of other stable equilibrium positions upon total removal of external load. The non-existence of these positions does not allow an impulsively loaded clamped arch to be classified as a stability problem in the strict mathematical sense.

The experiments were divided into three sets. The first set was concerned with the static buckling of clamped circular arches subjected to concentrated loads. The second set extended the first set to include a step function load. The last set considered a uniformly distributed impulsive load. Although the first two sets are different in nature, they used similar equipment and were performed with identical specimens. They will be presented together in Part II. The impulsive load experiments are presented in Part III.

II. STABILITY OF CLAMPED SHALLOW CIRCULAR ARCHES UNDER STATIC CONCENTRATED LOADS AND STEP CONCENTRATED LOADS

Four arches with geometric parameters $\gamma = \frac{L^2}{4Rh}$ of approximately 7, 11, 14 and 18 were used in the tests. The load was applied at various locations on the arch. Although the entire deformed arch shape was not measured, the displacement at the loading point was recorded. The combination of the static response and the maximum dynamic response gives a clearer picture of the buckling phenomenon.

A. Experiment

The experimental set up used for static loading is similar to the one used by Gjelsvik and Bodner (Ref. 6). The step load was developed by suddenly releasing a dead weight which initially touched the arch surface. However, the inertia of the dead weight changed the effective force on the arch and in turn affected the frequency and magnitude of the response. In fact, it was detected that the load detached from the arch during the first few cycles. The effect of inertia was reduced by placing a very soft spring between the arch and the weight. The softer the spring, the longer the initial stretch which may be much larger than the response of the arch. With this arrangement, it was found that the variation in load was less than 10 $^{\circ}/\mathrm{o}$ of the total dead weight. The large variation occurred after the arch buckled, thus its affect was small on the determination of the critical load.

1. Test Specimens

The equations that describe a shallow arch show that the circular arch can be characterized by one nondimensional parameter γ (Figure 4) where

$$\gamma = \frac{L^2}{4Rh} = \frac{\beta^2 R}{h}$$

The three variables are length, thickness and radius of curvature. For all of the arches tested, the thickness was held constant and the same nominal radius of curvature was used.

The specimens were cut from 1/16 inch thick 2024 T3 aluminum sheet, and were trimmed by the milling machine to 3/4 inch wide. The strips were then rolled to approximately 30 inches radius in a three-roll roller. The radius was rough checked using a template. After rolling, 4 inches from both ends were cut off. The arches were then heat treated for eight hours at 375 degrees Fahrenheit.

Straight tensile specimens were tested in an Instron testing machine. Young's Modulus was found to be 10.5×10^6 lb/in^2 and the proportional limit above 46,000 lb/in^2. Curved tensile specimens with a radius of 30 inches were similarly tested and the results were much the same. A typical tensile test of a curved specimen is shown in Figure 5.

The arches were mounted into a heavy steel frame for testing. The ends are secured using Devcon B. An arch mounted in the frame is shown in Figure 6. The geometry of the tested arches can be found in Table I.

2. Experimental Setup

Except for the recording system, both the static and dynamic tests used the same equipment as explained below. A schematic drawing of the setup is shown in Figure 7. A description of each item marked by a letter is as follows.

a. Aluminum Arch

The center line and eccentricity lines were marked on the convex side of the arch surface.

b. Steel Support for the Arch

This support could be moved to the left or right in order to position the point of loading directly under the knife edge.

c. Knife Edge Assembly

Through a retractable pin, the knife edge was hung on a support shown in Figure 8. The whole assembly could be moved up and down so that the knife edge was just touching the arch surface before performing the test. After adjusting the elevation, the support was locked in position. The retractable pin was connected to a solenoid. When the circuit was closed, the solenoid pulled the pin back and the weight carried by the knife edge could be transferred to the arch. For static tests, the knife edge was disengaged from the pin manually and was gently set on to the arch. The hanging weight accounted for the initial load.

d. Displacement Transducer

The housing of the transducer was fixed to the stationary part, while the sliding core was connected to the top of the knife edge (see Figure 8). As the knife edge moved with the arch, the transducer measured the vertical displacement at the loading point.

The calibration of this transducer was linear with a working range of 3". By adjusting the control, the output was 100 MV per inch of the displacement.

e. Tension Spring

The spring is connected to the bottom part of the knife edge. In static tests, it serves as a safety device to avoid breakage of the fragile load cell due to excessive displacement from below. It was changed to a very soft spring for dynamic tests for reasons mentioned previously.

f. Load Cell

The load cell was a 0.010" thick Mylar tensile specimen. The strip was 1.25" wide and 6.5" long. Two SR-4 paper strain gages were placed in series on each side of the Mylar strip as active gages. The same number of dummy gages were placed on the same strip and were perpendicular to the active ones. The gages were supplied by a 12V D. C. power supply. The working range corresponded to about one quarter of the ultimate stress of Mylar. The calibration was linear and gave 0.493 MV output per pound weight. On top of the initial load, this gave the total applied load for the static tests. In the dynamic tests, the load cell measured the variation of the effective load as a function of time.

g. Dead Weight

This was the main difference in the arrangement between the dynamic and static tests. For the former one, a pot of weight was hung to the load cell and the weight was the last in the series. In static tests, the weight rested on a hydraulic jack and was fastened to the load cell by a nylon cord.

h. Hydraulic Jack

The hydraulic jack was used for the static tests. It worked as a moving platform for the weights. At the beginning of the test, the piston was brought to the upper most position. When the valve was opened the piston sank slowly. In the process of loading, the load regulated automatically with the displacement. Thus this arrangement established itself as a "near rigid machine" and was able to map the unstable branch of the equilibrium path.

The recording system used in the static tests was an X-Y plotter. Without using an amplifier, the output from the displacement transducer was connected to the X axis, while the output from the load cell went to Y axis. The result was a single load deflection curve representing the equilibrium path.

A Honeywell Visicorder (Model 1508) was used to record the dynamic response and the variation of the effective load. The outputs were amplified three and one hundred times respectively for the displacement transducer and the load cell. Inside the Visicorder, Honeywell galvanometers were used in recording oscillographs to transfer voltage variations to a photographic record. The oscillographs were recorded on Kodak extra thin Linagraph Direct Print paper (Type 1799).

3. Test Procedure

There were three main steps in the complete testing of an arch. Namely, they were an initial imperfection measurement, a quasi-static test and a dynamic test. Arches were reusable. They were reloaded at different locations, including from 0 °/o up to 6 °/o offset from the center. This gave the reduction of critical load due to an eccentric load. In between tests, imperfections of the arch shape were measured in order to assure that the arch was not subjected to excessive plastic deformation.

To obtain results with high accuracy, the dynamic tests were to be performed following the static test at the same loading location. However, repeated tests showed that the response characteristics were reproducable and were little influenced by the order of testing. In fact, after approximately one hundred tests on the same arch, the critical load remained within 2 °/o. Therefore, to simplify the

the testing procedures, static tests were carried out for all loading positions and were followed by the dynamic tests.

In static tests, the critical load was defined as the local maximum of the loading parameter on the equilibrium path. However, in the dynamic tests, the critical load could not be determined by only one test. Different load levels were applied to the arch. Slightly increased amplitude of vibration resulted from a small increase in load. At a critical load, the maximum amplitude increased abruptly.

a. Initial Imperfection Measurement

A pendulum like apparatus was built to measure imperfections of the arch. It consisted of a fixed center and rotatable arm which could be adjusted in length. A dial gauge with a working range of 0.060 inches was installed at the tip of the arm (see Figures 9 and 10).

The measurement was made by first adjusting the arm to the appropriate radius then pressing the concave side of the arch gently against the dial gauge. Starting from one end of the arch the dial gauge readings were taken at half inch intervals along the arch until the dial gauge could not advance another full step. This gave the deviation of the arch shape from the preset radius. Applying the "Least Square Method" to the measured data the "best fit radius" and the "best fit imperfection" can be found. The derivation of the equations to accomplish this can be found in Appendix I.

Before the arches were mounted on the supports the imperfections were measured. Only those arches with imperfection amplitudes less than five thousandth of an inch were used. Also, they were cut from longer ones so that the selected sections had a minimum amount of asymmetric imperfection. When the arch was mounted and the Devcon was hardened, the arch shape was measured again to make sure that it had not been excessively deformed due to the process of mounting. The imperfections of the tested arches are shown in Figure 11.

b. Static Test

The arch was put into the knife edge assembly such that the loading position was directly under the edge. The assembly was lowered so that the edge just touched the arch surface. At this point, the output from the displacement transducer represented zero displacement of the arch. When this was recorded on the X-Y plotter, the knife edge was disengaged manually from the assembly. The arch deformed a little due to the weight of the knife edge and the spring system. This was compensated in the plotter as initial load.

External load was applied to the arch gradually as the piston in the hydraulic jack sank slowly. After the arch buckled, the load was released by raising the piston back to the upper position.

c. Dynamic Test

The procedures before the disengagement of the knife edge were the same as in static tests. A motor in the Visicorder was turned on and accelerated the Linagraph paper to a constant speed of 80'' per second. 0.2 second later, the knife edge was released by the withdrawal of the retractable pin. The response of the arch and the external load were transformed into an optical signal and recorded on photo sensitive paper. The Linagraph paper was latensified by exposing to fluorescent light. The record traces became visible and readable in a few seconds.

When the motion of the arch subsided, the load was released and the experiment was repreated with a different amount of load. The critical load was determined to within 0.05 lb. or less.

B. Test Results

Four arches were used in the test program. The geometric parameters were roughly 7, 11, 14 and 18. The arches were used repeatedly until all information was acquired. Between tests, imperfection measurements showed a slight plastic deformation around the point of loading. In spite of this, repeated tests showed almost identical response characteristics.

The critical static load is shown as a nondimensional load in Table II. It appears that higher arches have higher critical loads because the nondimensional load is the product of the applied load and the geometric parameter. In fact, the flatter arches have a higher buckling load. Figure 12 shows the effect of asymmetric loading. In general, a 10 ^{o}/o reduction of critical load was detected when the load was applied offset from the center an amount equal to 6 ^{o}/o of the arch length. This effect was especially sensitive in the neighborhood of the center because the curve forms a cusp at $\epsilon = 0$. Similar behavior was obtained theoretically and experimentally by Thompson for simpler structures (Ref. 13).

Figure 13 is a comparison of the experiments with the existing analysis. The critical loads are normalized by Schreyer and Masur's classical solution (Ref. 7) and this ratio is called the critical load ratio. The upper curve is the classical solution for a sinusoidal arch (Ref. 9). The lowest curve is the static energy solution for clamped circular arches (Ref. 6). Experiments performed by Gjelsvik and Bodner have considerable scattering and the results are much lower than the present ones.

It was observed on the load deflection diagram that the equilibrium paths crossed the abscissa (displacement axis) at no point other than the origin. Therefore, only the original configuration is a possible equilibrium position at the zero load condition.

Step loading tests are summarized in Table III. Figures 14a-14d are typical deflection-time traces at the loading point when a step load was applied. The numbers attached to the curves are the load expressed in pounds. The closest pair which change in nature defines the critical load. At the critical range, a one-half per cent change of load will result in a factor of three change in response. The dotted straight lines represent the static equilibrium positions at the corresponding load levels. The subcritical responses were damped to the near equilibrium positions while the supercritical responses vibrated around the far equilibrium positions. If damping were not present, the supercritical response would have completed the bell shape curves. The superposition of the static response and the maximum dynamic response is shown in Figures 15a-15d. One observes that subcritical maximum dynamic response is always less than the second branch of the static equilibrium path. This agrees with the statement in the introduction that the energy level at such a branch is higher.

The effect of loading imperfections is shown in Figure 16. In contrast to static tests, the influence of the loading location is much less and the reduction of the critical load appears to have a smooth transition near the center.

Finally, the dynamic critical loads were normalized by Schreyer and Masur's static classical solution. The results are plotted in Figure 17. In addition, the upper bound and lower bound of the dynamic critical load for a sinusoidal arch (Ref. 9) and the numerical solution for the circular arch (Ref. 12) are superimposed on the same diagram. The present experiments agree very well with Vahidi's numerical results.

C. Conclusions

The present static experiments show higher critical loads than those obtained previously in reference 6. Among other things, the difference between the two experiments is partly due to the different way of estimating the radius of curvature. The nondimensional load is proportional to the square of the radius. A 5 °/o error in calculating the radius, therefore causes a 10 °/o error in the load. The geometric parameter γ is also proportional to the radius. Therefore, an accurate determination of the radius is important in reducing the data for comparison with the analysis. Previously, the radius was calculated by measuring the relative positions of three points on the arch. In present tests, the arch was measured at many stations. The calculated radius is a best fit to all measured points. In addition, the knowledge of the initial geometric imperfection provided a better choice of specimens and avoided unnecessary complications.

Overall, the static tests agree reasonably well with Schreyer and Masur's exact solution. The results are sensitive to the position of loading. The critical load is reduced sharply when the load is slightly off center. On the other hand, the dynamic response is quite insensitive in this respect.

For all step loading tests, the critical dynamic load was determined to within 0.05 pound. This amount of load corresponds to one-half per cent change in the total load which causes an increase of the maximum displacement by a factor of three.

The step loading tests and the analyses are summarized in Fig. 17. The upper bound obtained by Hsu or Simitses is for sinusoidal arches. They defined the static critical load as the upper bound. For the circular arches, the dotted lines are the bounds which are defined in the introduction. To obtain the bounds, the static equilibrium positions for each load level must be found. This is carried out in Appendix II. These positions correspond to the local minimums, saddle points or the local maximums on the energy surfaces.

In the case of clamped circular arches, asymmetric equilibrium positions are possible for $\gamma \geq 11.0$. Hence, for $\gamma < 11.0$, asymmetric saddle points do not exist. Consequently, the upper and lower bounds merge together. As pointed out in the introduction, this bound is more appropriately called a lower bound if damping is considered. The static critical load will be the corresponding upper critical load.

The reason why the lower bound is above the critical load obtained by Vahidi, who used numerical integration is not clear. However, the difference between the results from the two analyses is very small. In addition, the experimental results were expected to lie above the lower bound. If damping affected the experiments, the results should compare with the theory more favorably. However, the experimental results are a little below the lower bound. Static experiments show similar reduced critical load from the exact solution. This may be due to the effect of the initial geometric imperfections.

The analytical results for clamped arches have shown that the difference between an energy determination of the critical load under step loading and the results obtained by a direct integration of the differential equations is very small. The experiments show good agreement with both analytical results. Therefore, the success of the energy method has been demonstrated for this structure. It seems significant to extend this type of work to more complicated structures where a direct solution of the differential equations is impractical.

Finally, it was found that the original rest configuration of the arch was the only equilibrium position at the zero load condition. This is in agreement with Vahidi's calculation (Ref. 14). Since the existence of other equilibrium positions is a requirement in an energy approach to determine the critical load level, the impulsive loaded clamped circular arch can not be rigorously classified as a buckling problem.

III. STABILITY OF CLAMPED SHALLOW CIRCULAR ARCHES UNDER UNIFORMLY DISTRIBUTED IMPULSIVE LOAD

For the impulsive loading experiments 11 arches were used. They were divided into two groups. One group had a geometric parameter close to 10, the other group close to 20. Silver acetylide-silver nitrate was sprayed directly on the arch. This light sensitive explosive was detonated by a Xenon flash tube. The response of the arch was recorded by a high speed camera. The displacement was measured carefully and the data analyzed on a digital computer. The explosive load was a very short duration pressure loading. If the duration is much shorter than the fundamental natural period, the loading can be treated as giving the arch an initial velocity. For all positive time, the arch is free from lateral load and is in free vibration. Obviously, this is a particular case of Part II, where the energy surface at zero load condition should be investigated. Although there exists only one equilibrium position, it is suspected that there may be a significant change of maximum response in a relatively narrow range of impulse parameter. If this is the case, the determination of the inflection point on the maximum response curve is therefore significant.

A. Experiment

These experiments consisted of loading a clamped circular arch with a very short duration uniform pressure load. The arches were fabricated, chosen and mounted the same way as in Part II. The resulting motion of the arch was recorded using high speed photography.

A detailed description of the experimental work is presented in the following sections. The results are compared with Humphreys experiments and analysis (Refs. 15 and 16).

1. Impulsive Load

Silver Acetylide-Silver Nitrate was used to apply a very short duration pressure loading on the arch. The advantage of this chemical is the low level of impulse, which is approximately one-tenth of other commercially available explosives, and its ability to be detonated with an intense light. The general properties are discussed in references 17 and 18. Here a brief description of the preparation and calibration of this explosive will be given.

To begin with, each 10 grams of silver nitrate salt are dissolved into 40 cc. of distilled water. Then 6 cc. of concentrated nitric acid (s.g. 1.4) is slowly added. The solution is gently stirred until all crystals are dissolved and then acetylene gas is bubbled through the solution. Fine grained white precipitate is obtained by letting the gas come through very slowly. This is more desirable for spraying. After the white powder ceases to precipitate, it is washed with acetone. With acetone as a thinner the precipitate is sprayed on the arch surface. It is then dried in an oven at about 100 degrees Fahrenheit. Aging for more than one day is not recommended.

The weight of explosive needed for each arch must be accurately calculated before spraying. The amount that is going to be applied to the arch must be sprayed very carefully so that it differs not more than several hundredths of a gram to that estimated. Over spraying cannot be remedied and the whole process has to be repeated from the very beginning.

This explosive can be detonated by an electric spark or an intense light. It has been shown that a fairly large area can be detonated within a few microseconds if expendable Xenon flash tubes are used (Ref. 18). It was found that if one nonexpendable Xenon flash tube was used, complete detonation over the longest arch could be accomplished in less than 150 microseconds. This duration of loading on the whole arch is short enough that it can be considered impulsive (Ref. 15).

A GE-522 Xenon flash tube, mounted in a parabolic reflector, was used as the detonator. The tube was driven by a 250 microfarad capacitor charged to 5,000 volts. The rise time of the tube was about 20 microseconds and the duration of the light pulse was of the order of 300 microseconds.

The calibration of the impulse generated by this explosive was carried out on a ballistic pendulum. The explosive was deposited evenly on a 2 inch square steel plate and attached to the end of the pivoted arm of the pendulum. The calibration curve of impulse vs. weight is shown in Fig. 18. The offset from the origin is due to the friction at the pivot point. From these data an impulse level of $0.152 \frac{\text{lb-sec/in}^2}{\text{gm/in}^2}$ $(6.75 \times 10^4 \frac{\text{dyne-sec/cm}^2}{\text{gm/cm}^2})$ was calculated. This is about 3.6 per cent lower than previously found in Ref. 17.

2. Camera Setup

A 16 mm, high speed motion picture camera (HyCam, Red Lake Laboratories) was used to record the response of the arch. The axis of the camera was aligned perpendicular to the base line of the arch. To eliminate as much distortion as possible, the camera was placed at least 7 feet away. Two different lenses were used to cover the size of field necessary for the different length arches tested. These lenses were a f/1.9 Cosmicar Television Lens with a focal length of 75 mm and a f/1.8 Super Talcumar from Asahi Optical Company with a focal length of 55 mm.

The light was provided by four 1,000 watt quartz-iodine flood lamps. They were placed on the side of the arch opposite the camera and aimed directly at the camera. In order to collect more light at the camera, a large plastic Fresnel lens of focal length of 30 inches was placed between the arch and the lamps. A sheet of clear Mylar was placed on the flat side of the Fresnel lens to help diffuse the intense and unevenly concentrated light. A spot light meter at the camera position was used to check the evenness of the lighting of the Fresnel lens. The camera setup is shown in Figure 19.

A 400 foot roll of Kodak Tri-X negative (ASA rating of 400) of standard thickness (0.006 inches) was used for each test shot. However, the desired framing rate of 10,000 pictures per second was only obtained on the last 100 feet of film. The exact framing rate was determined by a timing light which exposed a small dot of light on the edge of the film every 1/1000 of a second.

3. Response Measurement

A detailed deflection history of the arch motion was obtained by reading the film frame by frame. The film was projected using a 500 watt slide projector on a mirror at a distance of about 15 feet. The image was reflected to a screen ruled with 21 equally spaced lines (Fig. 20). The distance to the mirror was adjusted until the arch image from support to support fix exactly on the twenty equal division on the screen. The lines then serve as the X coordinate for the arch. The Y distance was measured using a stretched wire perpendicular to the X lines. This wire was attached to a moving slide whose position was measured by a linear potentiometer. The wire was carefully moved to each intersection of the arch image and the lines ruled on the screen. The potentiometer reading was automatically recorded on punched cards for digital computer reduction. Approximately 50 frames were read for each test covering about 10 milliseconds of motion.

4. Test Procedure

When a particular value of γ was selected the arch was cut to the appropriate length and a 3/16 inch hole was drilled in each end. This hole provided a more secure support of the arch in the frame. The surface of the arch was then cleaned and the weight determined to the nearest 1/2000 of a gram. An estimation of the weight of the explosive was made and then it was sprayed on the convex side of the arch. The explosive was cured for one hour at 100 degrees Fahrenheit. The arch and the explosive are then weighed and the amount of deposited explosive determined. If the correct amount is not obtained the process was repeated until the weight differs from that desired by a few hundredths of a gram. Next the arch was secured in the steel frame with Devcon B.

After the Devcon has hardened, the arch and support are aligned with the camera. The Xenon flash tube was placed about 10 inches above the surface of the arch and the evenness of the light source was checked. The camera was started and an Event Synchronizer built into the camera discharged the Xenon tube when 325 feet of film had been exposed. This point is shown as point A in the camera performance curve (Fig. 21). The deformation of the arch that is of interest takes about 3 feet of film. The last 100 feet of exposed film was developed and the part of interest retained.

B. Test Results

A total of 11 tests were recorded by the high speed camera. These tests were divided into two groups. Group B has a geometric parameter γ close to 10 and for group C, γ was close to 20. The dimensions are listed in Table IV. The arches used for testing were selected so as to minimize the size of initial imperfections. The initial imperfections are shown in Figure 22. In all cases the deviation from the perfect arch was less than 5 per cent of the thickness.

The response of the arches to impulsive loading was examined in several manners. First the average displacement was calculated for the time of response of interest. This displacement is defined as the area between the deformed and undeformed arch. It is normalized to the area enclosed by the undeformed arch and the base line. The values of the maximum average displacement are listed in Table V and are shown in Figure 23 as a function of the nondimensional impulse $\bar{I}$. This figure shows that the arch exhibits a large increase in maximum response over a rather small range of impulse level. The maximum rate of change of response (the inflection points for the faired curves in Figure 23) are at an impulse level $\bar{I}$ of 9 and 22 for γ equal to 10 and 20 respectively. It is interesting to note that these points are close to the point of average displacement equal to one which was used by Humphreys (Ref. 15) to define the critical load. However, they are about 6-7 times as high as Humphreys' experimental results. The reason for this is not known at this time. A comparison with Humphreys' results is shown in Figure 24.

The deformation of the arch can also be displayed as successive pictures of the arch shape. This is done for two representative shots in Figure 25. Time starts at the top of the figure and the time between successive shapes is about 200 microseconds.

In order to get a more quantitative picture of the arch deformation, a three mode approximation to the deformed shape was calculated. The representation used is as follows:

$$w = (1 - \frac{\alpha^2}{\beta^2})^2 \left[q_1(t) + \frac{\alpha}{\beta} \; q_2(t) + \frac{\alpha^2}{\beta^2} \; q_3(t) \right] h$$

The coefficients were determined by using a "Least Square Fit" of the experimental data from the high speed pictures. The time history of the two symmetric modes is shown in Figure 26 for the arches tested. The trajectories in a q_1, q_3 space can also be displayed. Figure 27 shows a supercritical and subcritical response for each group of arches. The line of average displacement equal to one is also shown in the figures.

In addition to the dynamic tests results described above, an attempt was made to determine the static equilibrium positions of the clamped arch. This is of interest since the existence of these positions is a requirement in an energy approach to determining the dynamic buckling loads. These tests were carried out by pushing the arch through to a large displacement configuration by hand and attempting to find a position where it would stay. This was unsuccessful for the 4 arches used with $\gamma \approx 10$ and 20. In addition, the existence of an unstable equilibrium position could not be detected. This is somewhat more difficult to determine experimentally since it is like trying to balance a ball on top of a hill. However, there did not seem to be any equilibrium points other than the undeformed position for the arches tested. This is in agreement with Vahidi's calculation (Ref. 14).

C. Conclusion

The experimental work on the impulsively loaded clamped circular arch shows that the maximum response has a significant increase in value for a small increase in load at some value of impulse. It would appear from the data available that this increase is a smooth transition from a small response to a large response at some critical impulse level. Therefore, the use of a definition of dynamic buckling which requires a finite change in response for an infinitesimal increase in load would not consider this problem as a dynamic buckling problem. However, from a practical point of view the increase in deflection is of the order of three for a small increase in impulse level. This increase is about the same amount as one obtains for step loading on a simply supported arch in the range of geometric parameter where direct snapping occurs (Ref. 11).

It is of interest to note that this problem is like the one of direct snapping as categorized by Lock (Ref. 11). In other words the structure reaches its maximum displacement on the first oscillation of the fundamental mode. This can be seen from the response plots (Fig. 26) combined with the trajectories (Fig. 27). An examination of the nonsymmetric response was also made. The first component of the antisymmetric response is shown in Figure 28. As seen from these two cases of a subcritical and supercritical impulse, the antisymmetric mode was not parametrically excited by the fundamental mode. It obtained its maximum or nearly maximum early in the motion, and did not grow until the symmetric response achieved its maximum displacement.

In summary, while no evidence has been found that the clamped circular arch under impulse loading can be rigorously categorized as a dynamic buckling problem, it is clear that over a small range in impulse the arch undergoes a significant increase in response. It is therefore of practical significance to determine this range of impulse. In addition, it was experimentally determined that no stable equilibrium position exists for the clamped arch free from lateral load other than the undeformed position. Also, the existence of an unstable equilibrium position was not detected.

REFERENCES

1. Fung, Y. C. and Sechler, E. E.: "Instability of Thin Elastic Shells", Structural Mechanics, Proc. of First Symposium on Naval Structural Mechanics, Pergamon Press, New York, pp 115-168, (1960).
2. Tsien, H. S.: "A Theory for the Buckling of Thin Shells", J. Aero. Sci., Vol. 9, No. 10, pp 373-384, (Aug. 1942).
3. Babcock, C. D., Jr.: "The Influence of the Testing Machine on the Buckling of Cylindrical Shells under Axial Compression", Int. J. Solid Structures, 3, pp 809-817, (1967).
4. Arbocz, J. and Babcock, C. D., Jr.: "The Effect of General Imperfections on the Buckling of Cylindrical Shells", to be published, Journal of Applied Mechanics.
5. Fung, Y. C. and Kaplan, A.: "Buckling of Low Arches on Curved Beams of Small Curvature", NACA TN 2840, (Nov. 1952).
6. Gjelsvik, A. and Bodner, S. R.: "The Energy Criterion and Snap Buckling of Arches", J. Eng. Mech. Div., AMCE, pp 87-134 (October 1962).
7. Schreyer, H. L. and Masur, E. F.: "Buckling of Shallow Arches", J. Eng. Mech. Div., Proc. ASCE, pp 1-17 (August 1966).
8. Hoff, N. J. and Bruce, V. G.: "Dynamic Analysis of the Buckling of Laterally Loaded Flat Arches", J. Math Phys., 32, pp 276-288 (1954).
9. Hsu, C. S.: "Equilibrium Configurations of a Shallow Arch of Arbitrary Shape and Their Dynamic Stability Character", Int. J. Non-Linear Mechanics, 3, pp 113-136 (1968).

10. Simitses, G. J.: "Dynamic Snap-Through Buckling of Low Arches and Shallow Spherical Caps", Ph.D. Dissertation, Dept. of Aero. and Astro., Stanford University (June 1965).

11. Lock, M. H.: "The Snapping of a Shallow Sinusoidal Arch under a Step Pressure Load", Aerospace Corp., Space Systems Div., TR-65-107 (July 1965).

12. Vahidi, B.: "Dynamic Stability of Clamped Circular Arches", Graduate Student, University of California, San Diego, Private Communication.

13. Thompson, J. M. T.: "Dynamic Buckling under Step Loading", Dynamic Stability of Structures, Edited by G. Herrmann, Pergamon Press, pp 215-236 (1967).

14. Vahidi, B.: "Non-Existence of Snap-Through for Clamped Shallow Elastic Arches Subjected to Impulsive Load", TR No. 8, University of California, San Diego, (March 1968).

15. Humphreys, J. S.: "On Dynamic Snap-Buckling of Shallow Arches", AIAA Journal, Vol. 4, No. 5, pp 878-886, (May 1966).

16. Humphreys, J. S.: "On the Adequacy of Energy Criteria for Dynamic Buckling of Arches", AIAA Journal, Vol. 4, No. 5, pp 921-928, (May 1966).

17. Nevill, G. E. and Hoese, F. O.: "Impulsive Loading Using Sprayed Silver Acetylide-Silver Nitrate", Experimental Mechanics, pp 294-298, (Sept. 1965).

18. Hoese, F. O.; Langner, C. G. and Baker, W. E.: "Simultaneous Initiation over Large Areas of a Spray Deposited Explosive", Experimental Mechanics, pp 392-397, (Sept. 1968).

APPENDIX I

LEAST SQUARE FIT OF THE IMPERFECT CIRCULAR ARCH

The concave side of the arch surface was marked every half an inch. At these positions, the distance with respect to a fixed point was measured by a rotatable arm as described previously (see Fig. 29). These distances were denoted by R_i. The "Best Fit Radius" $\bar{R}$, and "Best Fit Center" (BFC) were found by the method of least square error. The distance between the two centers is r, and the angle between a vertical line and the line joining two centers is θ. Furthermore, express R_i with respect to BFC and call that distance $\bar{R}_i$. The relation between $\bar{R}_i$ and R_i, r is as follows:

$$\bar{R}_i = \left[(R_i \sin\alpha_i + r.\sin\theta)^2 + (R_i.\cos\alpha_i + r.\cos\theta)^2\right]^{1/2} \qquad (1)$$

Then, the deviation of the arch surface from the "Best Fit Arch" is e_i where

$$e_i = \bar{R} - \bar{R}_i \qquad (2)$$

Assuming that there were N positions along the arch, the total square error ϵ is given by

$$\epsilon = \sum_{i=1}^{N} e_i^2 \qquad (3)$$

The undetermined parameters $\bar{R}$, r and θ can be determined by the following variational equations.

$$\frac{\partial\epsilon}{\partial R} = N(\bar{R} - K_1 - rK_2 \cos\theta) = 0 \qquad (4)$$

$$\frac{\partial \epsilon}{\partial \theta} = K_3 \cos\theta + (K_1K_2 - K_4)\sin\theta + \frac{r}{2}\left[K_1K_5 \cos 2\theta + (K_2^2 - K_1K_6)\sin 2\theta\right] = 0 \tag{5}$$

$$\frac{\partial \epsilon}{\partial r} = (K_1K_2 - K_4)\cos\theta - K_3 \sin\theta + \frac{r}{2}\left[(K_2^2 - K_1K_6)\cos 2\theta - K_1K_5 \sin 2\theta + (K_2^2 + K_1K_7 - 2)\right] = 0 \tag{6}$$

where

$$K_1 = \frac{1}{N}\sum_{i=1}^{N} R_i \qquad K_5 = \frac{1}{N}\sum_{i=1}^{N} \frac{1}{R_i}\sin 2\alpha_i$$

$$K_2 = \frac{1}{N}\sum_{i=1}^{N} \cos\alpha_i \qquad K_6 = \frac{1}{N}\sum_{i=1}^{N} \frac{1}{R_i}\cos 2\alpha_i$$

$$K_3 = \frac{1}{N}\sum_{i=1}^{N} R_i \sin\alpha_i \qquad K_7 = \frac{1}{N}\sum_{i=1}^{N} \frac{1}{R_i}$$

$$K_4 = \frac{1}{N}\sum_{i=1}^{N} R_i \cos\alpha_i$$

and $\sum_{i=1}^{N} \sin\alpha_i = 0$. The relation (4) has been used in (5) and (6). Combining (5) and (6) and eliminating r, a transcendental equation for θ is obtained

$$\tan\theta = -\frac{B}{A} \tag{7}$$

where

$$A = K_1K_2 - K_4 + \frac{K_1}{2}(K_4K_7 - K_1K_2K_7 + K_4K_6 - 3K_1K_2K_6 + K_3K_5)$$

$$B = K_3(1 - K_2^2) + \frac{K_1}{2}(K_3K_6 - K_3K_7 - K_4K_5 + K_1K_2K_5)$$

APPENDIX II

EQUILIBRIUM POSITIONS AND THEIR ENERGY LEVELS OF CLAMPED ARCHES UNDER CONCENTRATED LOAD

NOMENCLATURE

A	Cross sectional area of the arch
A_1, A_2, A_3, A_4	Integration constant
B_1, B_2, B_3, B_4	Integration constant
E	Young's Modulus
h	Arch thickness
H	Central arch rise
I	Moment of inertia
L	Arch length
N	Axial thrust
P	Concentrated load
$\tilde{P} = \frac{PL^3}{16EI}\sqrt{\frac{A}{I}}$	Nondimensional load
R	Arch radius
$S(t)$	Heaviside step function
t	Time
w	Arch displacement
$w_0 = H(1-\frac{4x^2}{L^2})$	Initial arch shape
x	Arch coordinate
$\bar{x} = \frac{2x}{L}$	Nondimensional arch coordinate

$y = \frac{w}{2}\sqrt{\frac{A}{I}}$	Nondimensional arch displacement
$y_0 = \frac{w_0}{2}\sqrt{\frac{A}{I}}$	Nondimensional initial arch shape
β	Arch half angle
$\gamma = \frac{L^2}{4Rh} = \frac{\beta^2 R}{h} = \frac{2H}{h}$	Geometric Parameter
$\delta(x)$	Dirac delta function
μ	Nondimensional axial strain
Π	Potential energy of the system
$\overline{\Pi} = \Pi \cdot \frac{L^3 A}{16EI^2}$	Nondimensional potential energy
ρ	Mass density
$\tau = \frac{4}{L^2}\sqrt{\frac{EI}{\rho A}}\, t$	Nondimensional time
$(\ )' = \frac{\partial}{\partial x}$	
$(\dot{\ }) = \frac{\partial}{\partial \tau}$	

A. Symmetric Equilibrium Positions

The coordinate system is shown in Figure 30. The equations of motion of a shallow arch can be expressed in terms of the displacement as derived in reference 8.

$$EI\left(\frac{\partial^4 w}{\partial x^4} - \frac{\partial^4 w_o}{\partial x^4}\right) + N\frac{\partial^2 w}{\partial x^2} + \rho A\frac{\partial^2 w}{\partial t^2} + P\delta(x)S(t) = 0 \tag{1}$$

where

$$N = \frac{AE}{2L}\int_{-L/2}^{L/2}\left[\left(\frac{\partial w_o}{\partial x}\right)^2 - \left(\frac{\partial w}{\partial x}\right)^2\right] \cdot dx$$

Substituting the nondimensional quantities, (1) can be written in dimensionless form as follows,

$$y'''' + \mu^2 y'' + y + \widetilde{P}\delta(x)\, S(\tau) = 0 \tag{2}$$

where

$$\mu^2 = \int_{-1}^{1}\left[(y_o')^2 - (y')^2\right] d\bar{x} \tag{3}$$

The static equilibrium positions can be obtained by letting the inertia term equal to zero. The corresponding static equation will be

$$y'''' + \mu^2 y'' + \widetilde{P}\delta(\bar{x}) = 0 \tag{4}$$

The homogeneous solutions of (4) are:

$$
\begin{aligned}
y_1 &= A_1 \sin \mu \bar{x} + A_2 \cos \mu \bar{x} + A_3 \bar{x} + A_4 \qquad [-1 \leq \bar{x} < 0] \\
y_2 &= B_1 \sin \mu \bar{x} + B_2 \cos \mu \bar{x} + B_3 \bar{x} + B_4 \qquad [0 < \bar{x} \leq 1]
\end{aligned} \tag{5}
$$

The boundary conditions for the clamped arches are:

$$
\begin{aligned}
y_1(-1, \tau) &= 0 \\
y_1'(-1, \tau) &= y_0'(-1, \tau) = \sqrt{3}\,\gamma \\
y_2(1, \tau) &= 0 \\
y_2'(1, \tau) &= y_0'(1, \tau) = -\sqrt{3}\,\gamma
\end{aligned} \tag{6}
$$

The continuity conditions and the jump in shear at the point of loading ($\bar{x} = 0$) are expressed as follows:

$$
\begin{aligned}
y_1(0, \tau) - y_2(0, \tau) &= 0 \\
y_1'(0, \tau) - y_2'(0, \tau) &= 0 \\
y_1''(0, \tau) - y_2''(0, \tau) &= 0 \\
y_1'''(0, \tau) - y_2'''(0, \tau) &= \widetilde{P}
\end{aligned} \tag{7}
$$

Substitute (5) into (6) and (7), and provided that $\tan \mu \neq \mu$, the unknown constants are found as follows:

$$A_1 = -\frac{\widetilde{P}}{2\mu^3}$$

$$A_2 = \frac{1}{2\mu \sin\mu} \left[2\sqrt{3}\,\gamma + \frac{\widetilde{P}}{\mu^2} (\cos \mu - 1) \right]$$

$$\begin{aligned}
A_3 &= \frac{\widetilde{P}}{2\mu^2} \\
A_4 &= \frac{\widetilde{P}}{2\mu^2}\left(1 - \frac{\sin\mu}{\mu}\right) - A_2 \cos\mu \\
B_1 &= \frac{\widetilde{P}}{2\mu^3} \\
B_2 &= A_2 \\
B_3 &= -\frac{\widetilde{P}}{2\mu^2} \\
B_4 &= A_4
\end{aligned} \tag{8}$$

The constants $A_1, A_2, \ldots, B_4$ are functions of μ and $\widetilde{P}$. The $\mu \sim \widetilde{P}$ relationship can be found by substituting (5) into (3).

$$\begin{aligned}
\mu^2 = {} & 2\gamma^2 + (A_2^2 - A_1^2 + B_2^2 - B_1^2)\frac{\mu}{4}\sin 2\mu \\
& - (A_1A_2 - B_1B_2)\mu\sin^2\mu - 2(A_1A_3 + B_1B_3)\sin\mu \\
& + 2(A_2A_3 - B_2B_3)(\cos\mu - 1) - (A_1^2 + A_2^2 + B_1^2 + B_2^2)\frac{\mu^2}{2} - (A_3^2 + B_3^2)
\end{aligned} \tag{9}$$

The roots of this transcendental equation correspond to the value of μ at the equilibrium positions under the specified load level $\widetilde{P}$.

B. Antisymmetric Equilibrium Positions

In evaluating (6, 7), the following algebraic equation must be solved

$$\begin{bmatrix} -\sin\mu & -1 \\ \mu\cos\mu & 1 \end{bmatrix} \begin{Bmatrix} A_1 \\ A_3 \end{Bmatrix} = \begin{Bmatrix} \frac{P}{2\mu^2}\left(\frac{\sin\mu}{\mu} - 1\right) \\ \frac{P}{2\mu^2}(1 - \cos\mu) \end{Bmatrix} \tag{10}$$

If the determinant of the coefficient of A vanishes, i.e., $\tan\mu = \mu$, A_1, A_3 can not be determined uniquely as in (8). The lowest possible μ that satisfies this condition is $\mu = 4.492$. In this case, only one of (10) is independent.

$$A_3 = \frac{P}{2\mu^3}(\mu - \sin\mu) - A_1 \sin\mu \tag{11}$$

Substitute (11) and (5) into (3). A quadratic equation of A_1 is obtained.

$$\begin{aligned} &(\sin^2\mu - \mu^2)A_1^2 + \frac{P}{\mu^3}(\sin^2\mu - \mu^2)A_1 \\ &+ \Big[\mu(\sin\mu\cos\mu - \mu)A_2^2 + \frac{P}{\mu^2}(\sin^2\mu + 2\cos\mu - 2)A_2 \\ &+ \frac{P^2}{\mu^5}(\sin\mu - \mu) + 2\gamma^2 - \mu^2\Big] = 0 \end{aligned} \tag{12}$$

The A_2, A_4, B_1, B_2, B_3 and B_4 will be determined according to (8).

C. Potential Energy of the System

Let Π designate the potential energy

$$\Pi = \int_{-L/2}^{L/2} \frac{EI}{2}\left[\frac{\partial^2(w-w_o)}{\partial x^2}\right]^2 dx + \frac{1}{2}EAL\left(\frac{N}{AE}\right)^2 - P(w_o - w)\Big|_o \tag{13}$$

The nondimensional potential energy $\overline{\Pi}$ is as follows:

$$\overline{\Pi} = \int_{-1}^{1} (y'' - y_o'')^2 \, dx + \frac{1}{2} \mu^4 - 2\widetilde{P} \, (y_o - y) \Big|_o \tag{14}$$

Substitute (5) into (14), we get

$$\begin{aligned} \overline{\Pi} = \mu^3 \Big[& \frac{\mu}{2}(A_1^2 + A_2^2 + B_1^2 + B_2^2) - \frac{1}{4}(A_1^2 - A_2^2 + B_1^2 - B_2^2) \sin 2\mu \\ & - (A_1A_2 - B_1B_2) \sin^2 \mu \Big] + 2\sqrt{3}\gamma \mu \Big[(A_1 - B_1)(1 - \cos \mu) \\ & - (A_2 + B_2) \sin \mu \Big] + 6\gamma^2 + \frac{1}{2} \mu^4 - 2 \, \widetilde{P}\Big(\frac{\sqrt{3}}{2} \gamma - A_2 - A_4\Big) \end{aligned} \tag{15}$$

The results obtained above were evaluated numerically on an IBM 360/75 computer. The numerical results for the critical static load agree with the results obtained by Schreyer and Masur (Ref. 7). The values of the upper and lower bounds were numerically calculated and are shown in Figure 17.

TABLE I

Geometric Descriptions of the Tested Arches

	Arch 32	Arch 29	Arch 28	Arch 25
b (in)	0.75	0.75	0.75	0.75
h (in)	0.0632	0.0643	0.0643	0.0643
L (in)	12.20	10.90	9.50	7.75
R (in)	31.56	32.09	32.01	31.58
*γ	18.655	14.395	10.962	7.395
*H (in)	0.5895	0.4628	0.3524	0.2377
*β (degree)	11.075	9.729	8.503	7.030

* Calculated

TABLE II

Nondimensional Static Critical Load $\bar{P}$

ϵ	Arch 32	Arch 29	Arch 28	Arch 25
0.00	218.7	165.3	124.6	79.2
0.005		154.6	115.5	74.1
0.01	212.0	153.4	113.2	72.1
0.02	209.0	151.0	112.1	72.2
0.03	206.4	148.9	107.5	71.2
0.04	201.8	146.5	108.8	70.9
0.05	200.3	144.8	106.6	69.8
0.06	196.2	144.2	106.6	70.4

TABLE III

Critical Step Load

Arch 32. γ = 18.655

ϵ	P (lb)	$\overline{P}$	Result
0.00	10.60	197.1	
	10.65	198.1	
	10.70	199.0	buckled
0.01	10.40	193.4	
	10.60	197.1	
	10.65	198.1	
	10.70	199.0	buckled
	10.80	200.9	buckled
0.02	10.45	194.3	
	10.50	195.2	buckled
	10.60	197.1	buckled
0.03	10.30	191.5	
	10.35	192.5	buckled
	10.40	193.4	buckled
	10.50	195.2	buckled

TABLE III (Cont'd)

Critical Step Load

Arch 32. $\gamma = 18.655$

ϵ	P (lb)	$\overline{P}$	Result
0.04	10.20	189.7	
	10.25	190.6	buckled
	10.30	191.5	buckled
0.05	10.20	189.7	
	10.25	190.6	
	10.25	190.6	buckled
0.06	10.10	187.9	
	10.15	188.8	buckled
	10.20	189.7	buckled

TABLE III (Cont'd)

Critical Step Load

Arch 29. γ = 14.395

ϵ	P (lb)	$\overline{P}$	Result
0.00	11.65	144.2	
	11.70	144.8	
	11.75	145.4	
	11.80	146.1	buckled
0.005	11.50	142.3	
	11.70	144.8	
	11.75	145.4	
	11.80	146.1	buckled
0.01	11.60	143.6	
	11.65	144.2	
	11.70	144.8	buckled
0.02	11.50	142.3	
	11.55	143.0	buckled
0.03	10.95	135.6	
	11.00	136.2	buckled
	11.10	137.4	buckled
	11.20	138.7	buckled
	11.25	139.3	buckled

TABLE III (Cont'd)

Critical Step Load

Arch 29. γ = 14.395

ϵ	P (lb)	$\overline{P}$	Result
0.03	11.30	139.9	buckled
	11.40	141.2	buckled
	11.50	142.3	buckled
0.04	10.50	129.9	
	10.60	131.2	
	10.70	132.4	
	10.75	133.1	
	10.80	133.7	buckled
0.05	10.50	129.9	
	10.60	131.2	
	10.70	132.4	
	10.75	133.1	buckled
0.06	10.45	129.4	
	10.50	129.9	
	10.55	130.6	
	10.60	131.2	buckled

TABLE III (Cont'd)

Critical Step Load

Arch 28. $\gamma = 10.962$

ϵ	P (lb)	$\overline{P}$	Result
0.00	12.00	98.3	
	13.00	106.5	buckled
	13.05	107.0	buckled
	13.10	107.4	buckled
	13.20	108.1	buckled
	13.50	110.6	buckled
0.005	13.00	106.5	
	13.05	107.0	buckled
0.01	12.60	103.2	
	12.70	104.1	
	12.80	104.9	
	12.90	105.7	
	12.95	106.1	
	13.00	106.5	buckled
0.02	12.60	103.2	
	12.70	104.1	
	12.75	104.5	
	12.80	104.9	
	12.85	105.3	
	12.90	105.7	buckled

TABLE III (Cont'd)

Critical Step Load

Arch 28. γ = 10.962

ϵ	P (lb)	$\overline{P}$	Result
0.03	12.70	104.1	
	12.75	104.5	buckled
0.04	12.50	102.5	
	12.55	102.9	buckled
0.05	12.30	100.8	
	12.35	101.2	
	12.40	101.6	buckled
0.06	12.10	99.2	
	12.20	100.0	
	12.25	100.4	
	12.30	100.8	
	12.35	101.2	
	12.40	101.6	buckled

TABLE III (Cont'd)

Critical Step Load

Arch 25. γ = 7.395

ϵ	P (lb)	$\overline{P}$	Result
0.00	13.50	60.1	
	13.60	60.5	
	13.70	61.0	
	13.80	61.4	
	13.90	61.9	
	14.00	62.3	
	14.05	62.5	
	14.10	62.7	
	14.15	63.0	
	14.20	63.2	buckled
	14.50	64.5	buckled
	15.00	66.7	buckled
0.005	14.15	63.0	
	14.20	63.2	buckled
0.01	14.15	63.0	
	14.20	63.2	buckled
0.02	14.10	62.7	
	14.15	63.0	buckled

TABLE III (Cont'd)

Critical Step Load

Arch 25. γ = 7.395

ϵ	P (lb)	$\overline{P}$	Result
0.03	13.95	62.1	
	14.00	62.3	
	14.05	62.5	buckled
0.04	13.90	61.9	
	13.95	62.1	
	14.00	62.3	buckled
0.05	14.00	62.3	
	14.05	62.5	buckled
0.06	14.05	62.5	
	14.10	62.7	buckled

TABLE IV

Geometric Description of Tested Arches

Arch	Thickness (in)	Radius (in)	Length (in)	γ
B9	0.0623	31.76	8.64	9.43
B6	0.0623	30.22	8.43	9.44
B7	0.0622	25.45	8.13	10.44
B8	0.0623	32.33	8.57	9.12
C3	0.0605	31.31	12.08	19.25
C2	0.0605	31.57	12.20	19.48
C5	0.0605	30.55	12.28	20.40
C4	0.0605	28.10	12.12	21.60
C8	0.0604	29.47	12.03	20.33
C7	0.0604	26.64	12.11	22.79
C9	0.0603	31.84	12.31	19.73

TABLE V

Summary of Impulse Tests

Arch	W_e/A (gm/in^2)	$\overline{I}$	W^a_{max}
B9	0.0626	8.43	0.5596
B6	0.0749	10.45	1.3905
B7	0.0964	12.19	1.5830
B8	0.0847	14.82	1.7342
C3	0.0742	12.60	0.2281
C2	0.0799	15.08	0.3616
C5	0.0826	16.66	0.3969
C4	0.0854	16.95	0.4669
C8	0.0962	20.33	0.6239
C7	0.1098	21.65	0.9185
C9	0.1037	27.75	1.6227

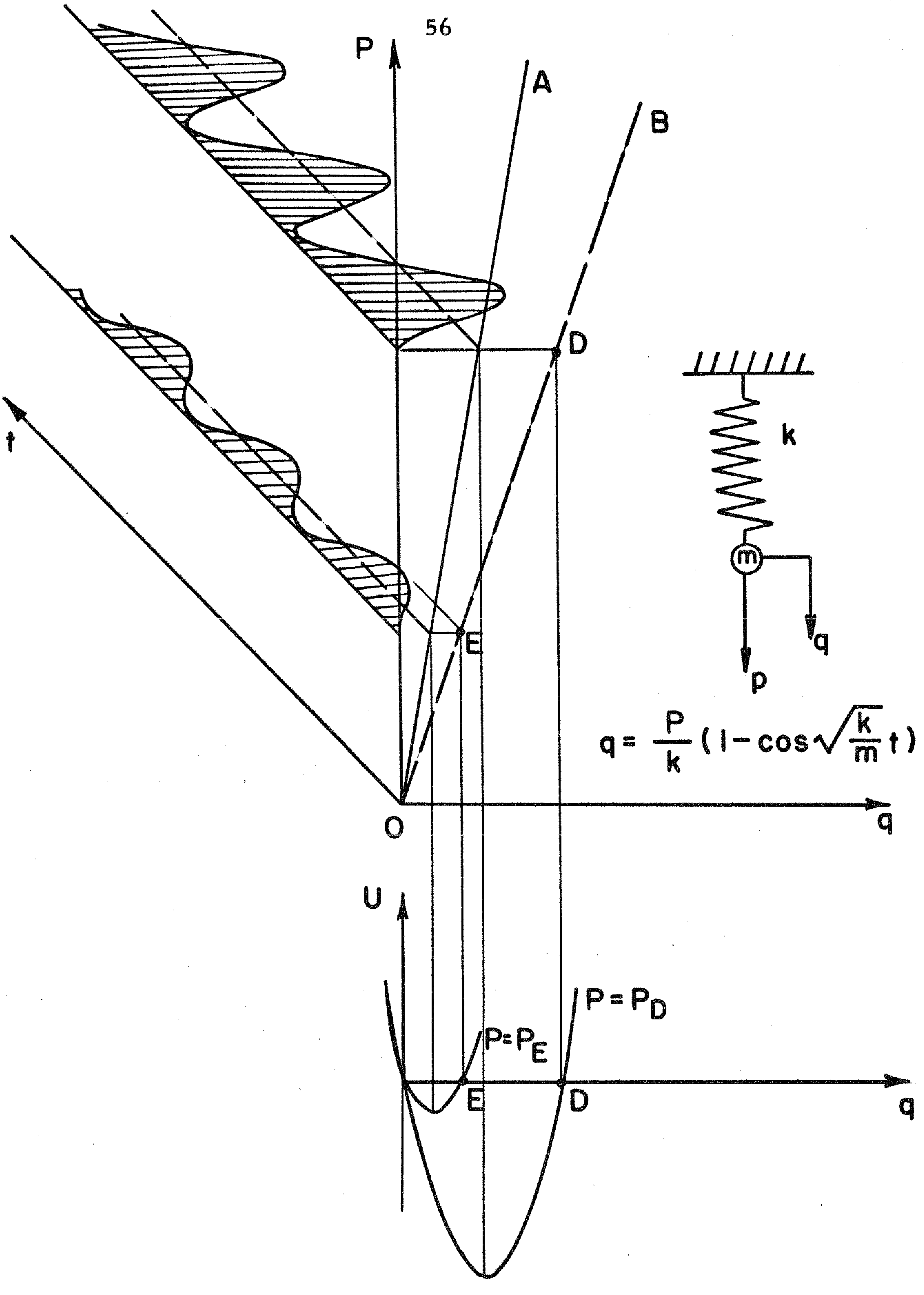

FIG. 1 RESPONSE OF LINEAR SPRING MASS SYSTEM

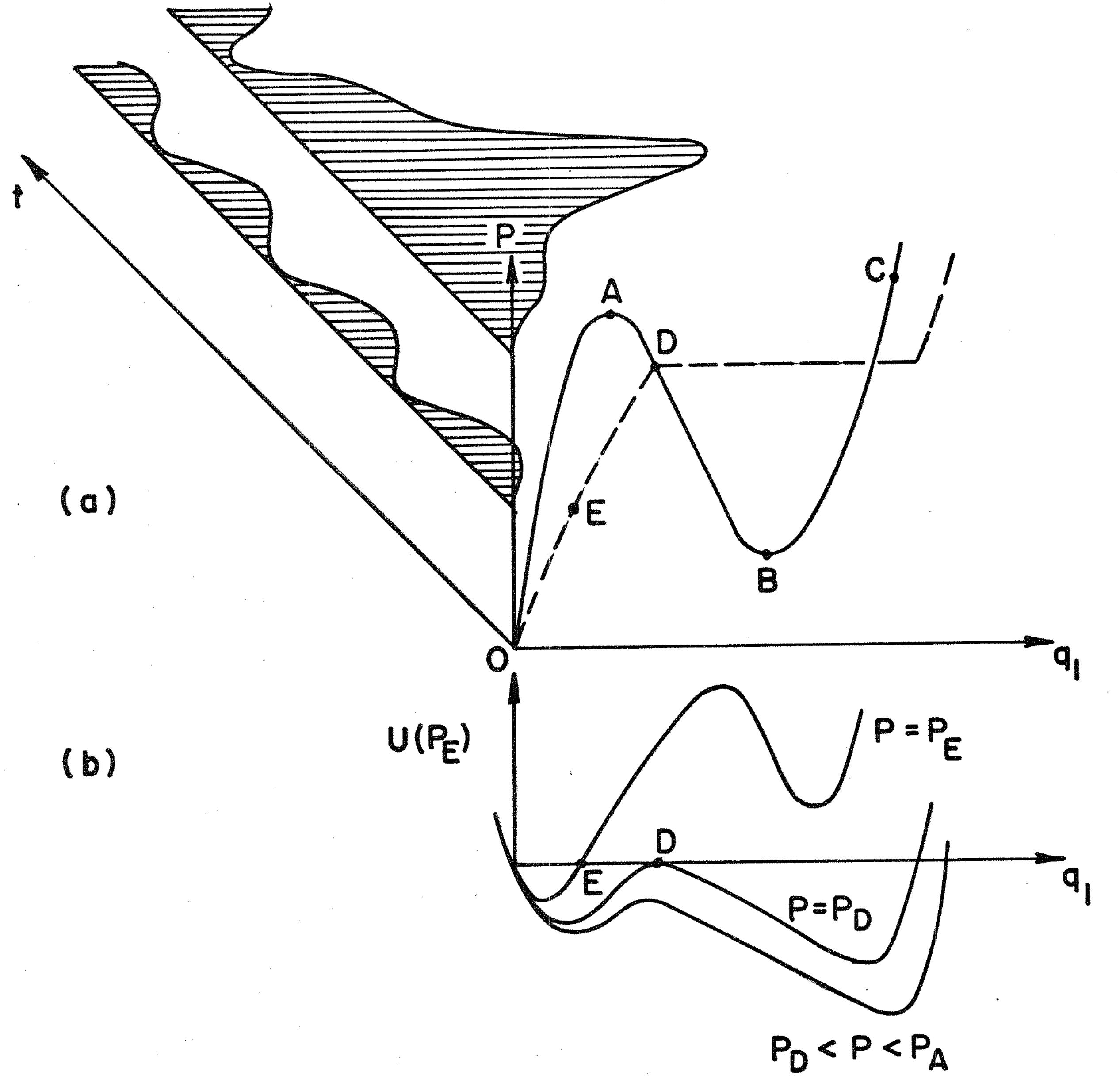

FIG. 2 NONLINEAR RESPONSE OF ONE DEGREE OF FREEDOM SYSTEM

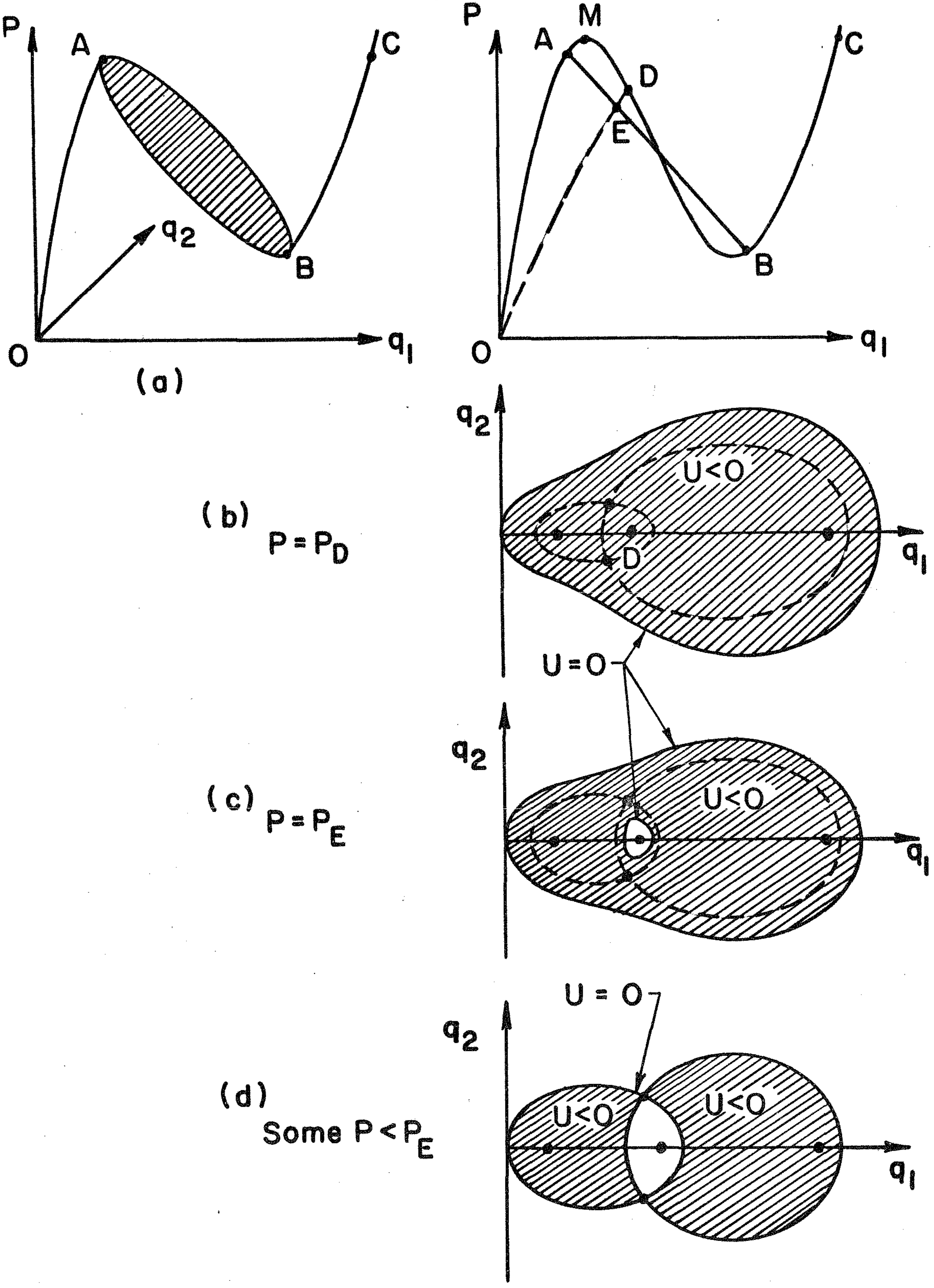

FIG.3 NONLINEAR RESPONSE OF TWO DEGREES OF FREEDOM SYSTEM

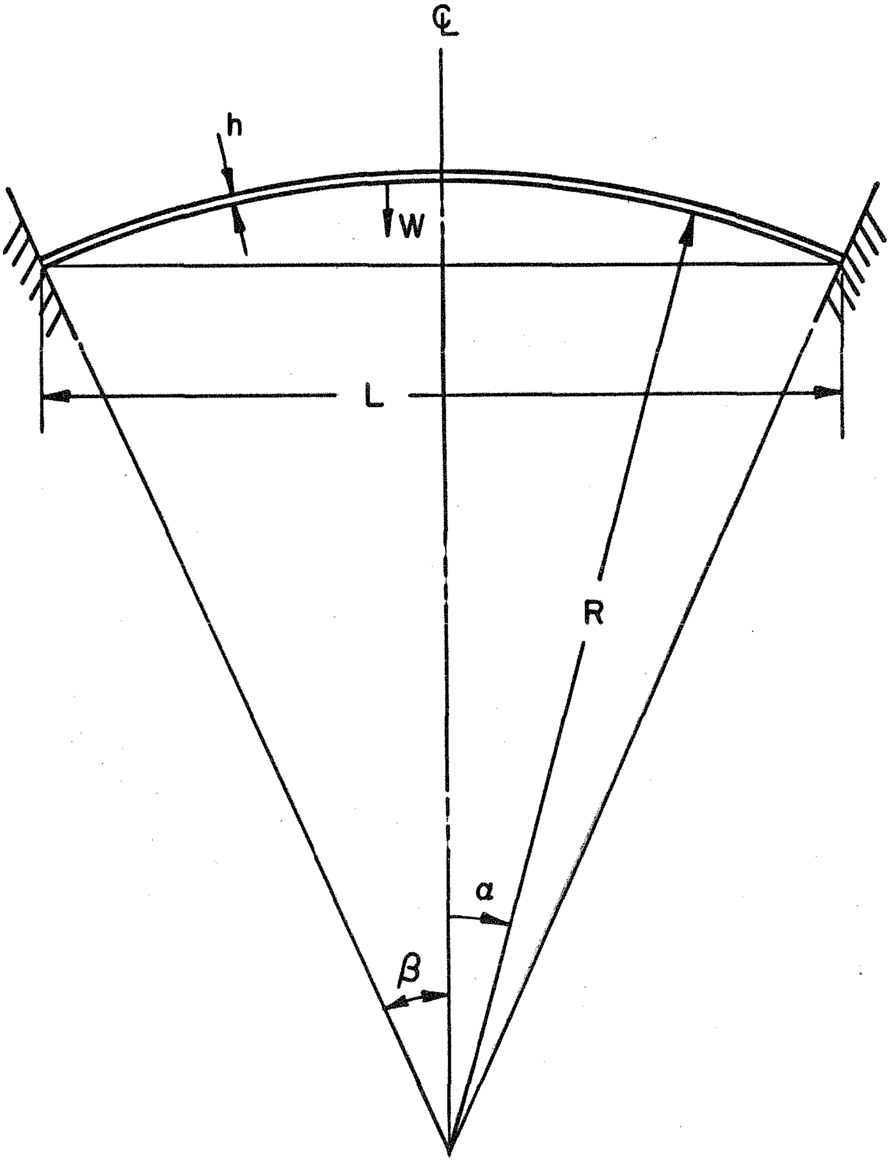

FIG. 4 COORDINATE SYSTEM OF CIRCULAR ARCH

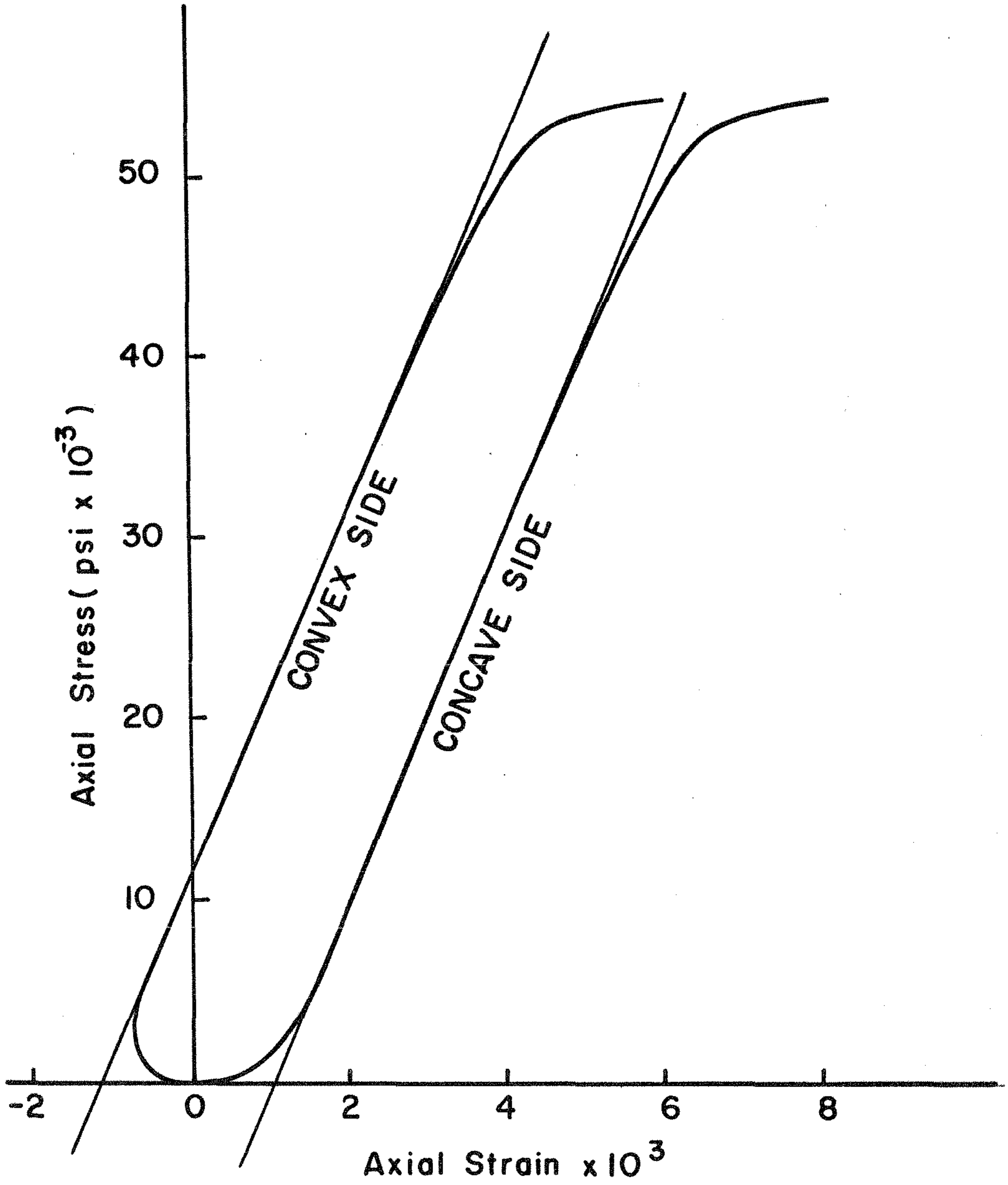

FIG. 5 TYPICAL TENSILE TEST OF CURVED 2024 ALUMINUM SPECIMEN

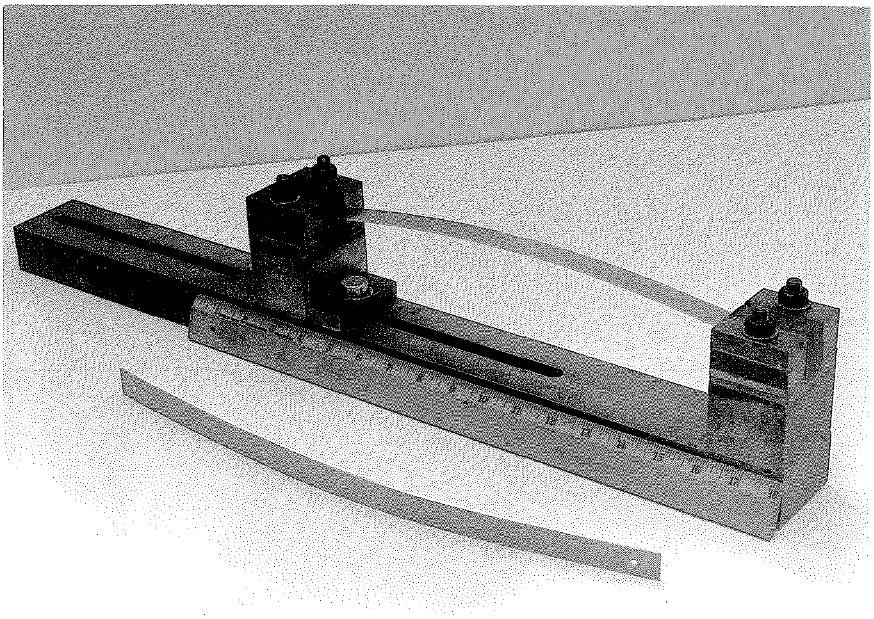

FIG. 6. CIRCULAR ARCH BEFORE AND AFTER INSTALLATION IN STEEL FRAME.

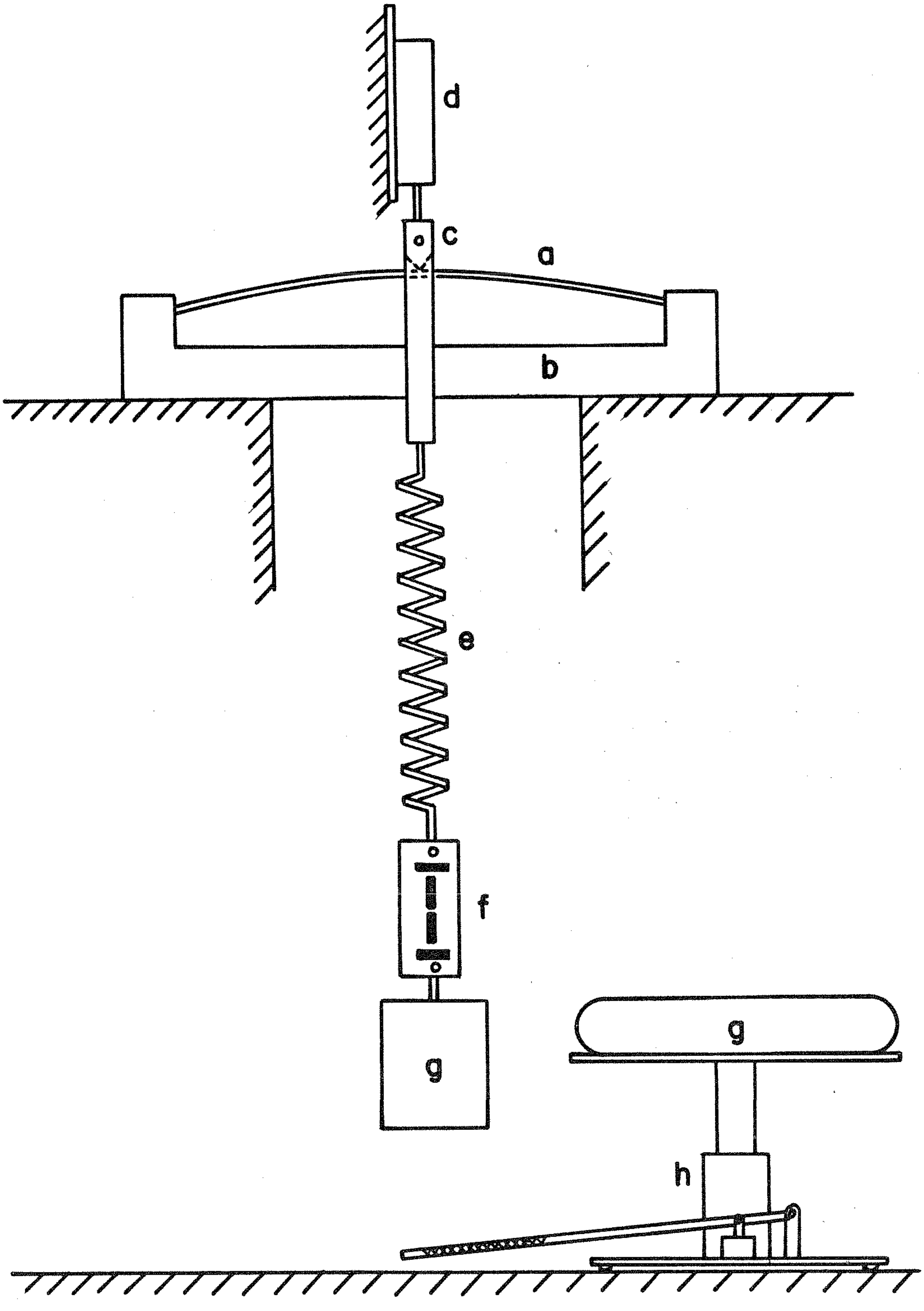

FIG.7 THE STATIC AND DYNAMIC TEST APPARATUS

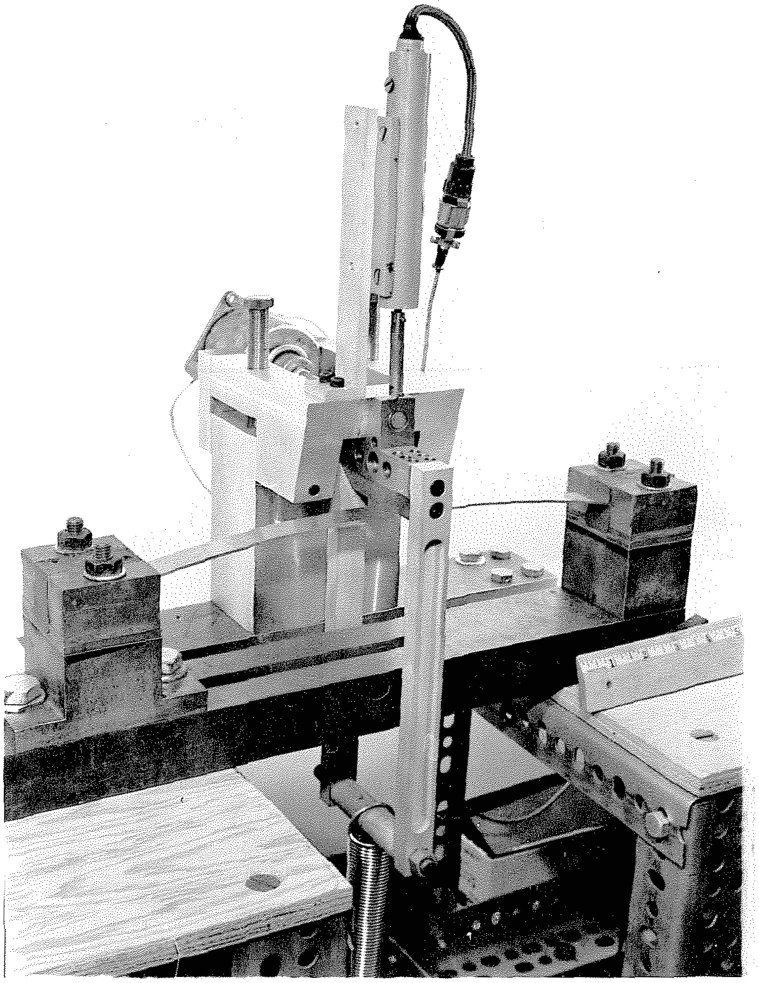

FIG. 8. KNIFE EDGE ASSEMBLY

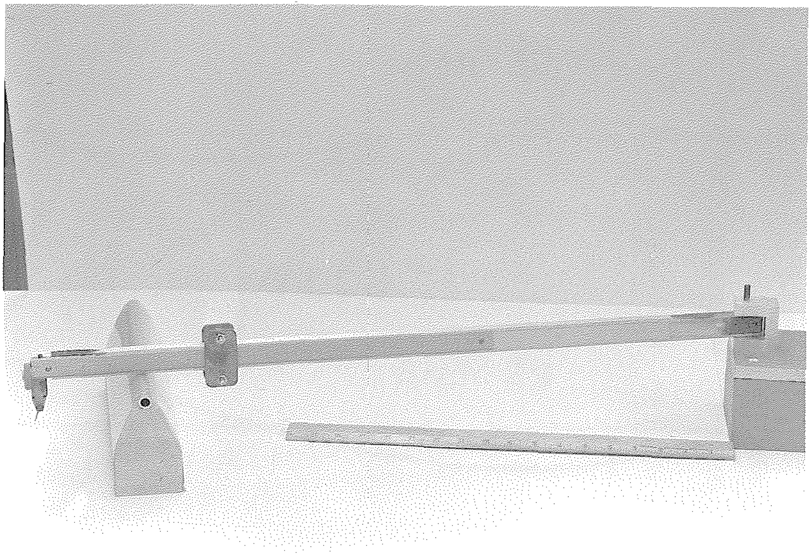

FIG. 9. INITIAL IMPERFECTION MEASURING EQUIPMENT

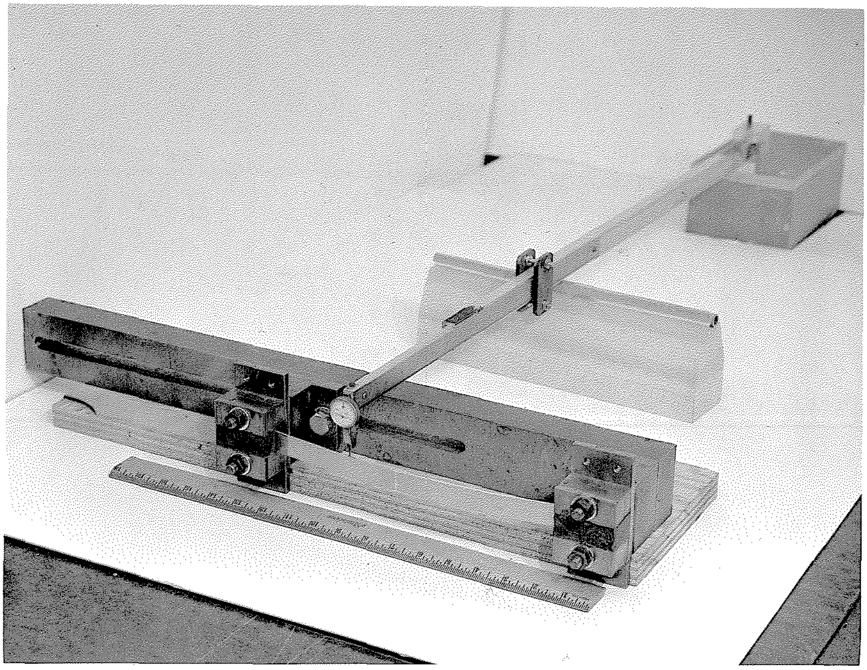

FIG. 10. MEASURING OF INITIAL IMPERFECTION OF CIRCULAR ARCH

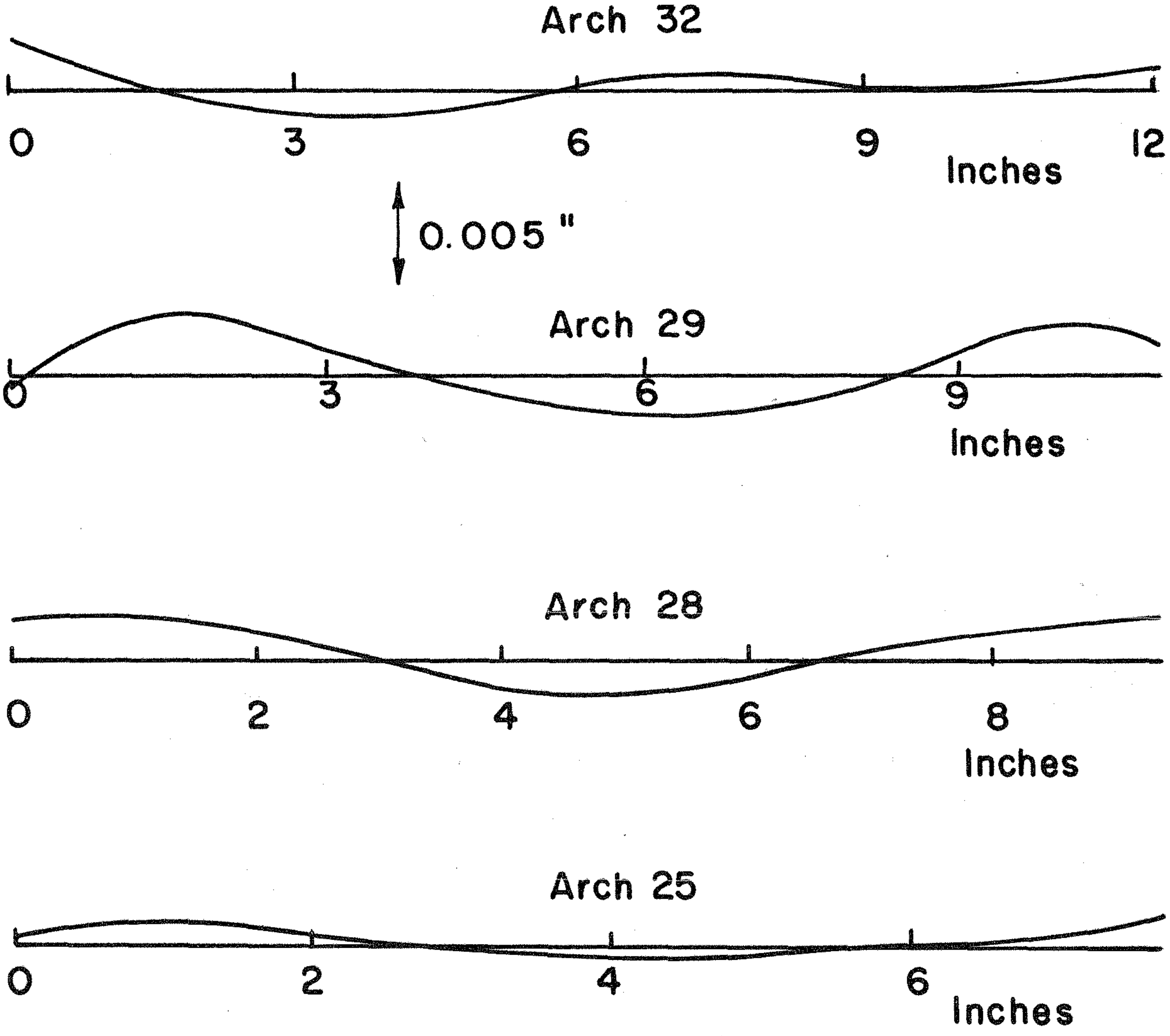

FIG. 11 IMPERFECTIONS OF THE TESTED ARCHES

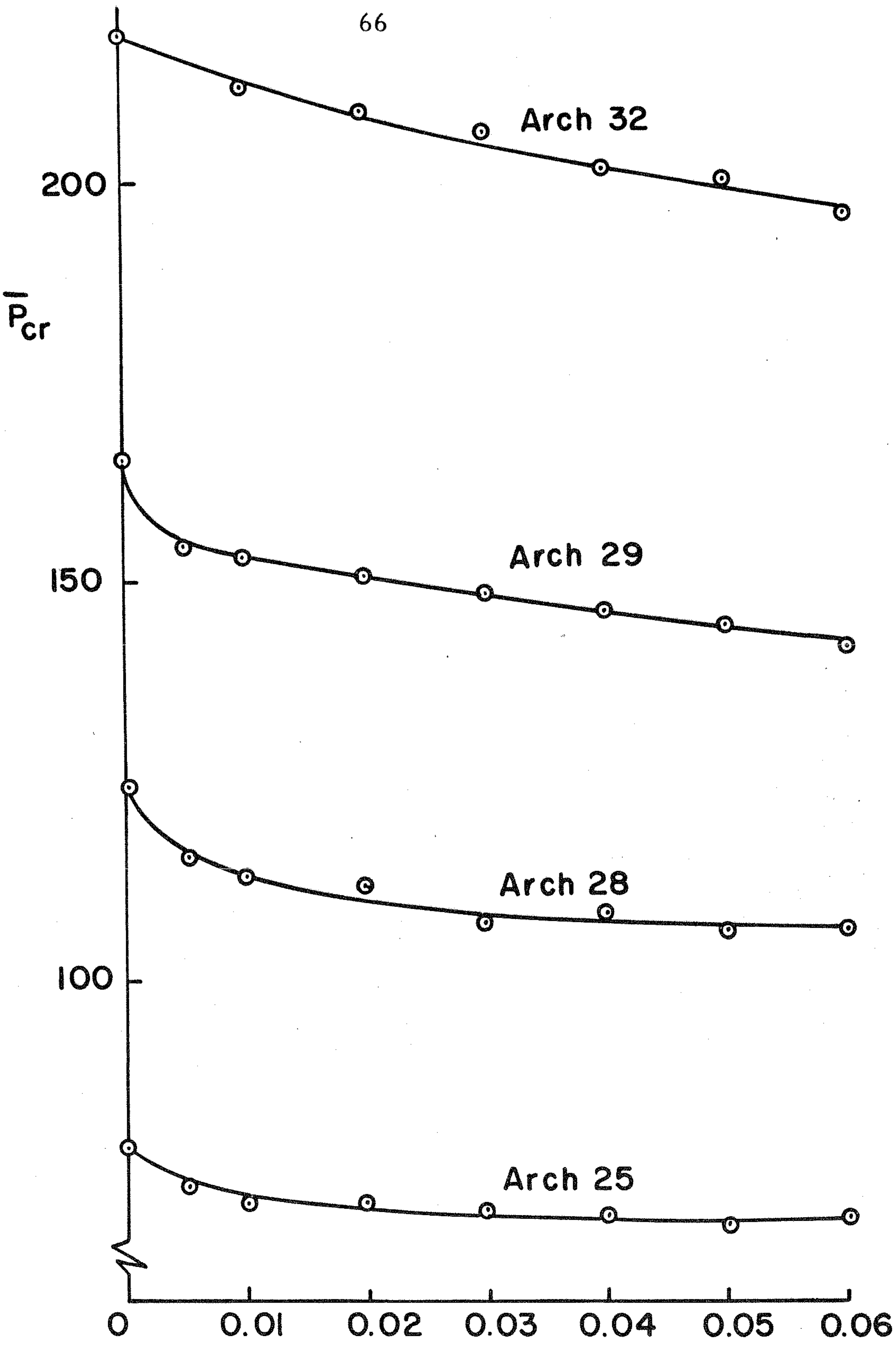

FIG.12 NONDIMENSIONAL CRITICAL STATIC LOAD VS. LOADING IMPERFECTION

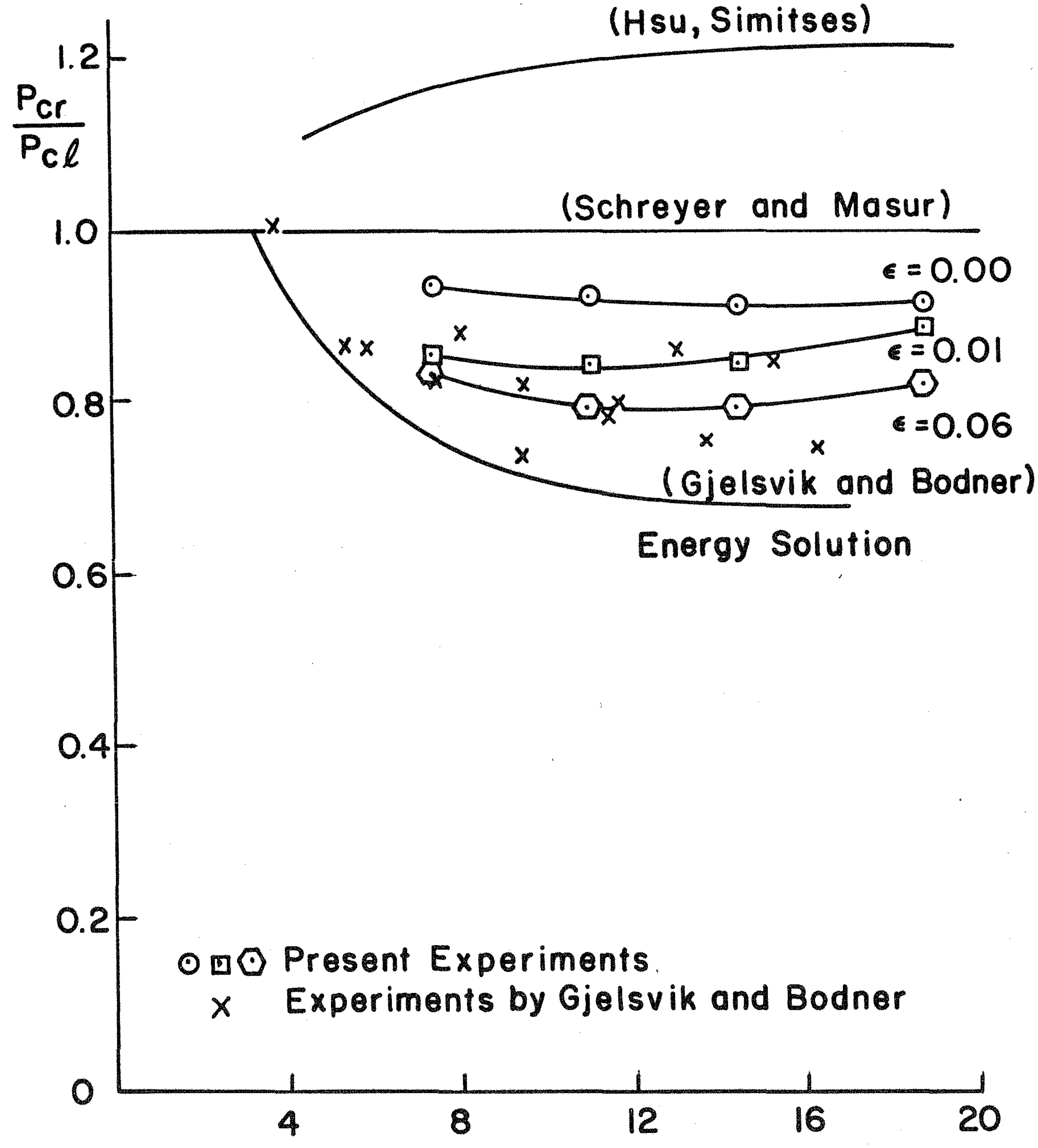

FIG. 13 COMPARISON OF STATIC EXPERIMENTS TO THEORETICAL STATIC BUCKLING LOAD

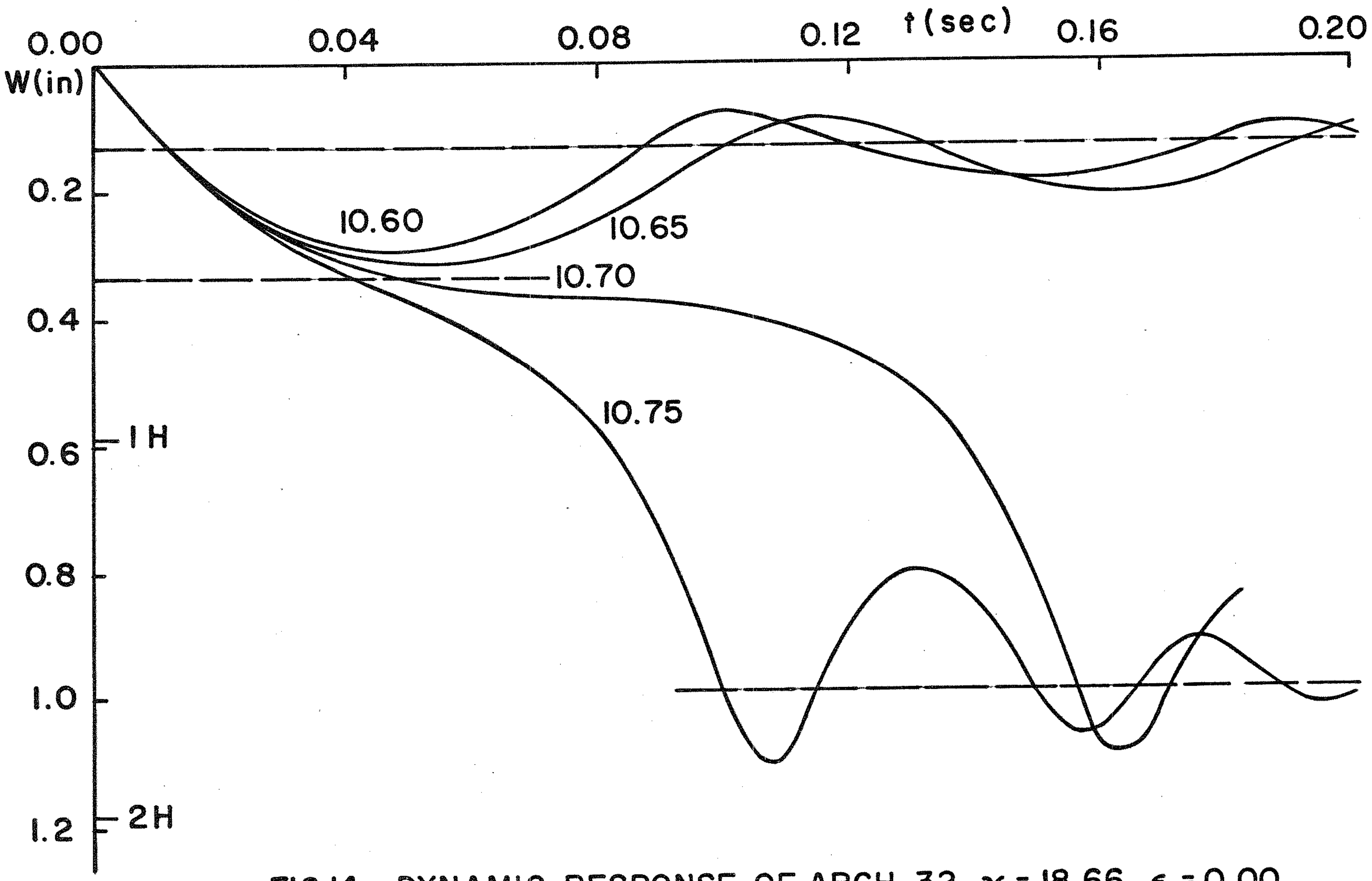

FIG.14a DYNAMIC RESPONSE OF ARCH 32, $\gamma = 18.66$, $\epsilon = 0.00$

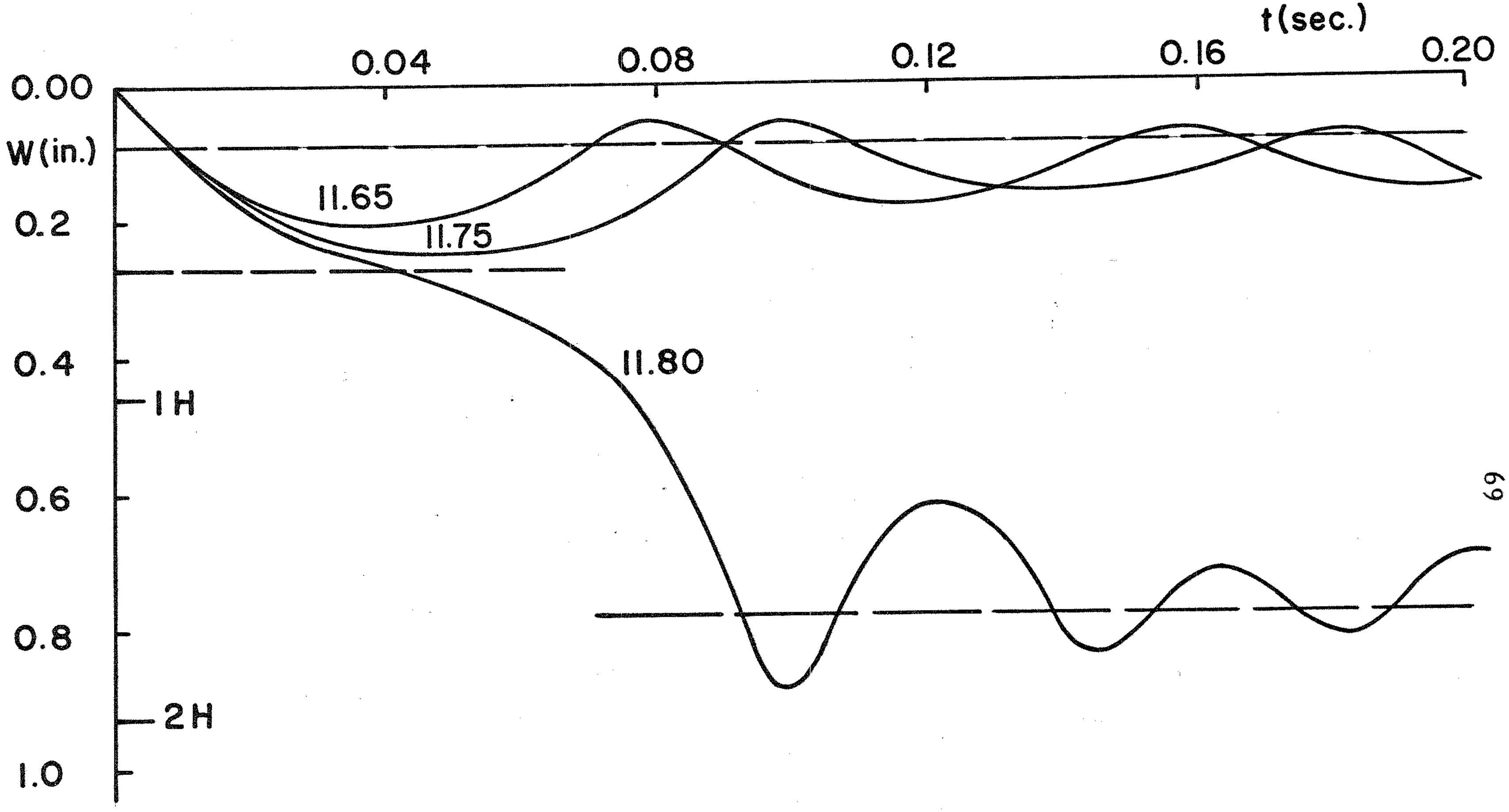

FIG.14b DYNAMIC RESPONSE OF ARCH 29, γ = 14.40, ϵ = 0.00

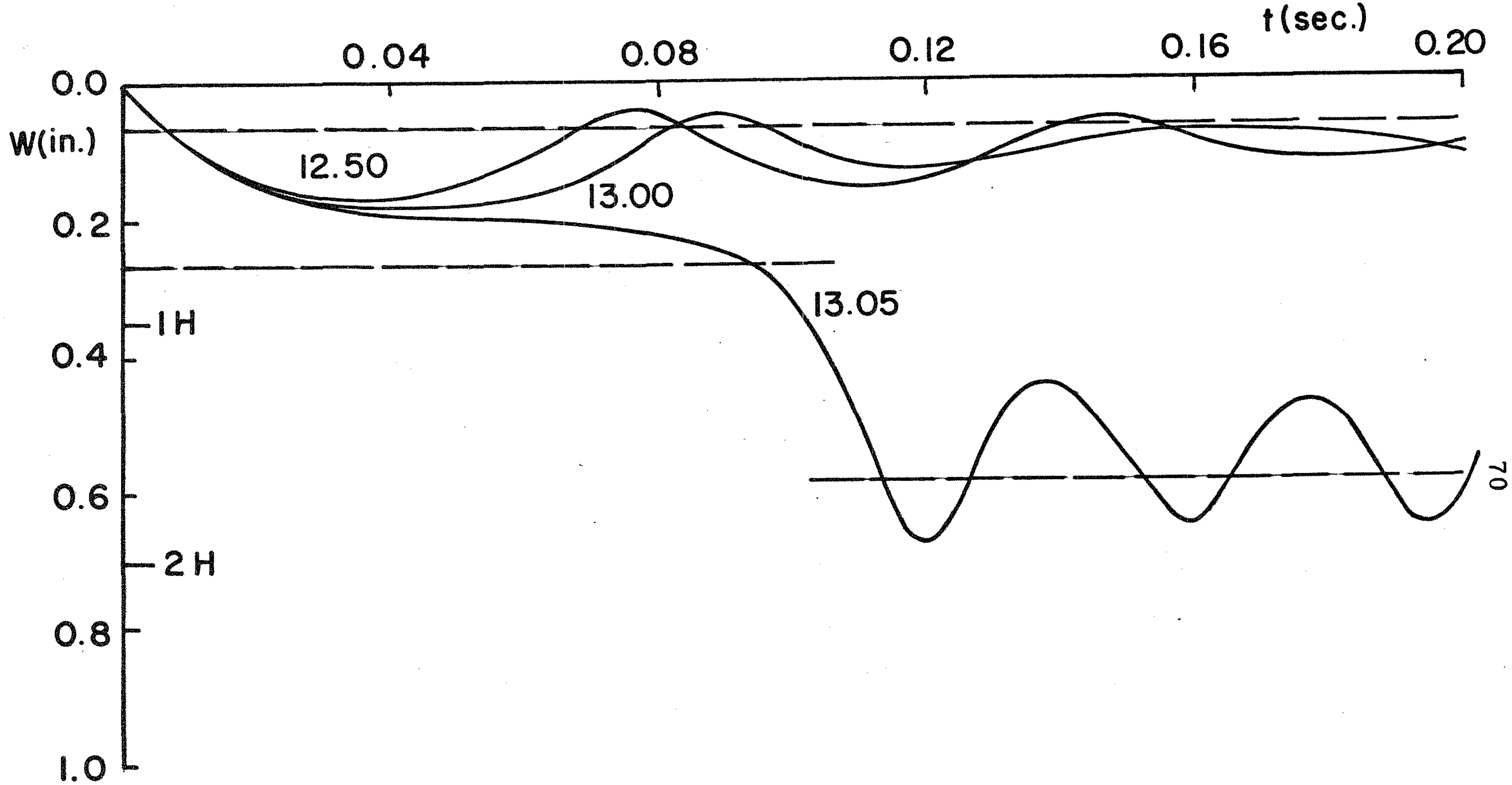

FIG.14c DYNAMIC RESPONSE OF ARCH 28, $\gamma=10.96$, $\epsilon=0.00$

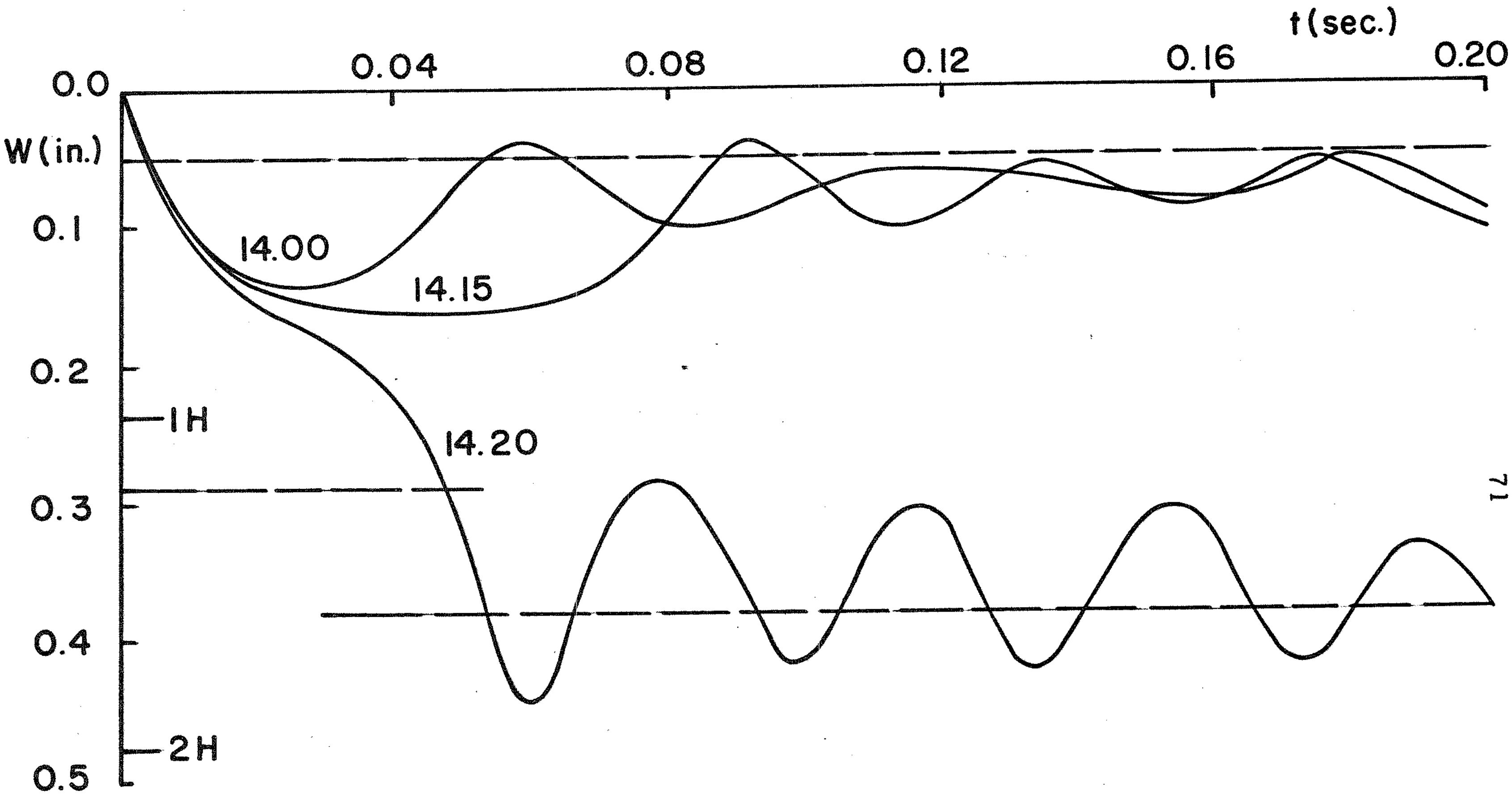

FIG.14d DYNAMIC RESPONSE OF ARCH 25, $\gamma = 7.40$, $\epsilon = 0.00$

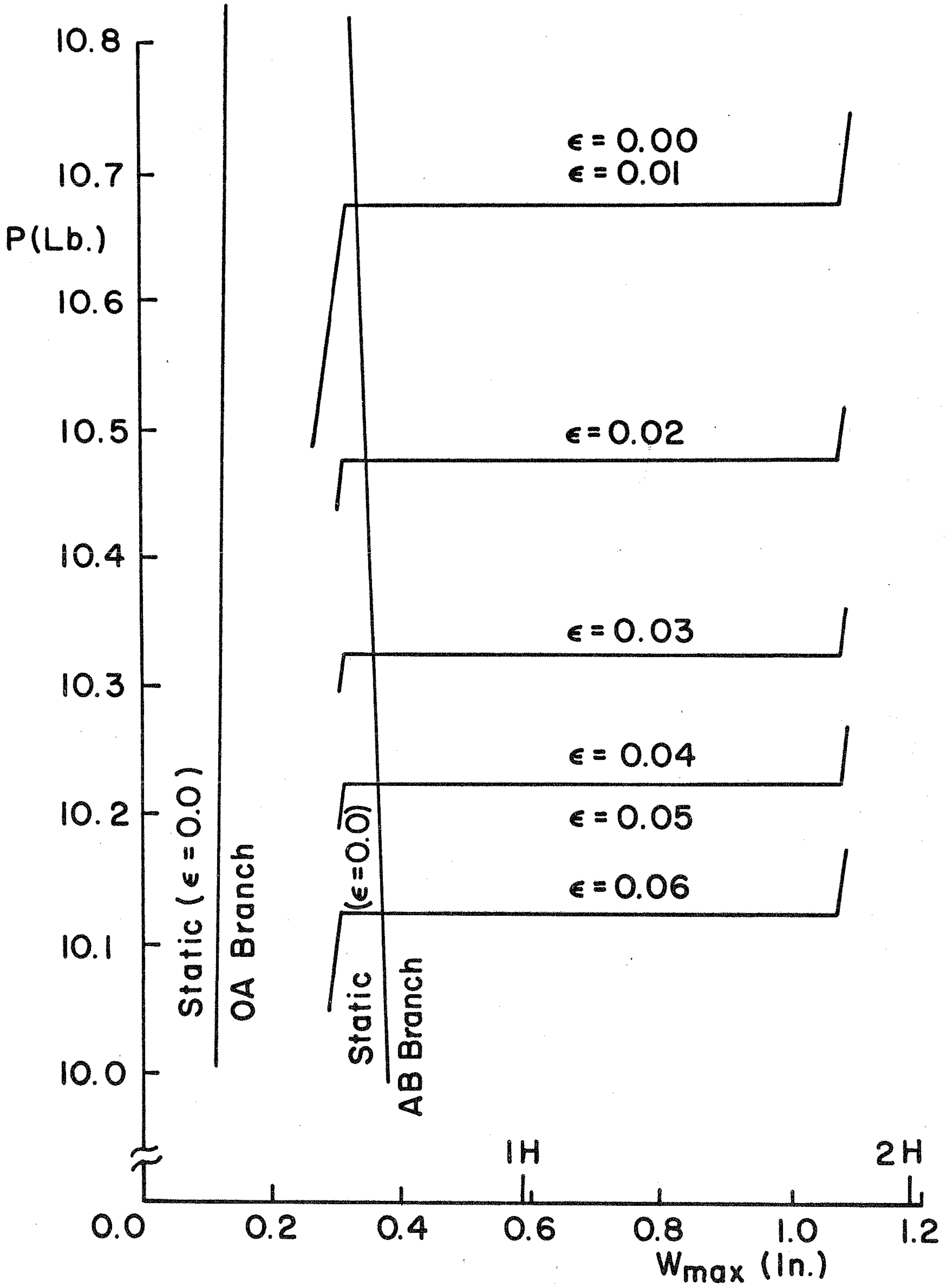

FIG.15a LOAD DEFLECTION CURVE FOR ARCH 32, γ=18.66

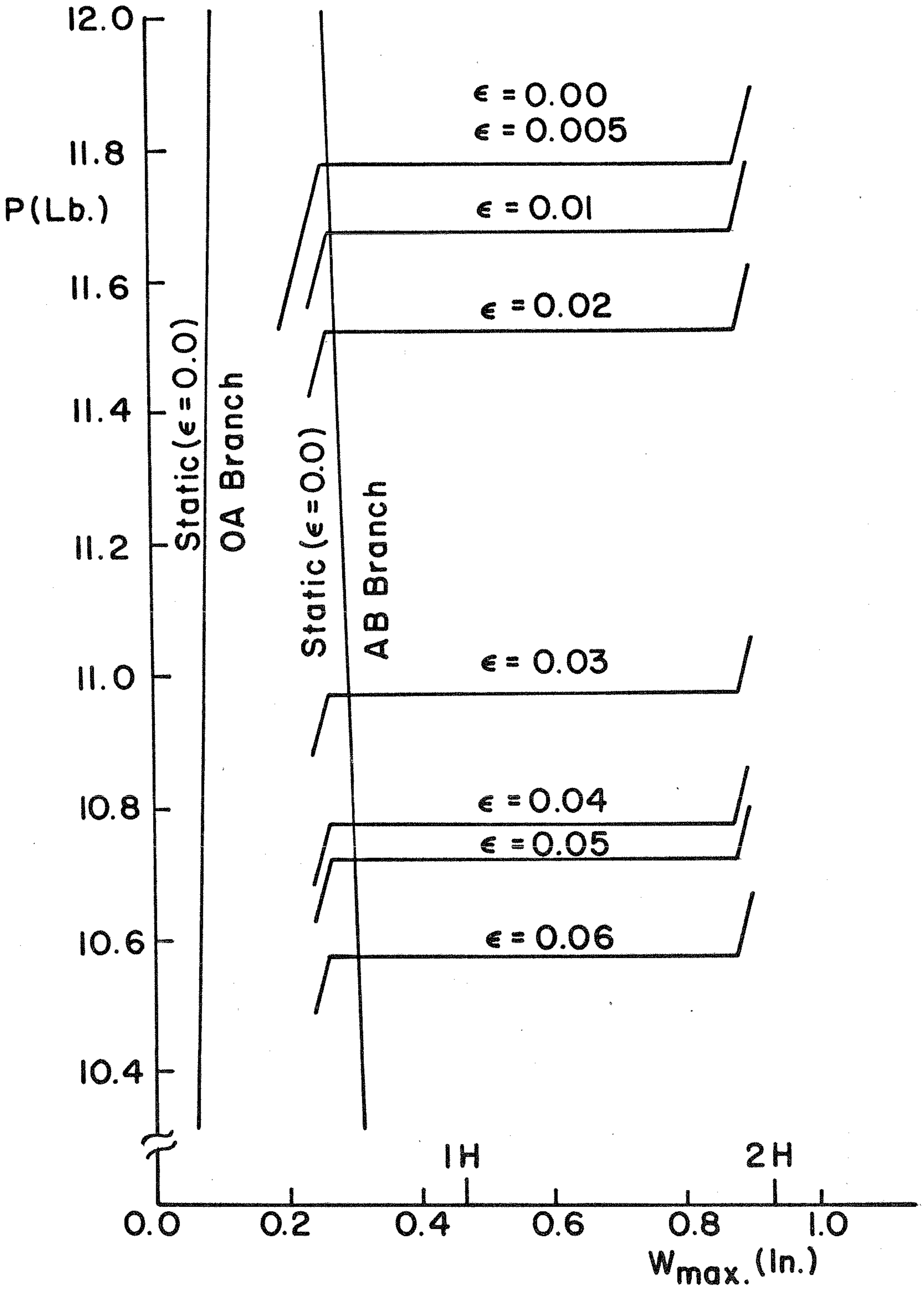

FIG.15b LOAD DEFLECTION CURVE FOR ARCH 29, $\gamma = 14.40$

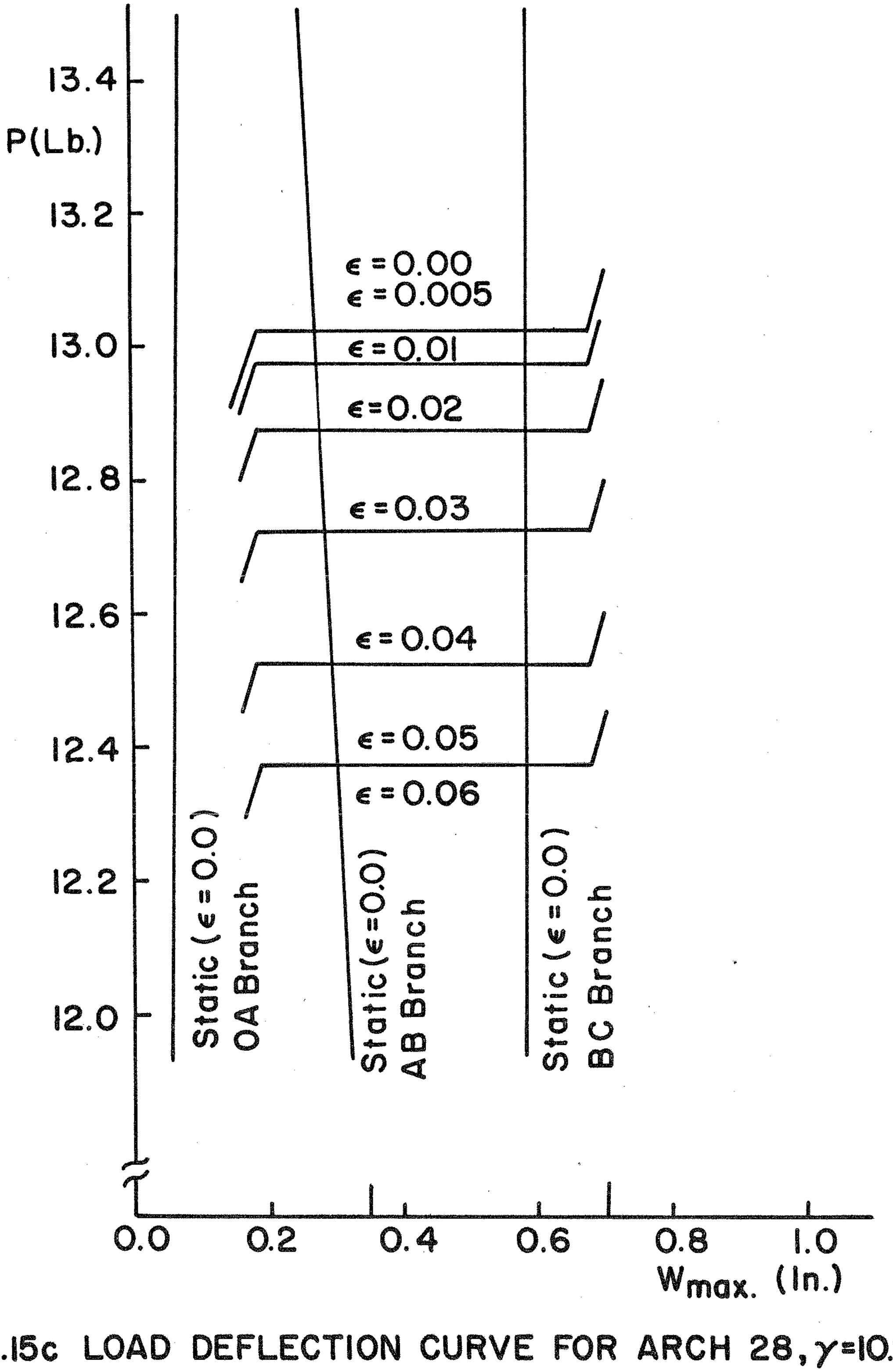

FIG.15c LOAD DEFLECTION CURVE FOR ARCH 28, γ=10.96

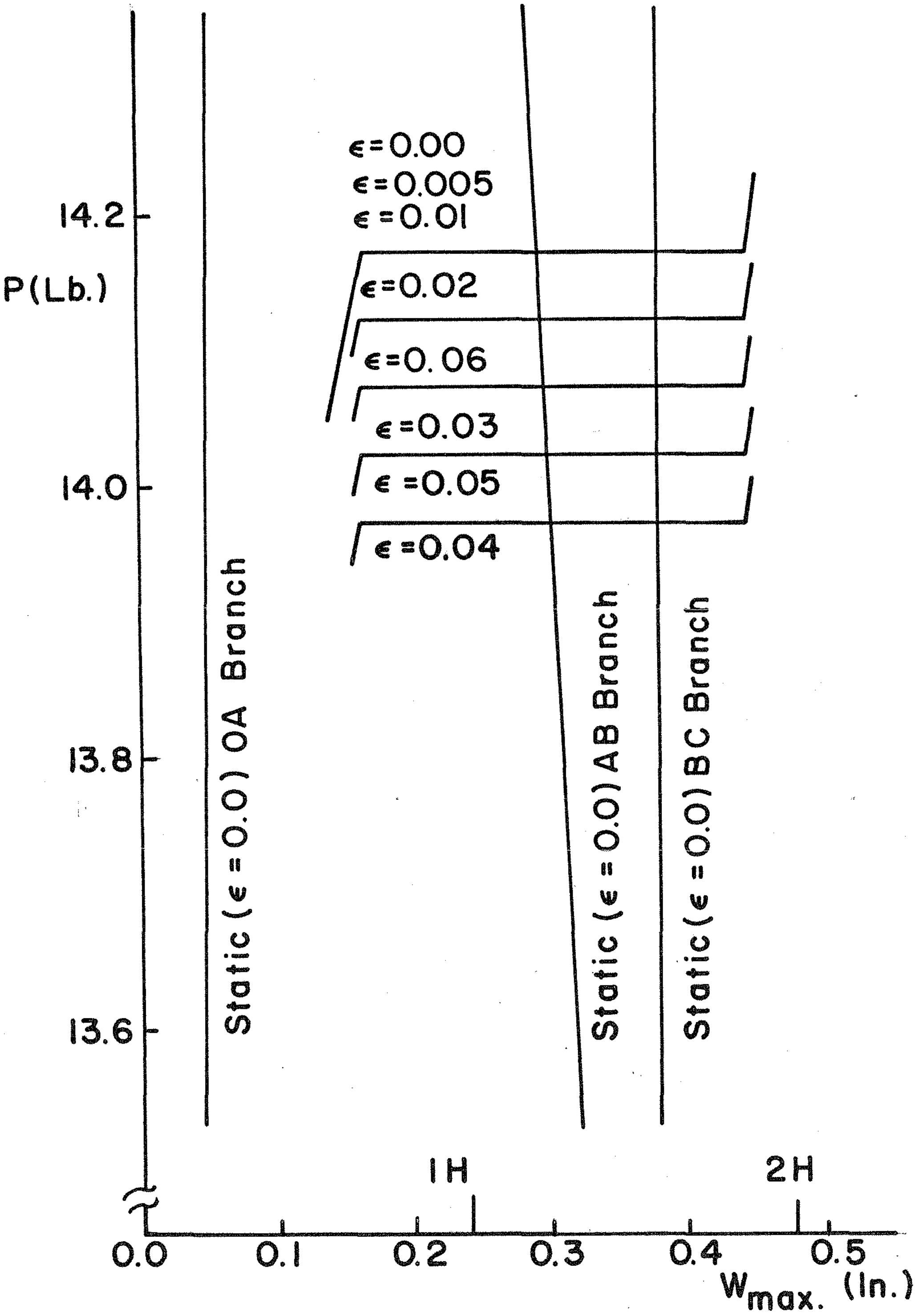

FIG.15d LOAD DEFLECTION CURVE FOR ARCH 25, $\gamma = 7.40$

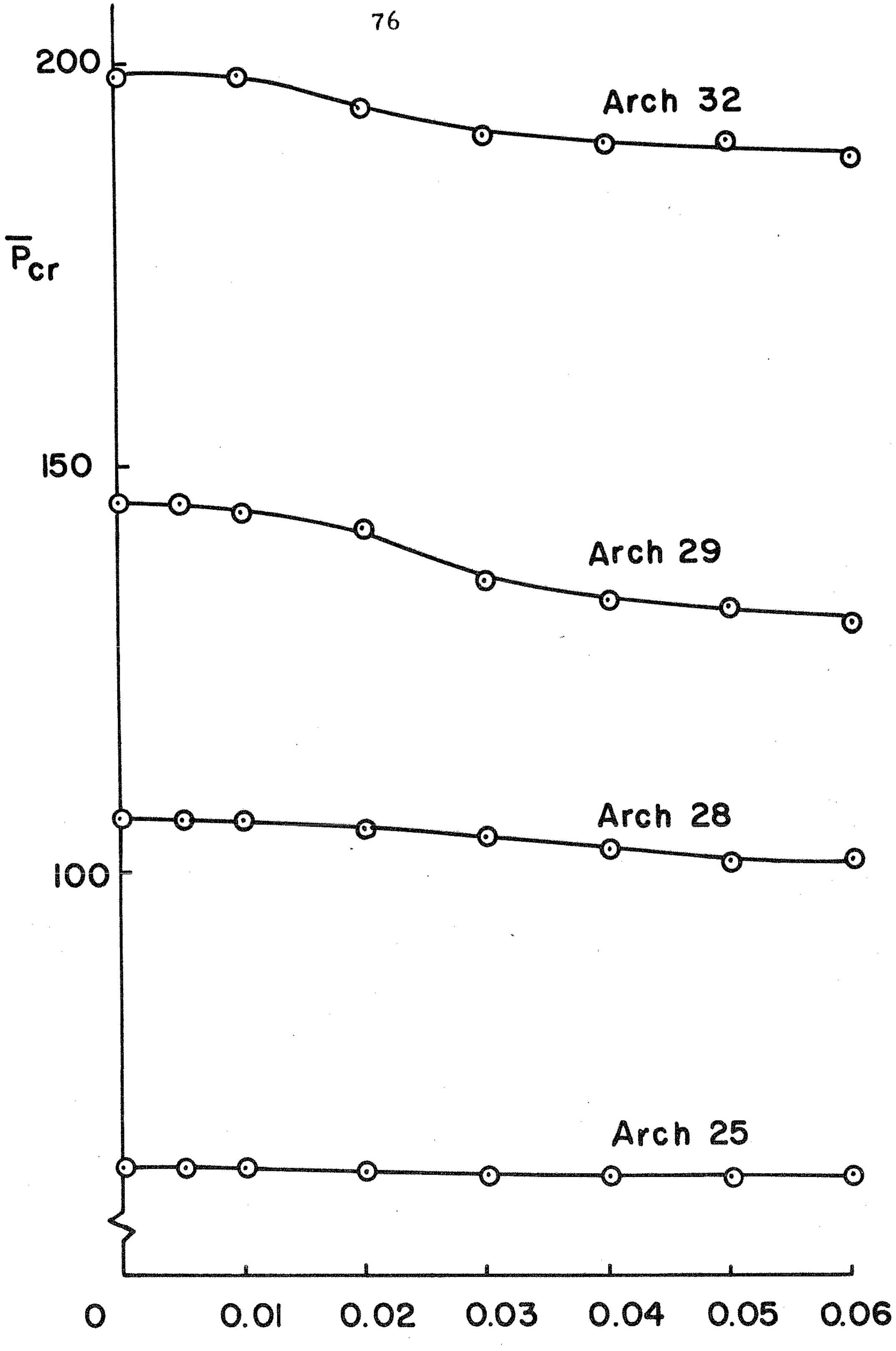

FIG. 16 NONDIMENSIONAL CRITICAL STEP LOAD VS. LOADING IMPERFECTION

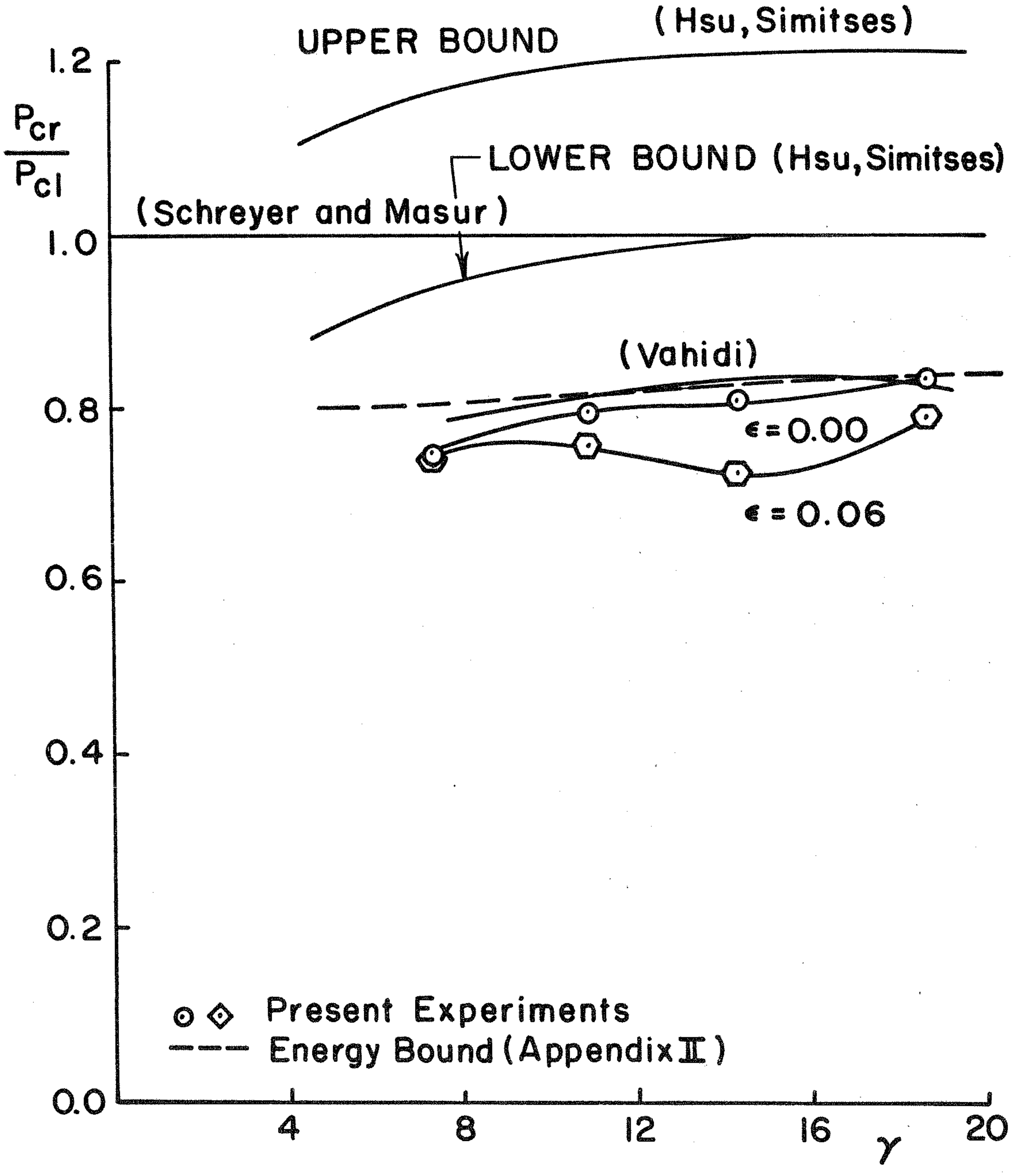

FIG. 17 COMPARISON OF DYNAMIC EXPERIMENT TO THEORETICAL STEP BUCKLING LOAD

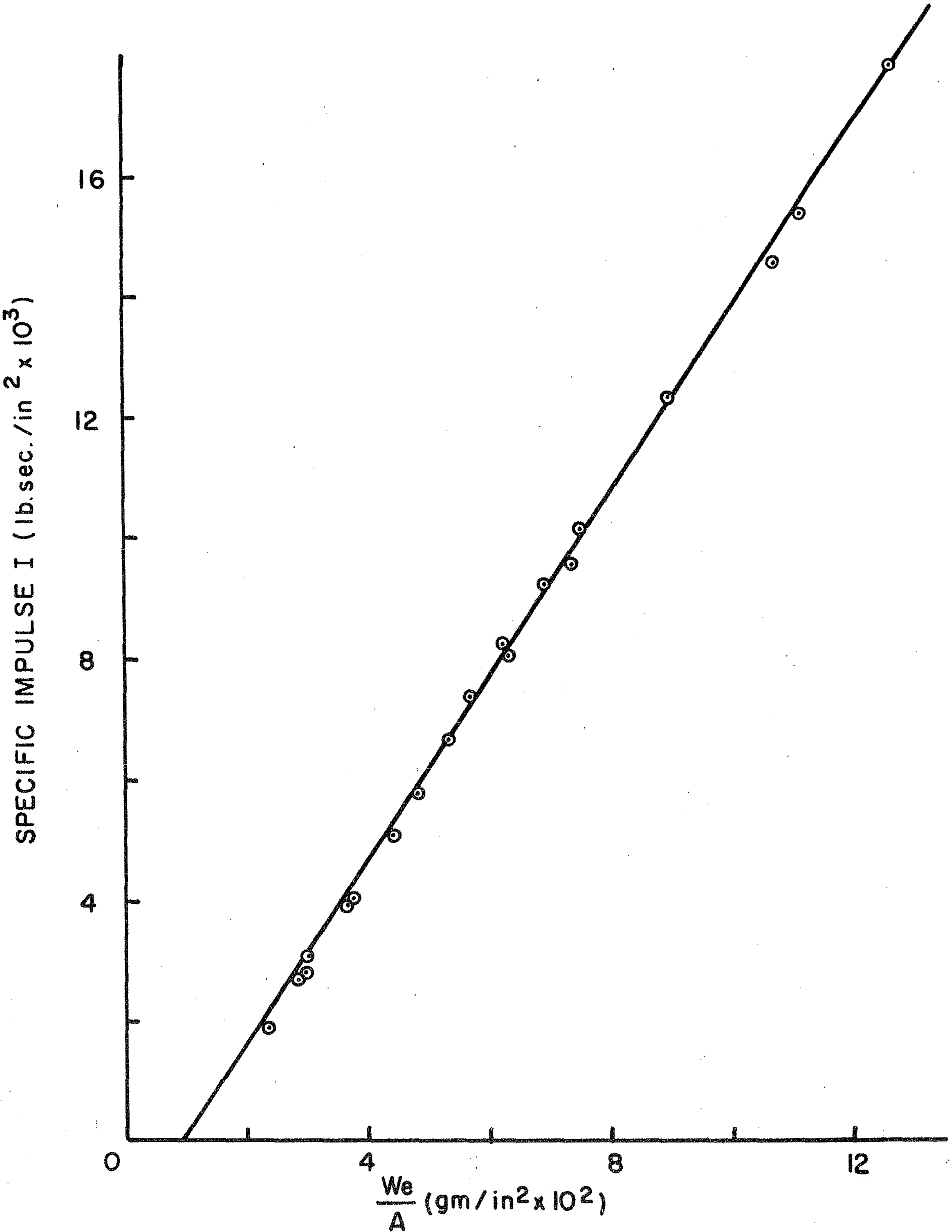

FIG. 18 CALIBRATION OF EXPLOSIVE (SILVER ACETYLIDE - SILVER NITRATE)

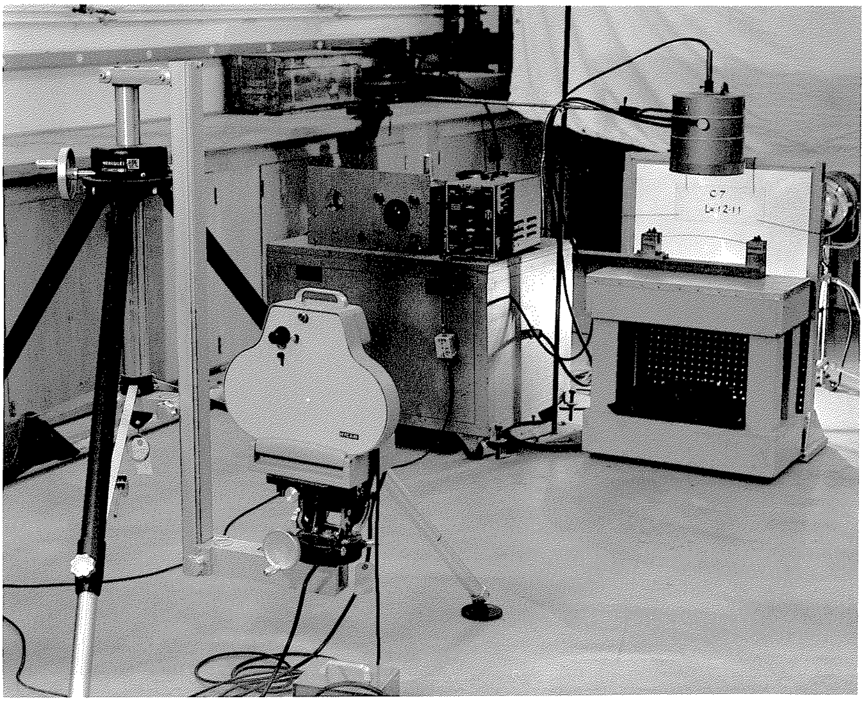

FIG. 19. CAMERA SETUP

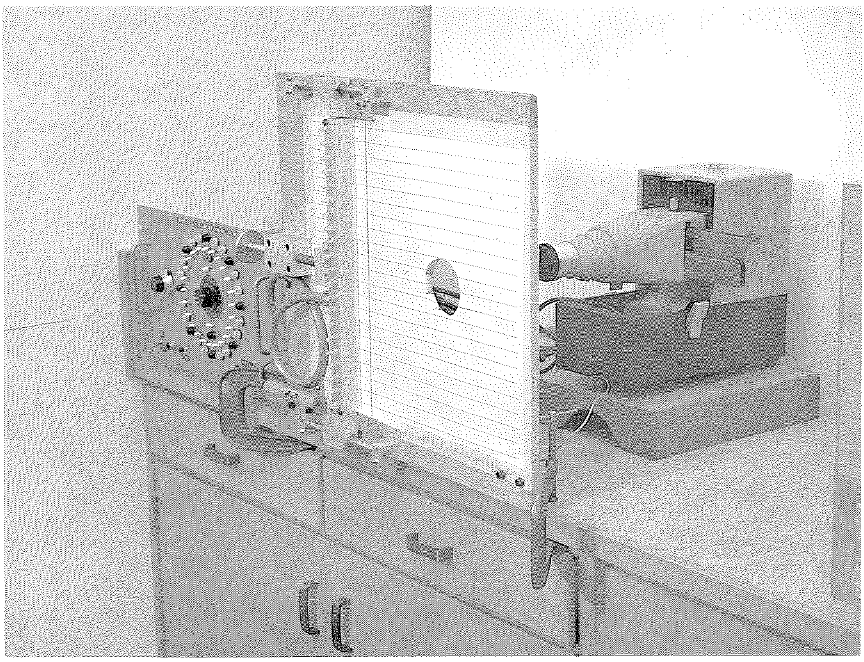

FIG. 20. FILM READER TO MEASURE DEFORMED ARCH SHAPE

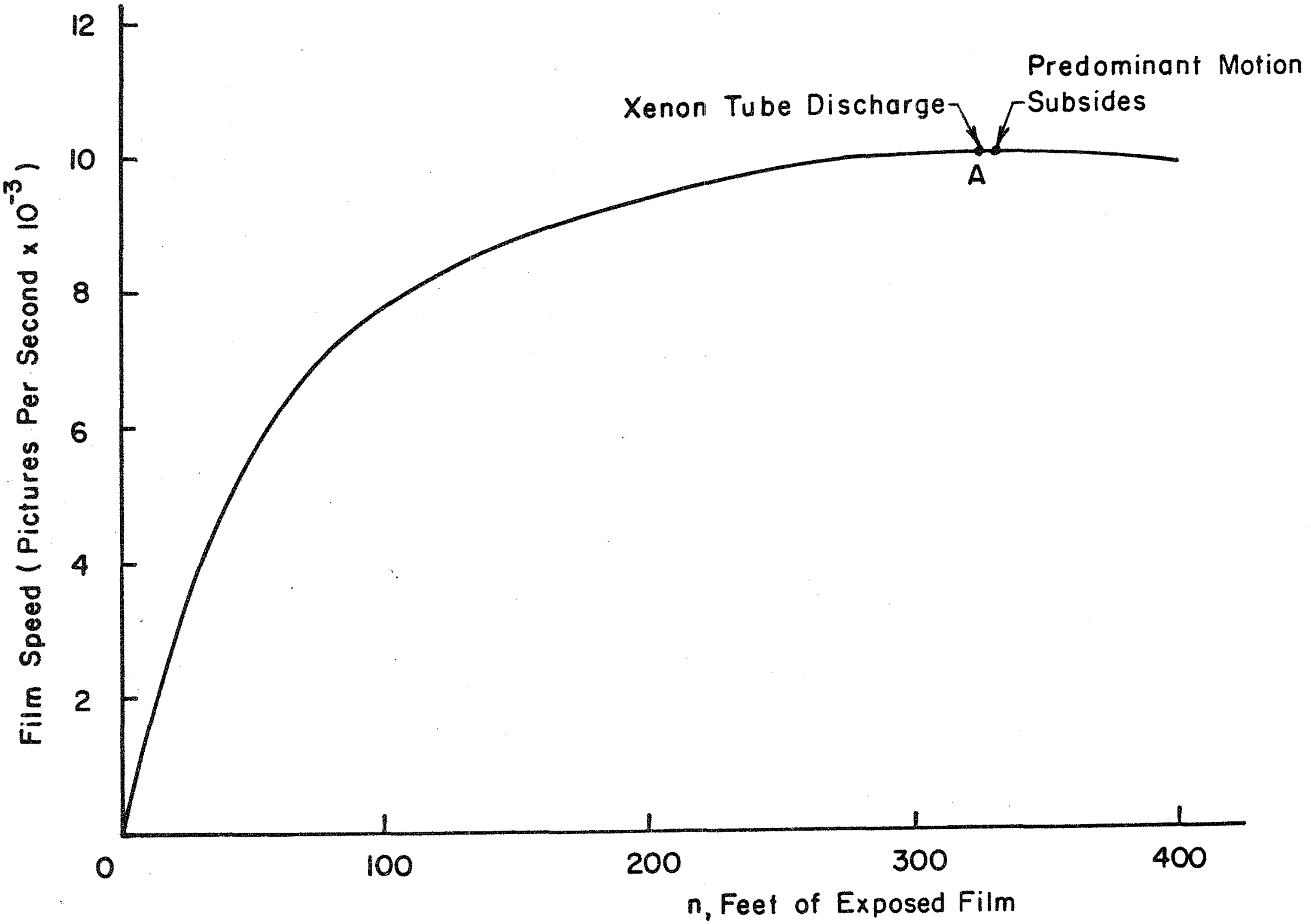

FIG. 21 PERFORMANCE AND SYNCHRONIZATION OF THE HIGH SPEED CAMERA

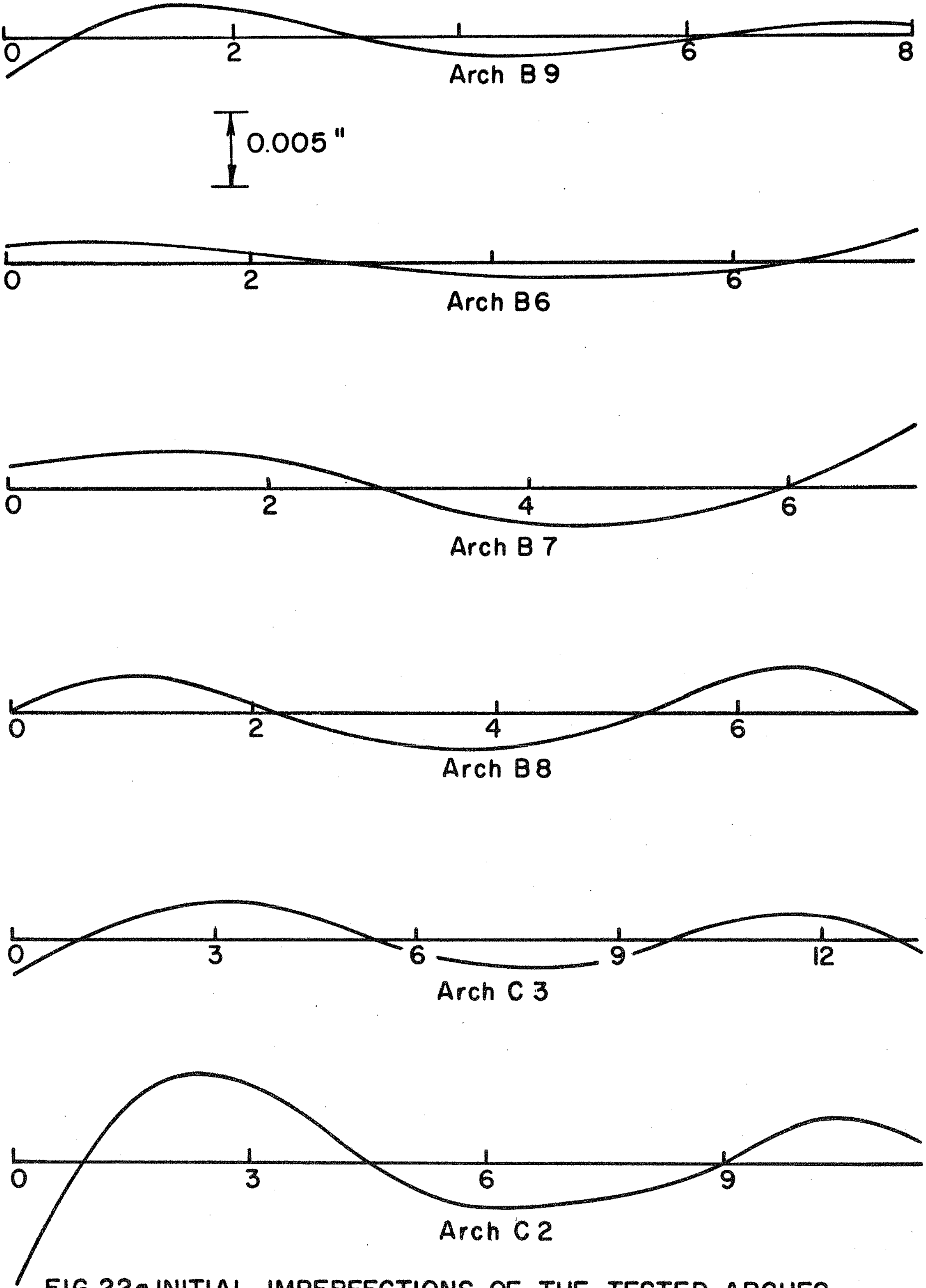

FIG. 22a INITIAL IMPERFECTIONS OF THE TESTED ARCHES

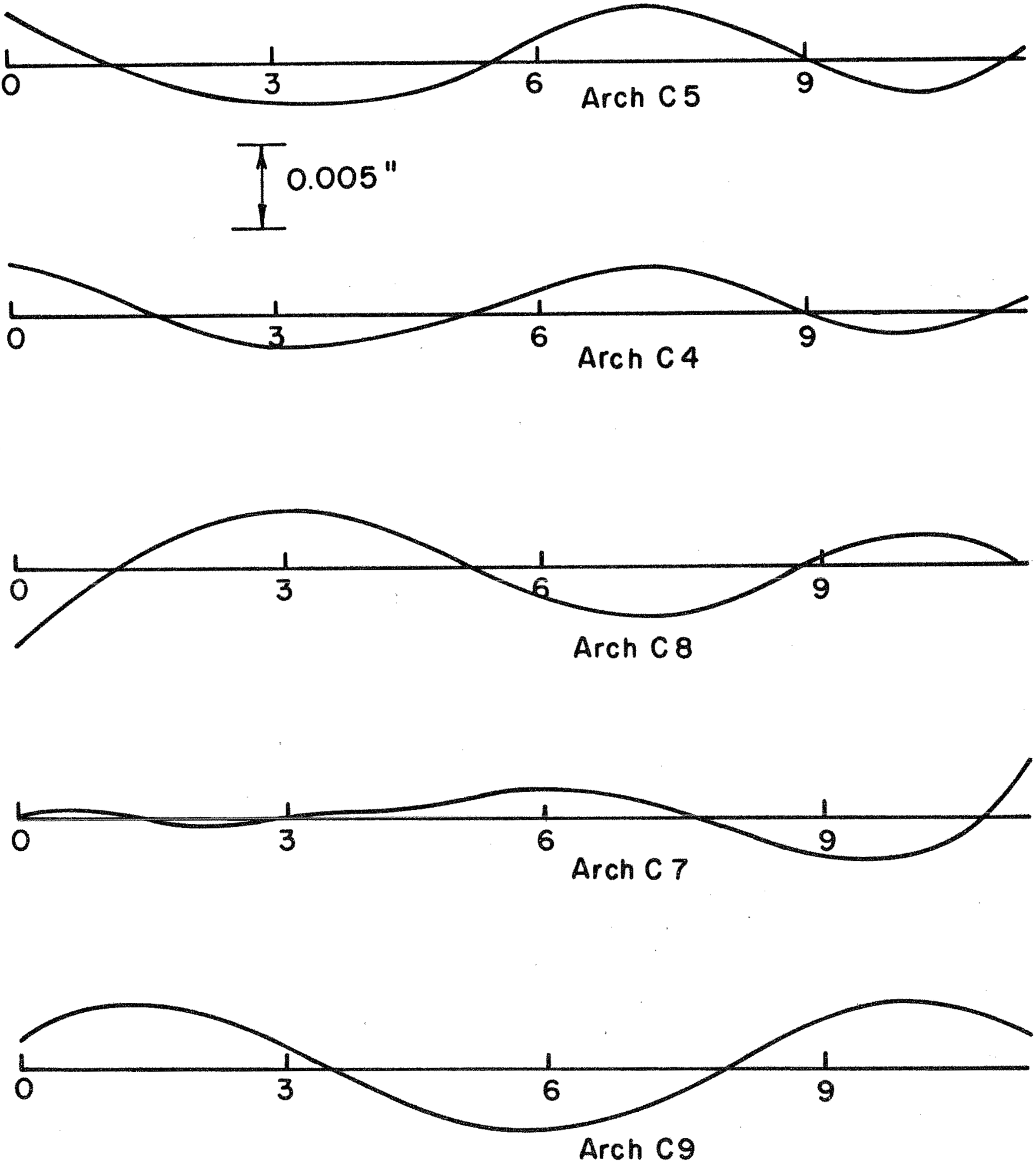

FIG.22b INITIAL IMPERFECTIONS OF THE TESTED ARCHES

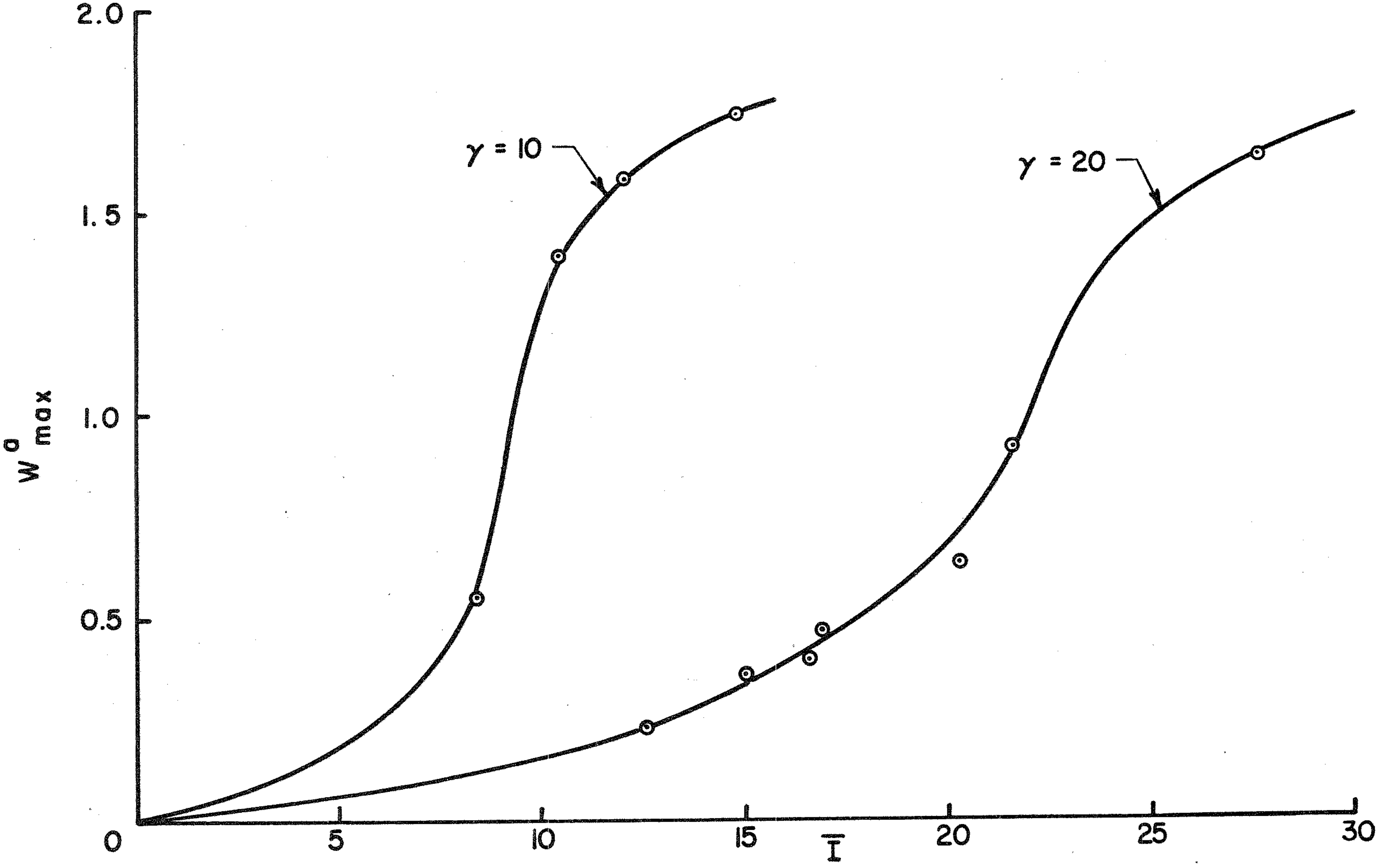

FIG.23 IMPULSE VS. MAXIMUM AVERAGE DISPLACEMENT FOR CLAMPED ARCH

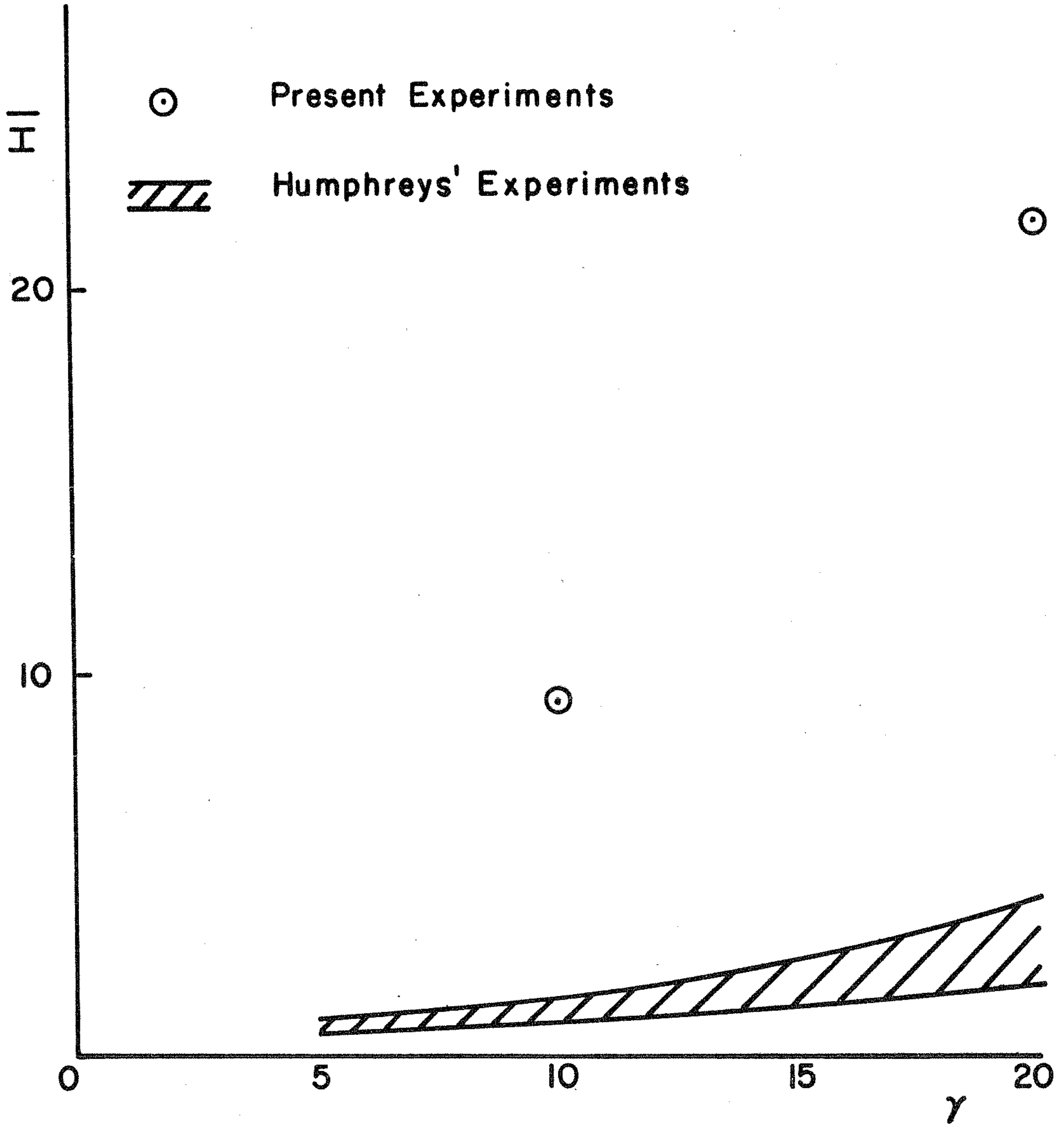

FIG.24 COMPARISON OF THE PRESENT RESULTS WITH HUMPHREYS' EXPERIMENTS

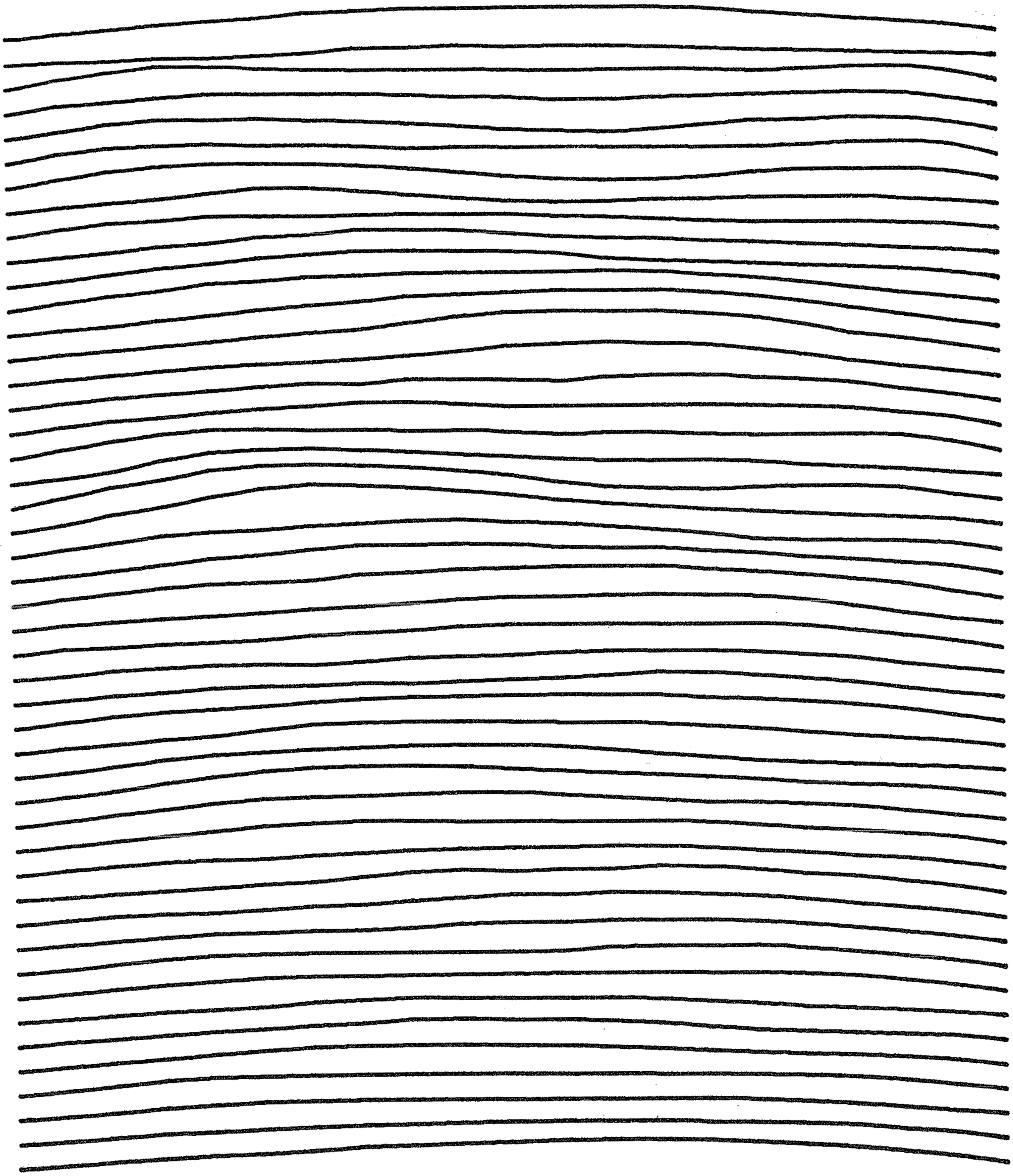

FIG. 25a DEFORMED SHAPES OF ARCH B 9

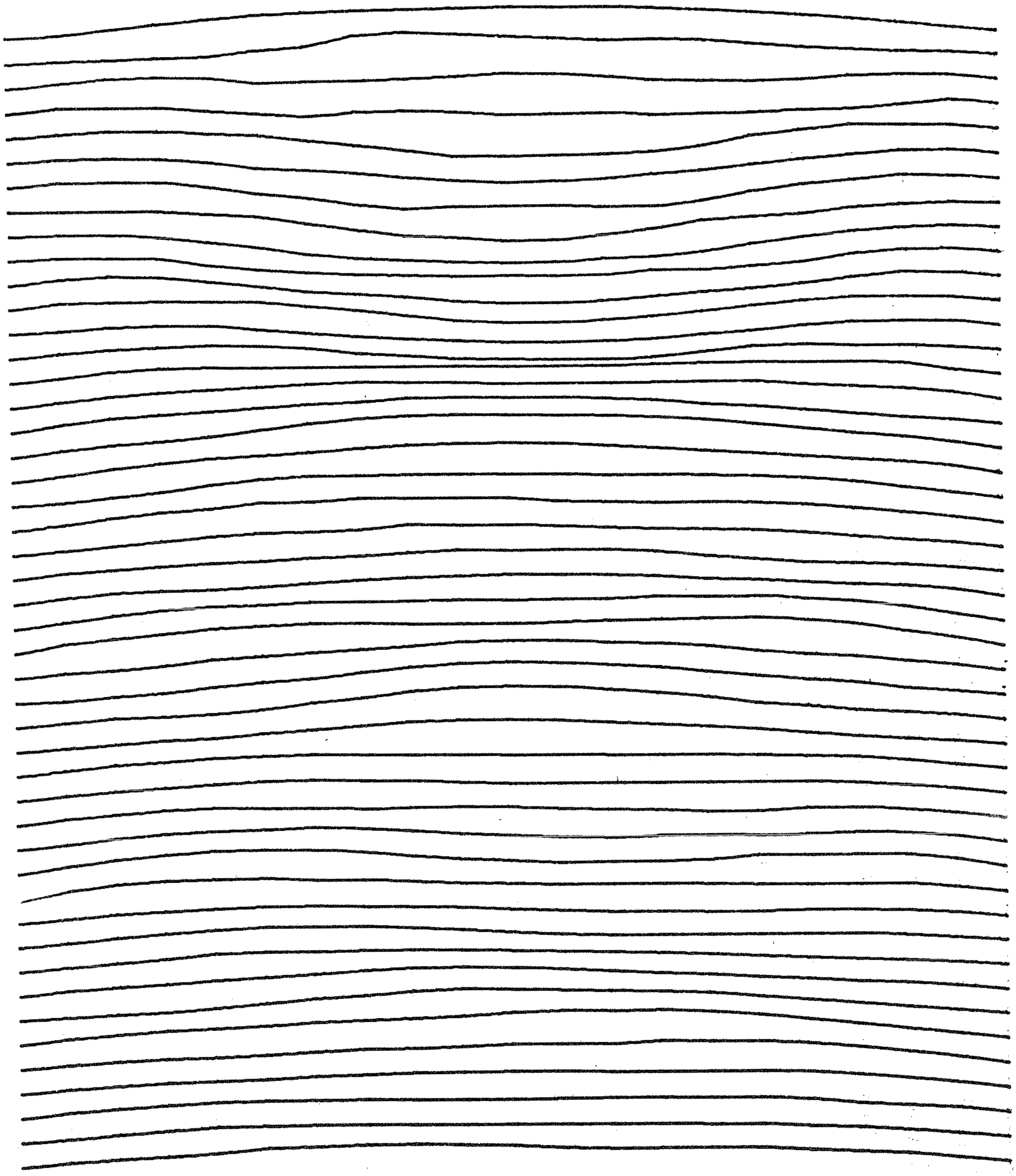

FIG. 25 b DEFORMED SHAPES OF ARCH B8

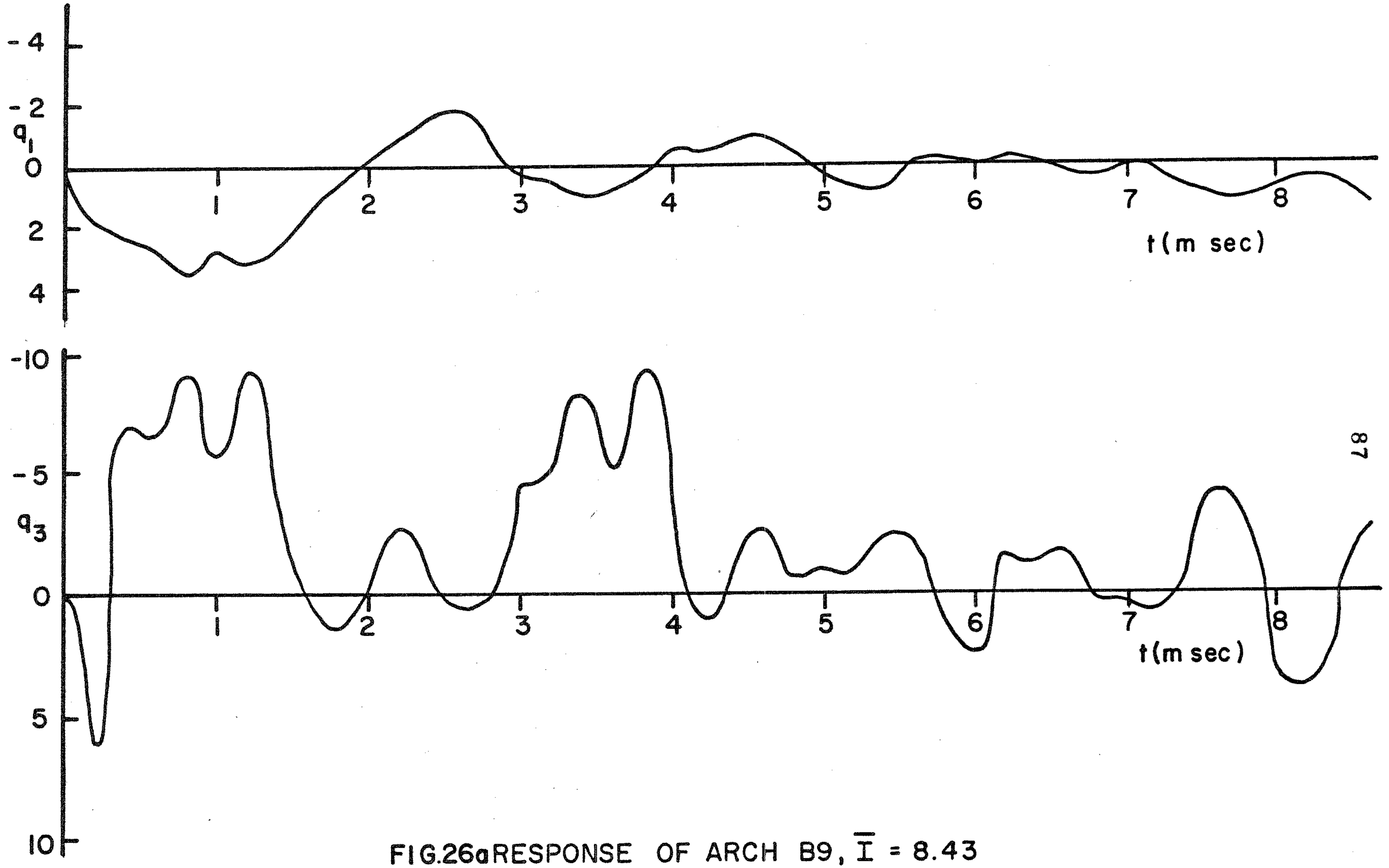

FIG.26a RESPONSE OF ARCH B9, $\overline{I}$ = 8.43

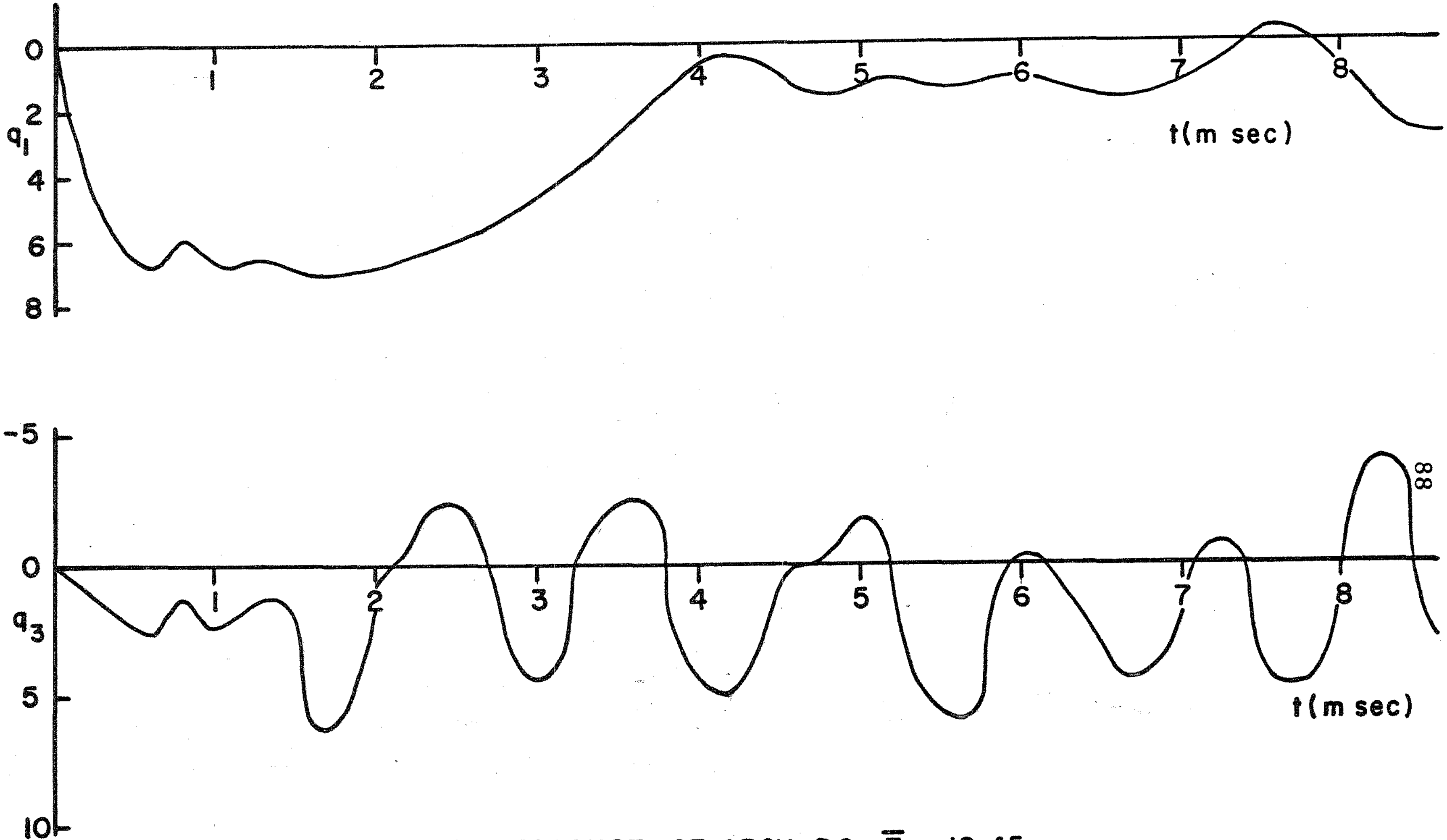

FIG.26b RESPONSE OF ARCH B6, $\overline{I}$ = 10.45

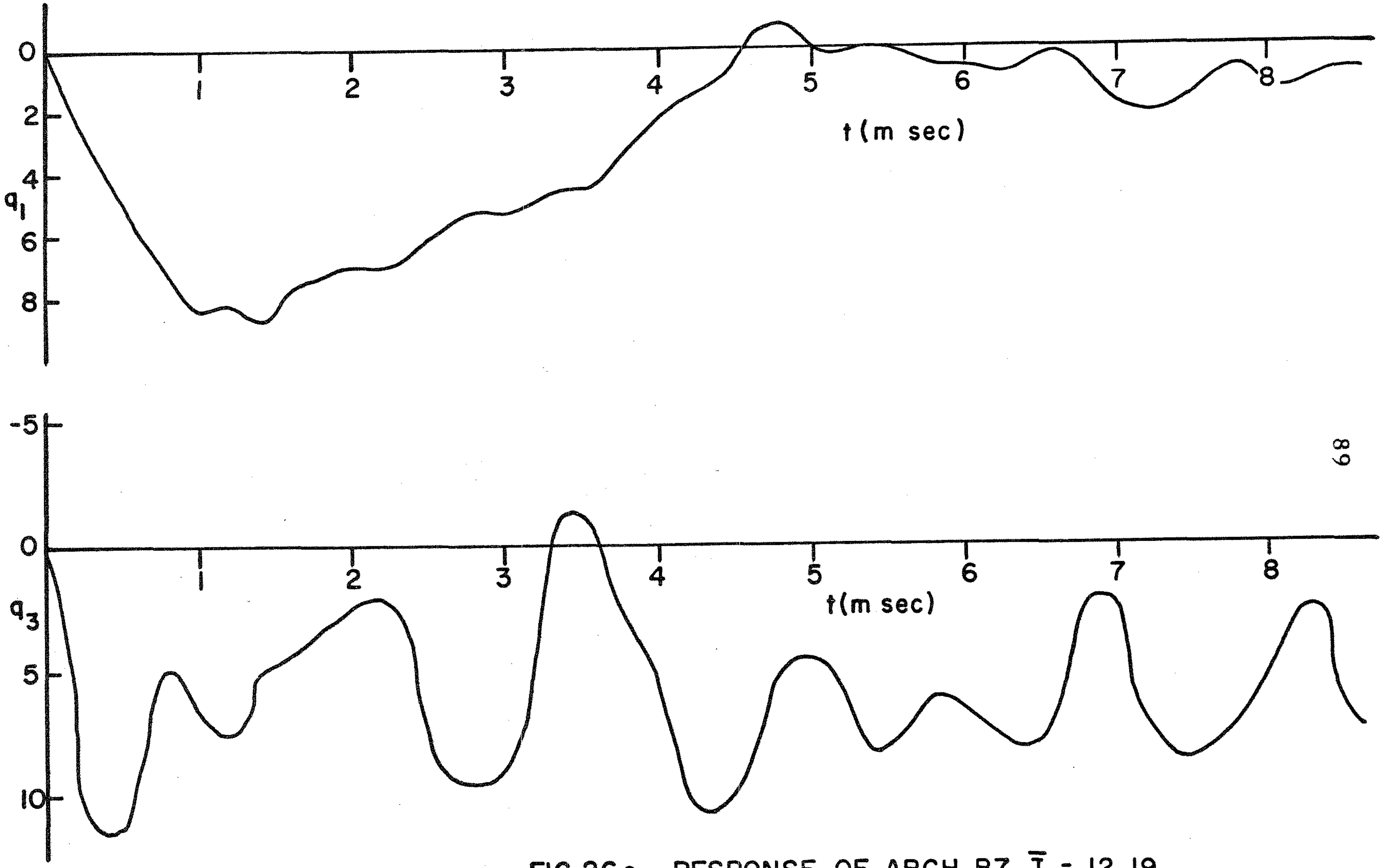

FIG.26c RESPONSE OF ARCH B7, $\overline{I}$ = 12.19

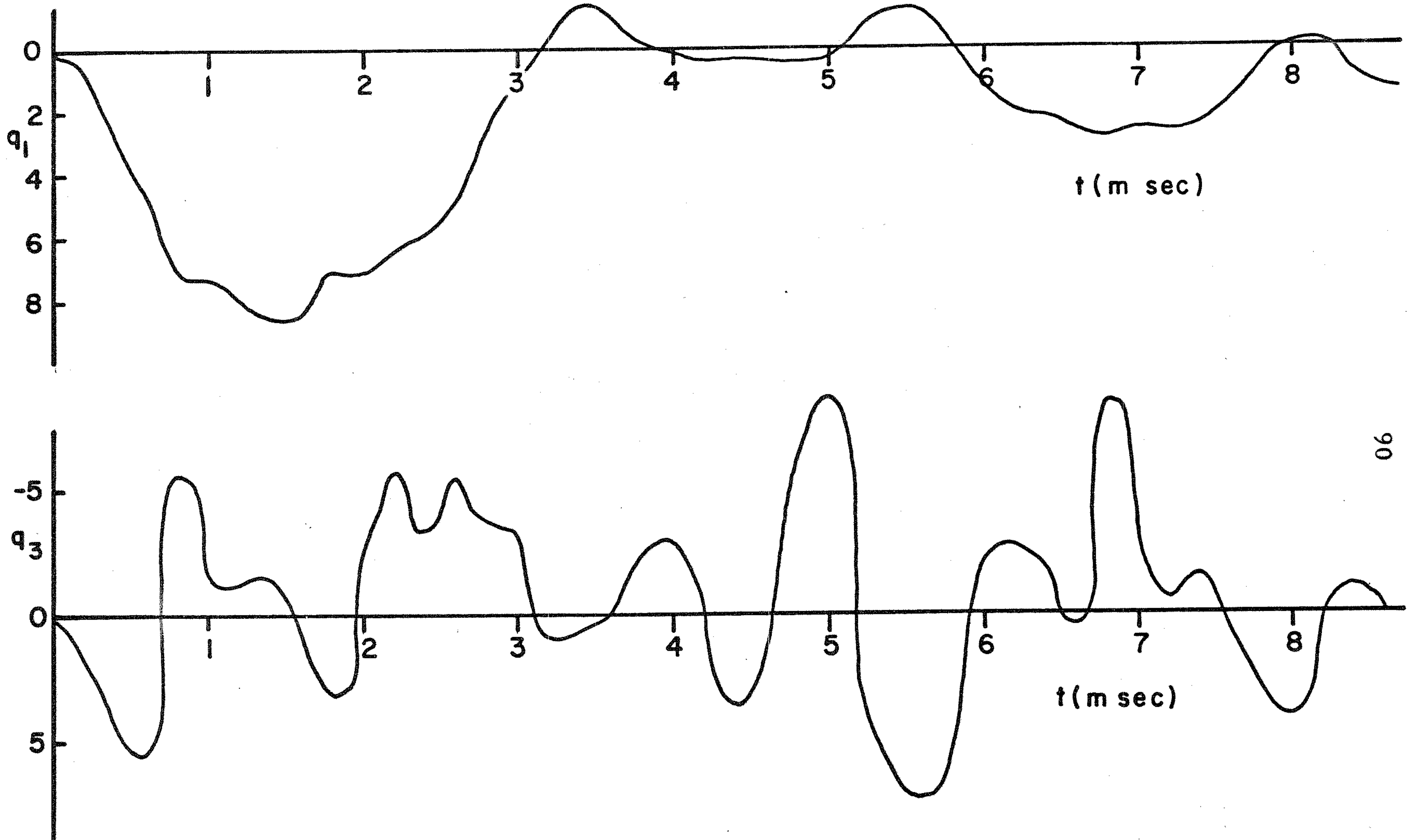

FIG.26d RESPONSE OF ARCH B8, $\overline{I} = 14.82$

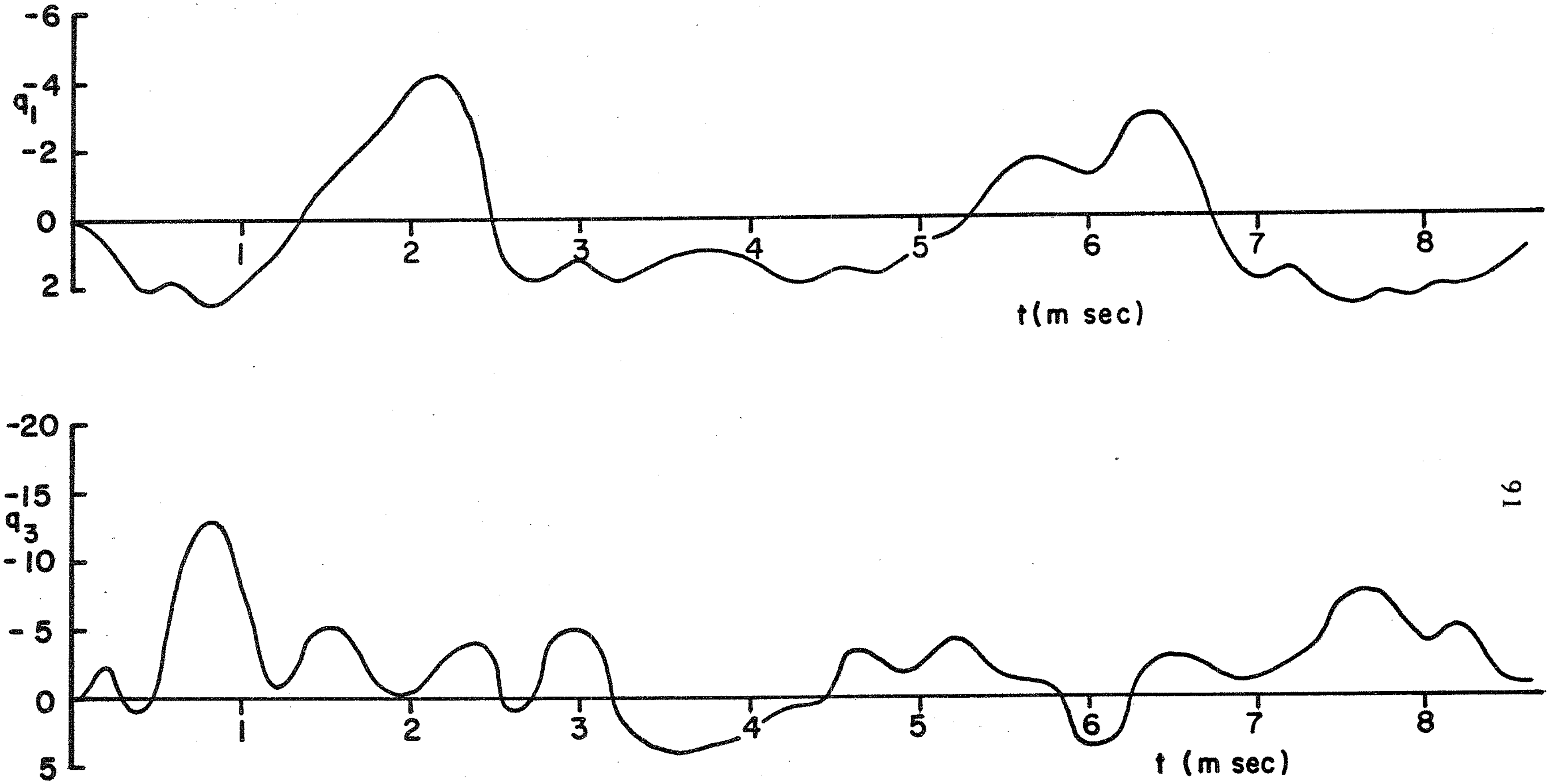

FIG.26e RESPONSE OF ARCH C3, $\overline{I}$ = 12.60

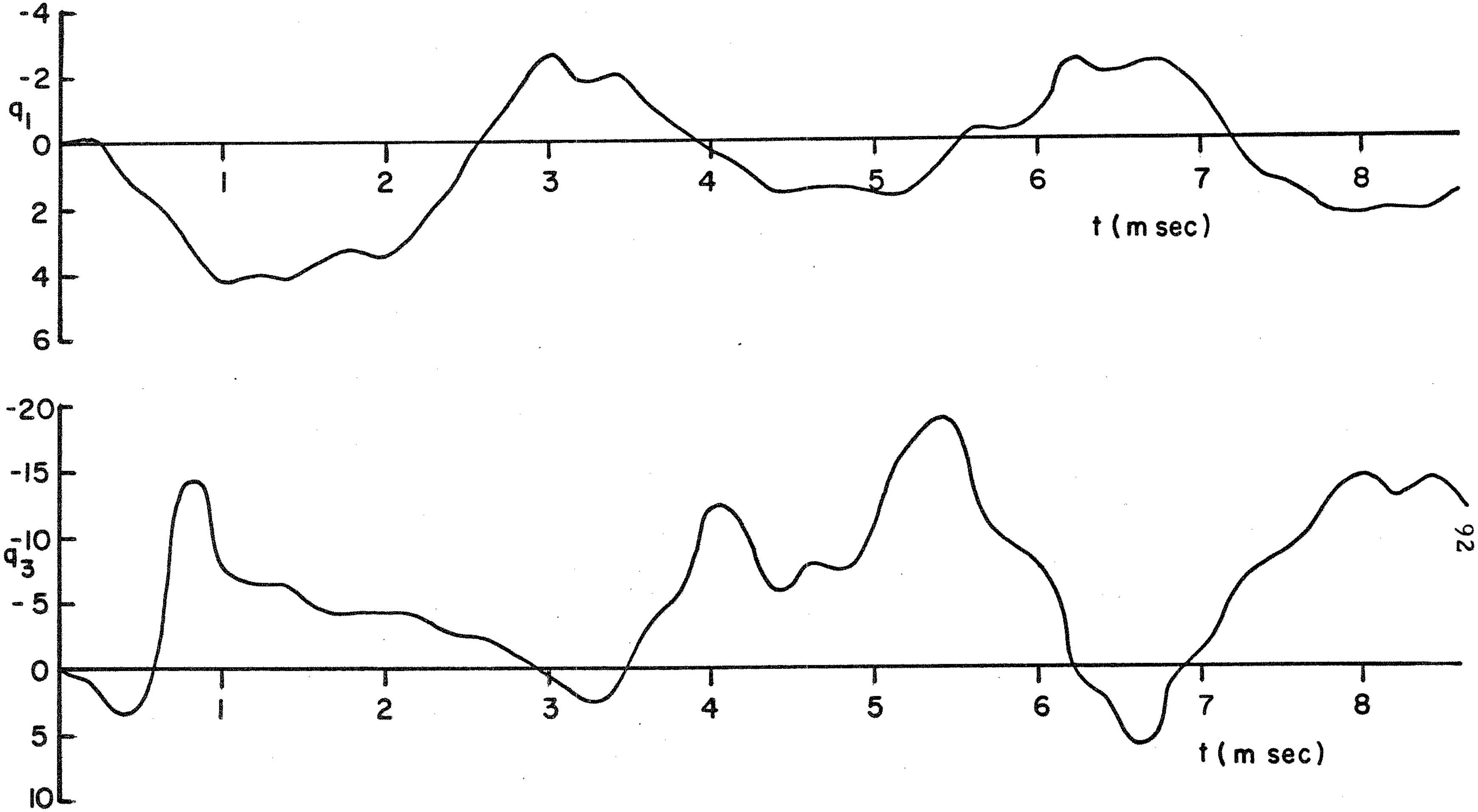

FIG.26f RESPONSE OF ARCH C2, $\overline{I}$ = 15.08

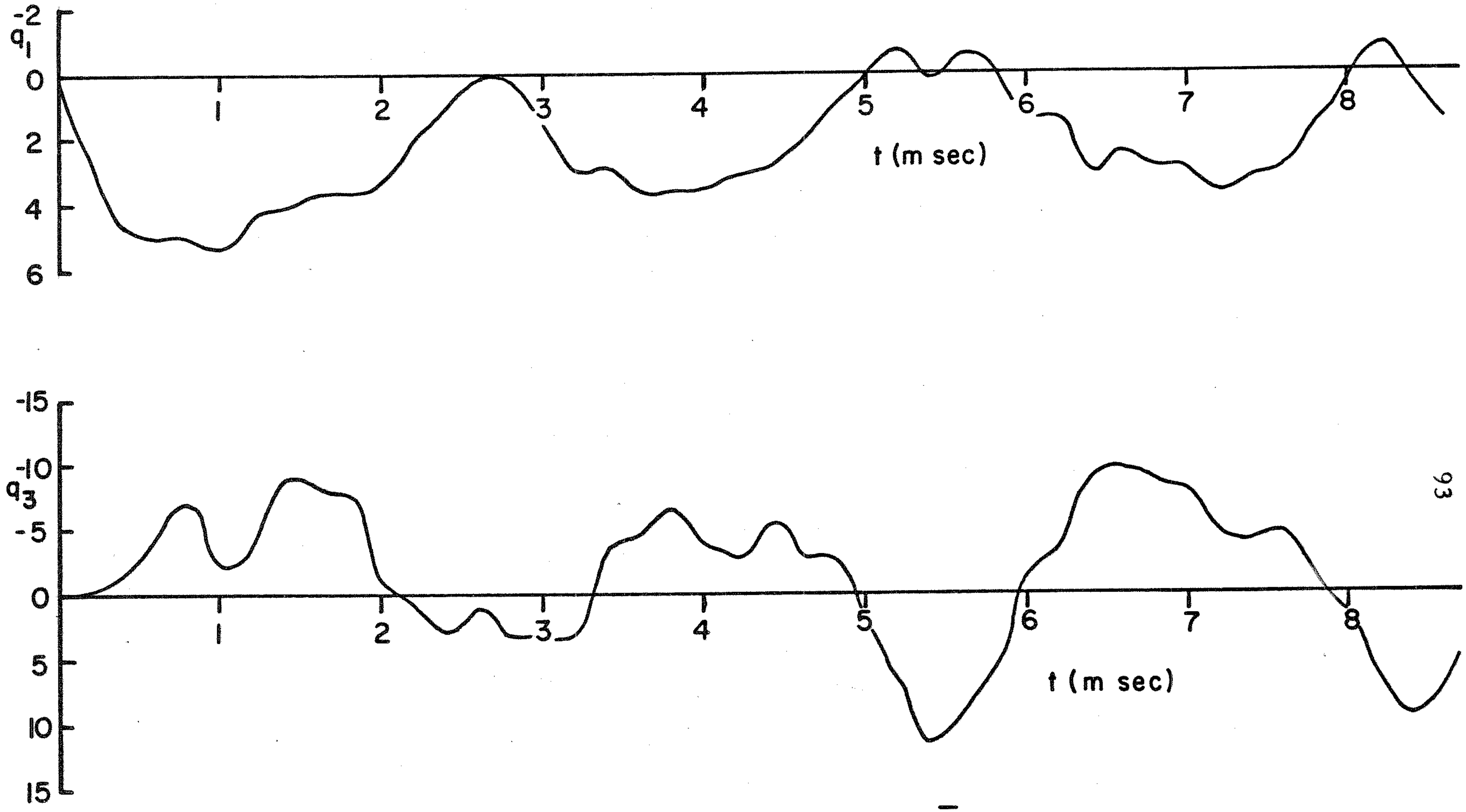

FIG.26g RESPONSE OF ARCH C5, $\overline{I}$ = 16.66

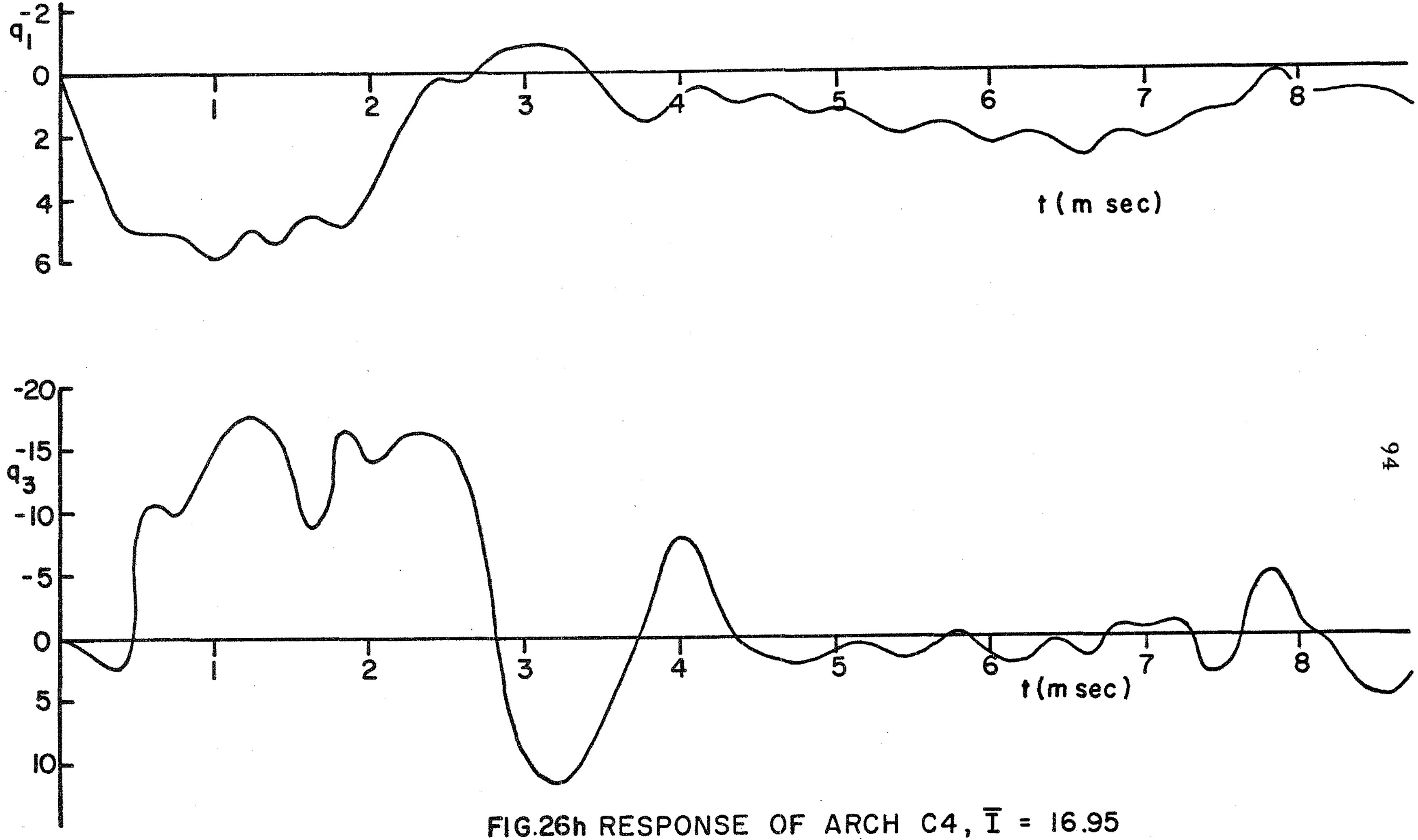

FIG.26h RESPONSE OF ARCH C4, $\overline{I}$ = 16.95

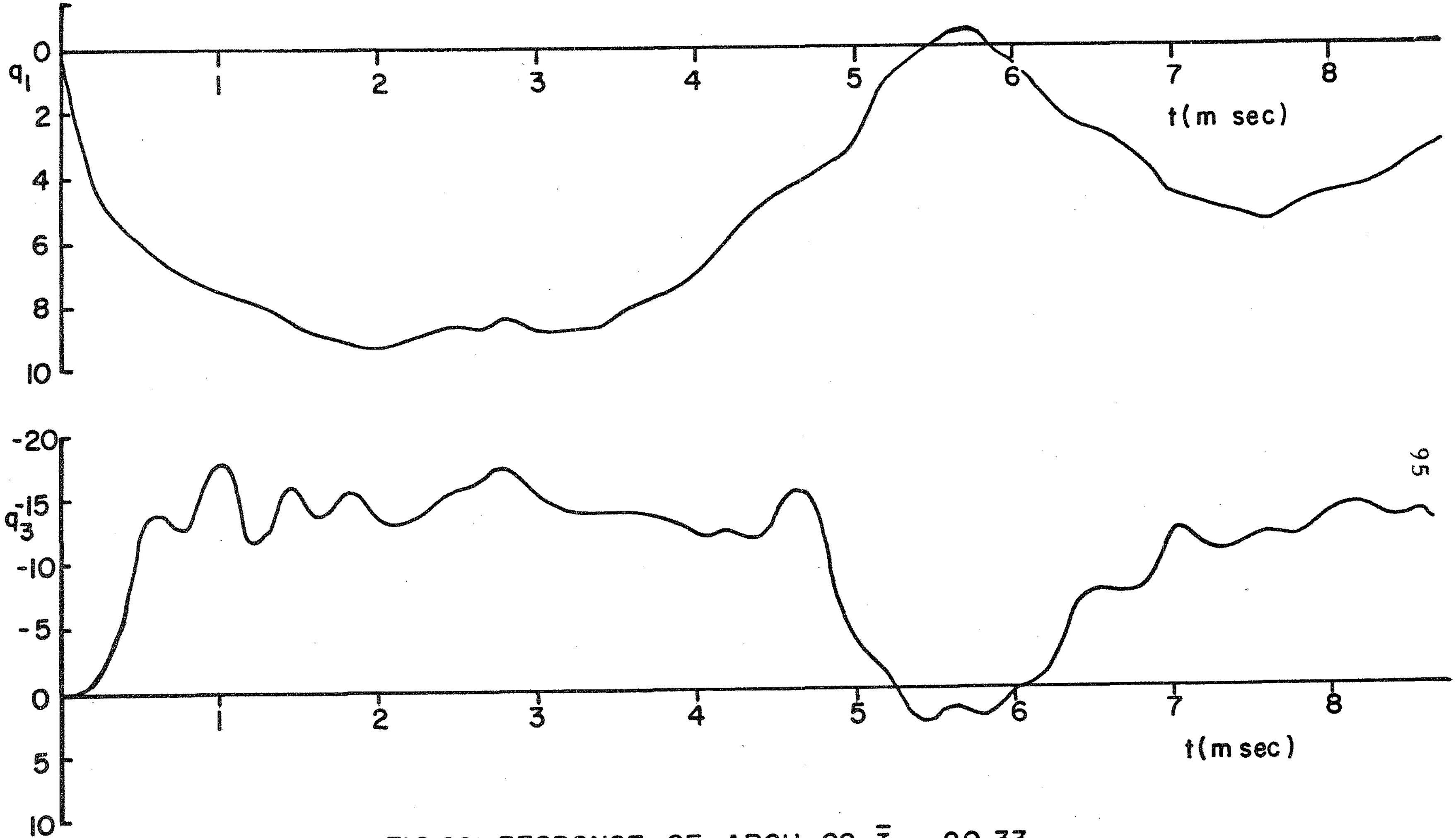

FIG.26i RESPONSE OF ARCH C8, $\bar{I}$ = 20.33

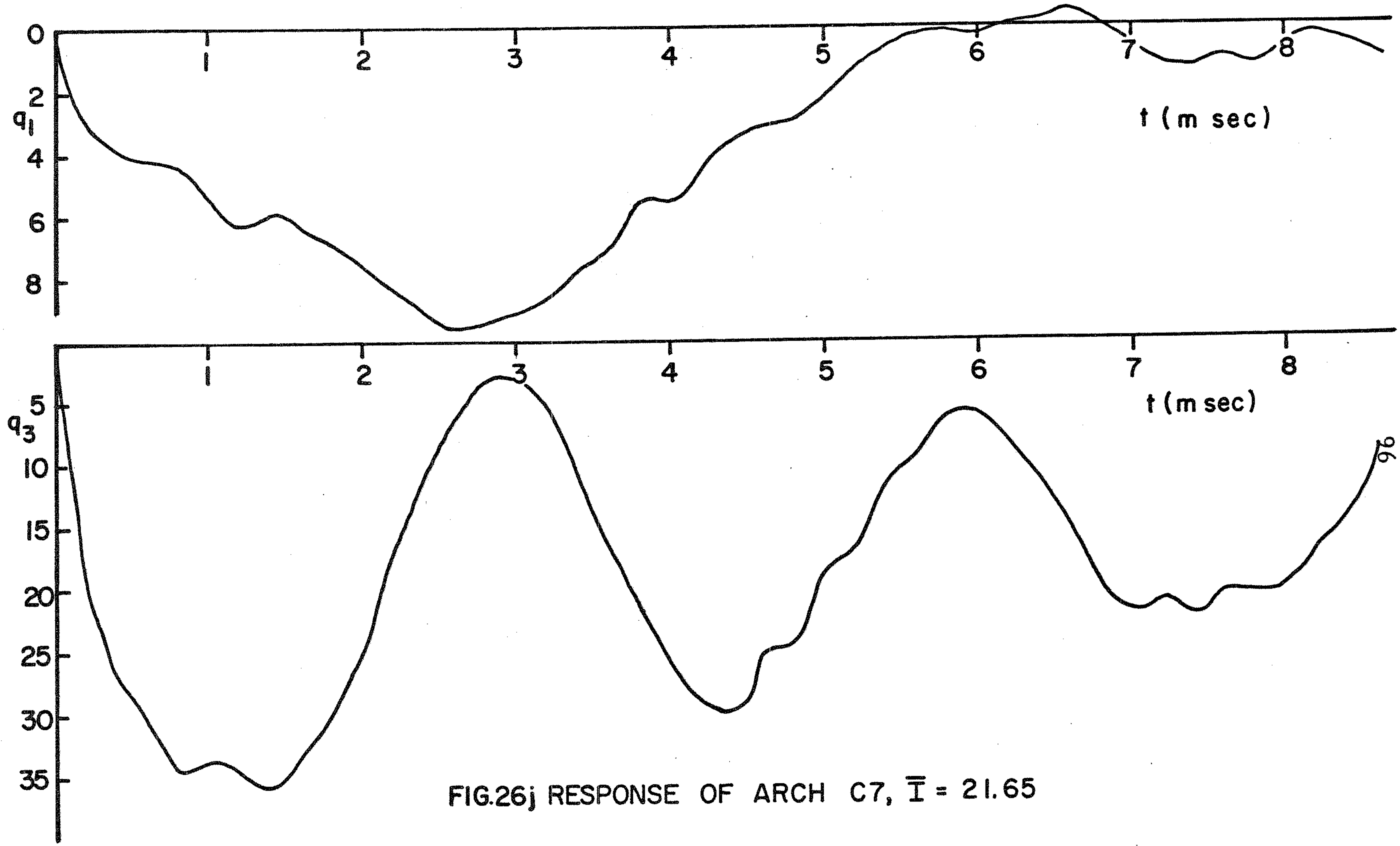

FIG.26j RESPONSE OF ARCH C7, $\overline{I} = 21.65$

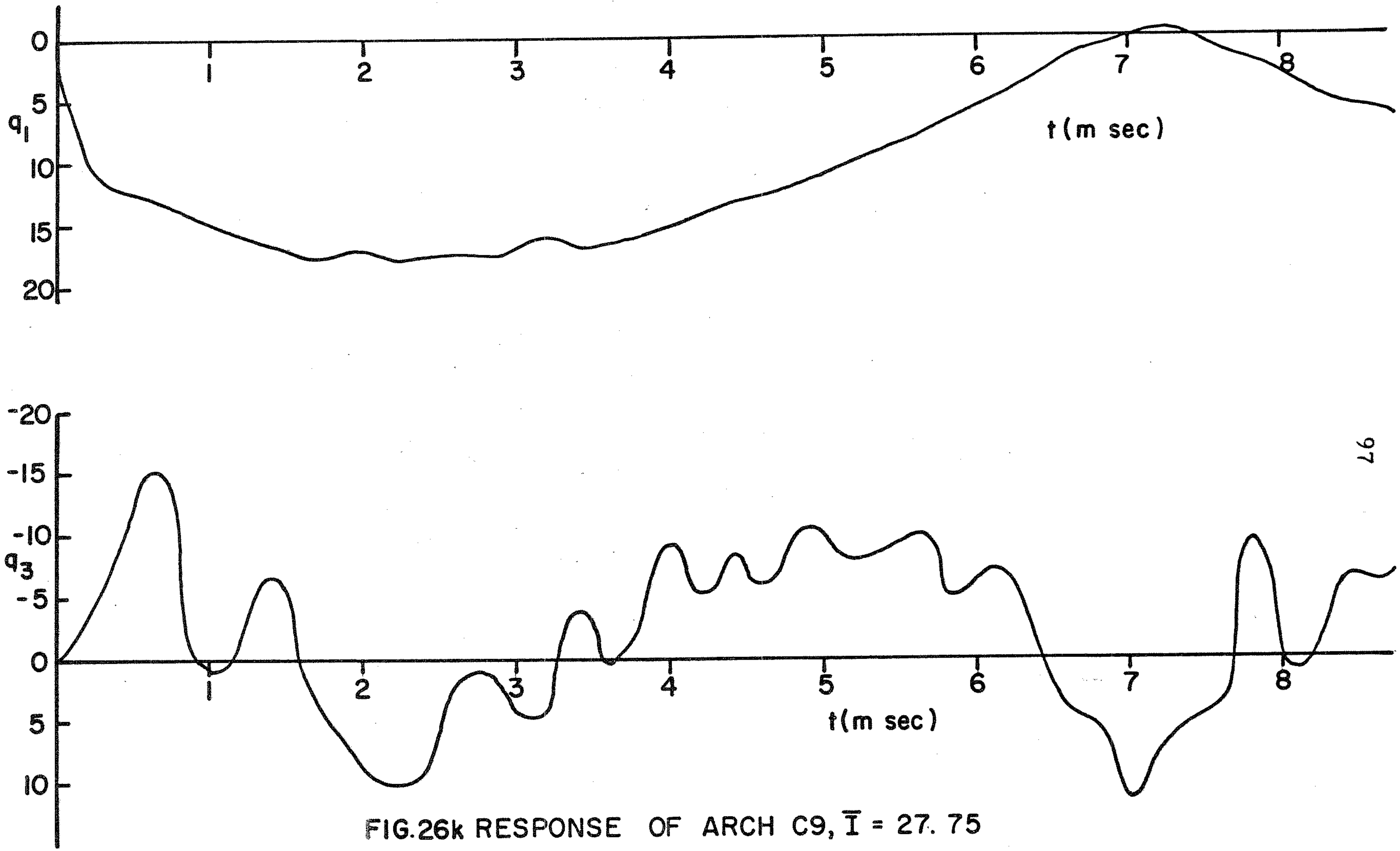

FIG.26k RESPONSE OF ARCH C9, $\overline{I}$ = 27.75

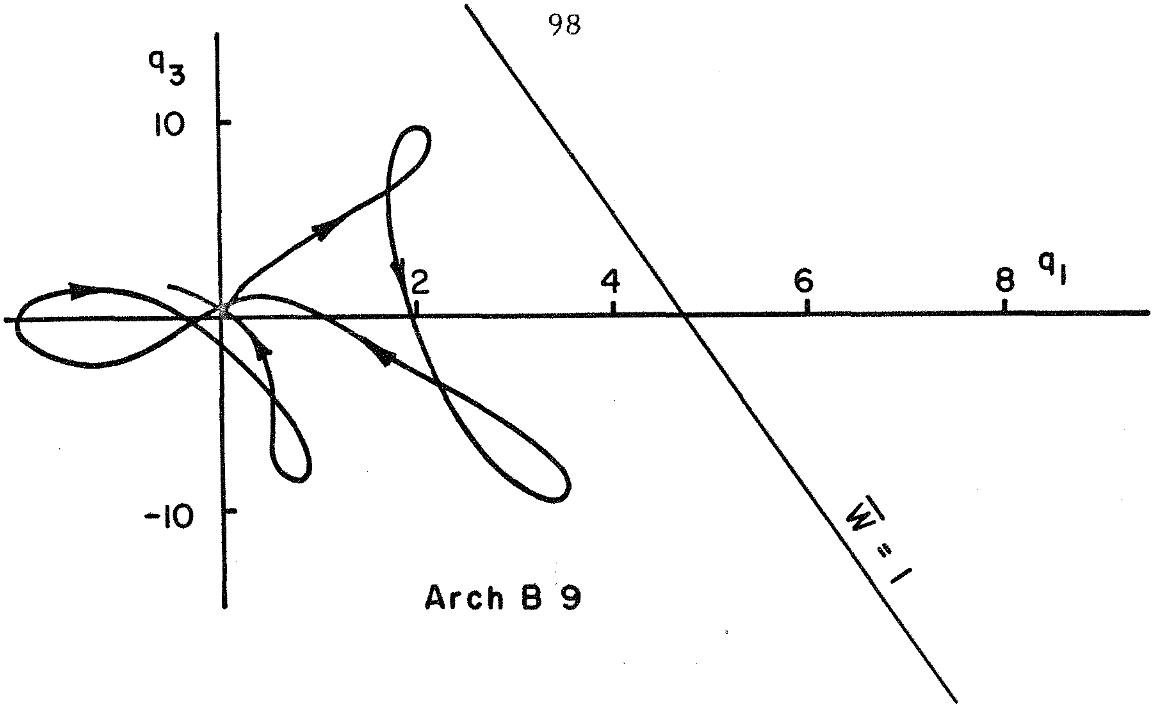

Arch B 9

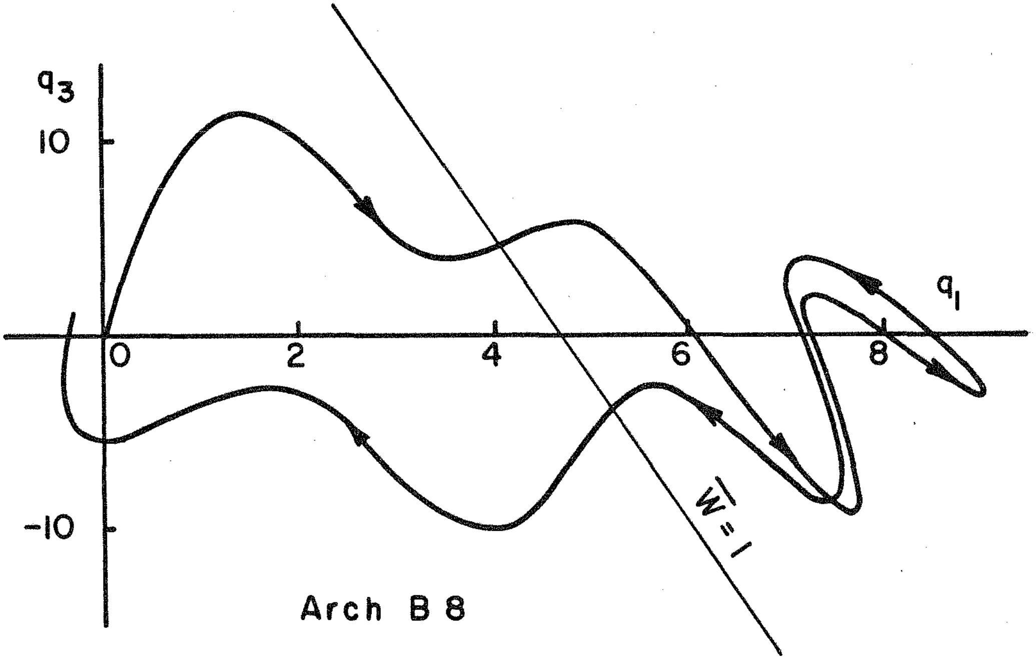

Arch B 8

FIG.27a TRAJECTORIES OF ARCHES FOR $\gamma \approx 10$

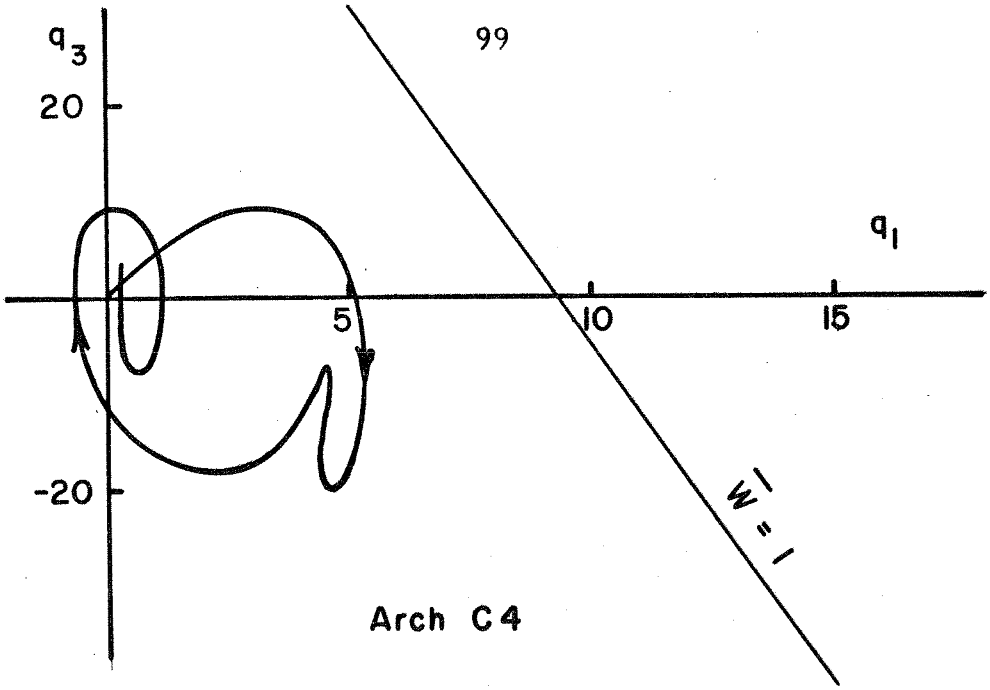

Arch C4

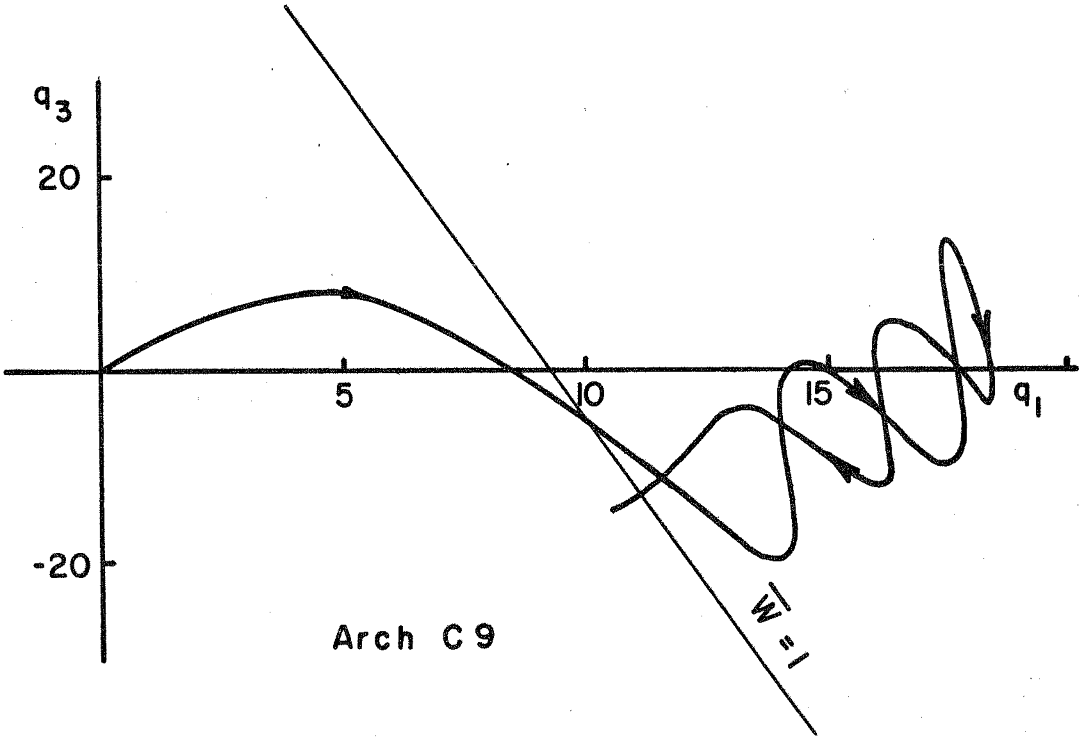

Arch C9

FIG.27b TRAJECTORIES OF ARCHES FOR $\gamma \approx 20$

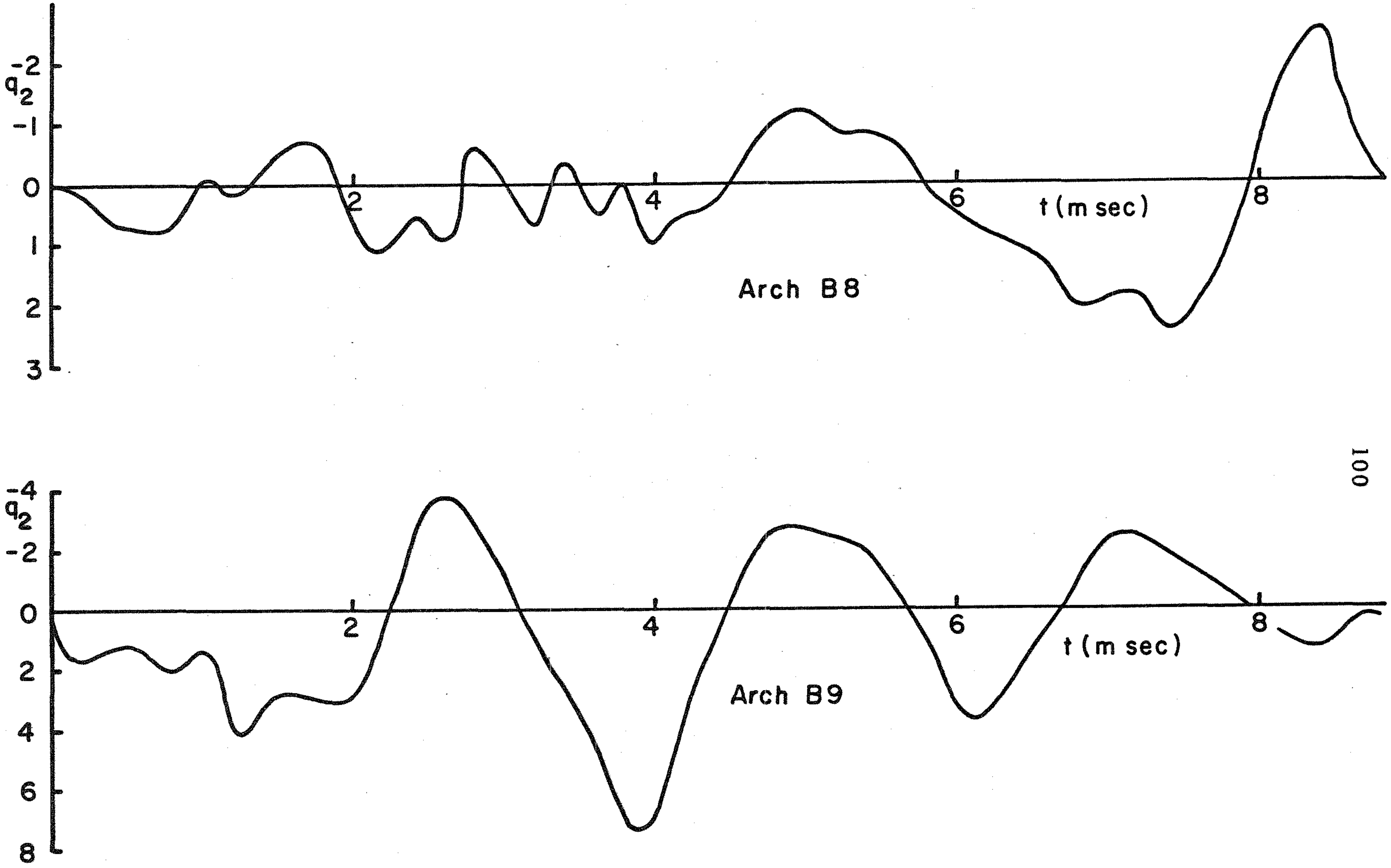

FIG.28a ARCH ANTISYMMETRIC RESPONSE FOR $\gamma \approx 10$

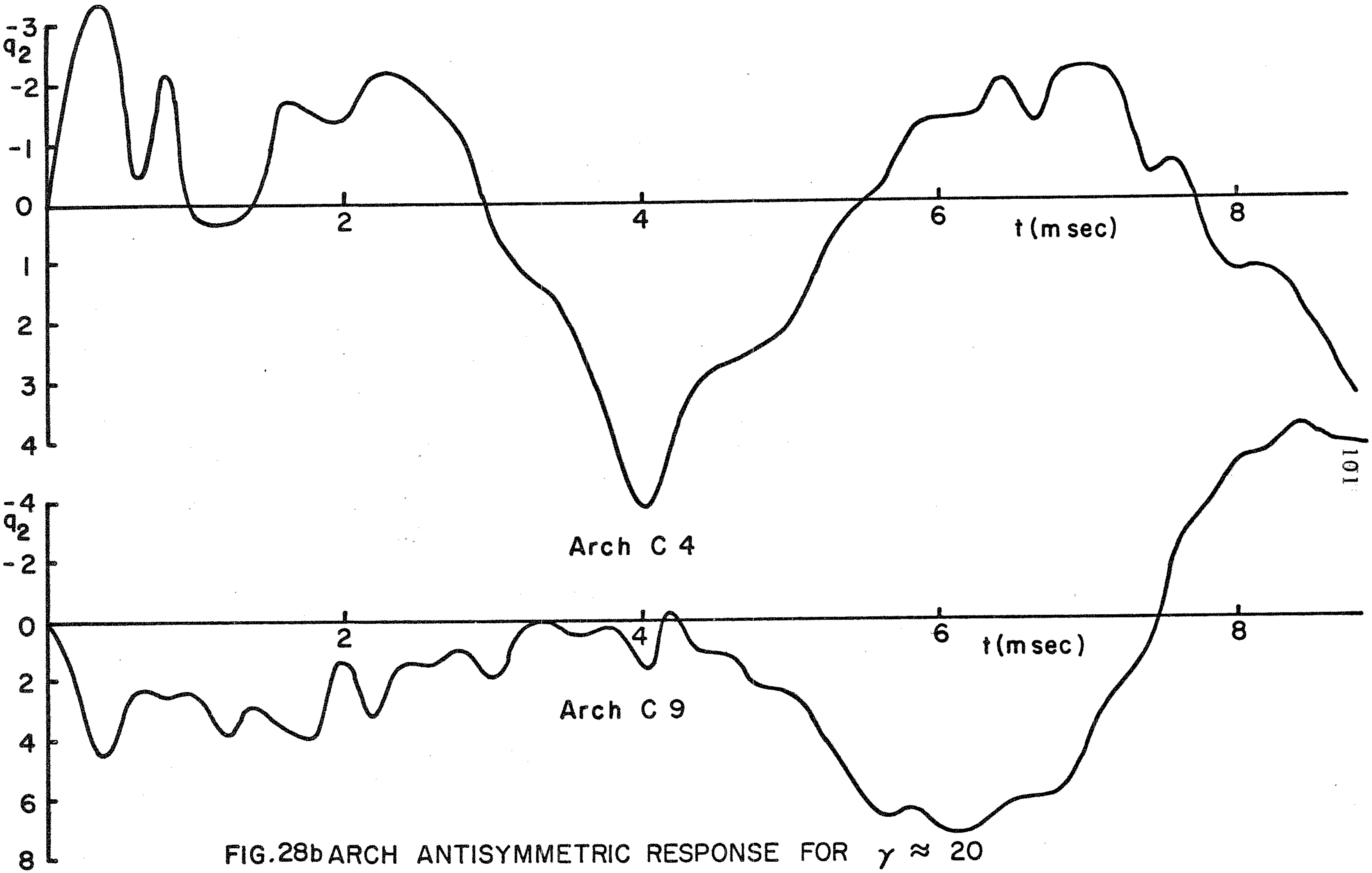

FIG. 28b ARCH ANTISYMMETRIC RESPONSE FOR $\gamma \approx 20$

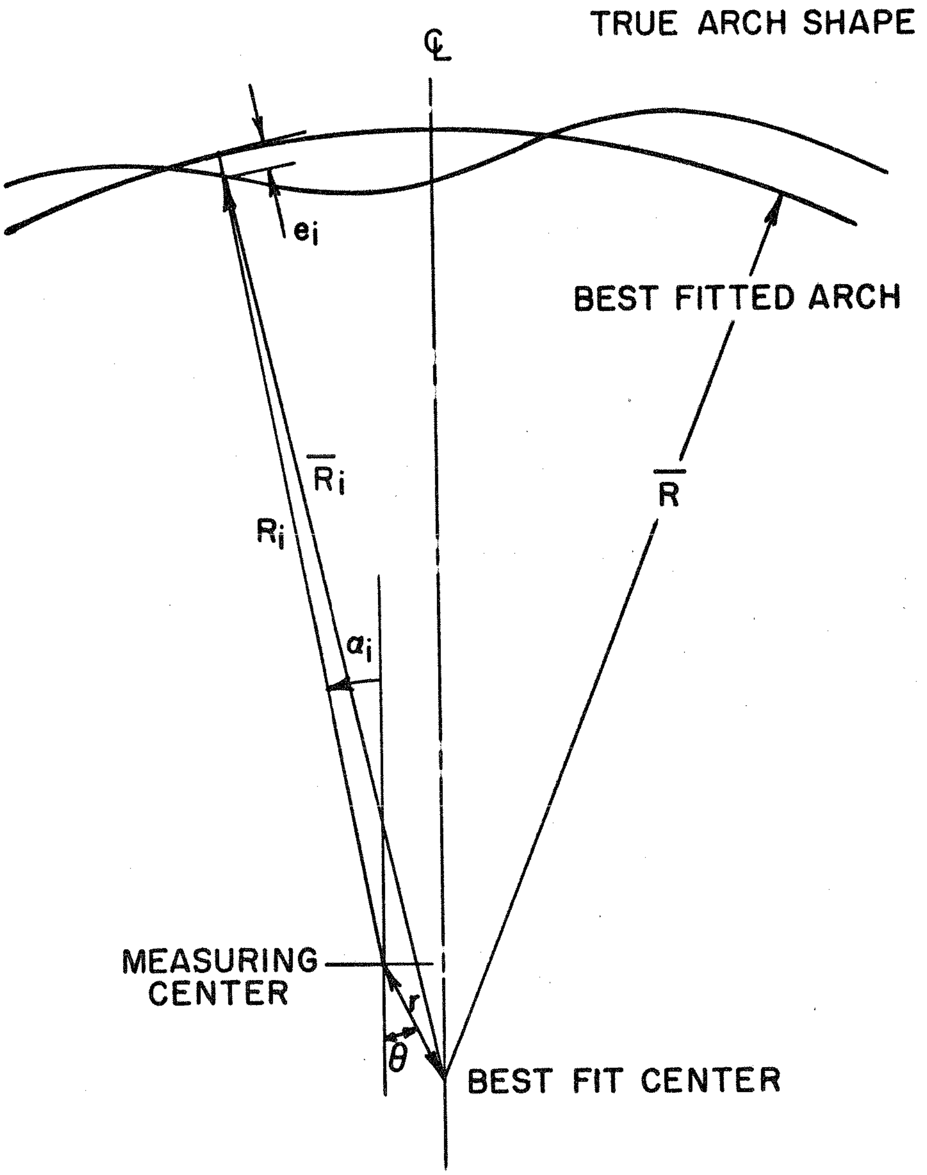

FIG. 29 COORDINATE SYSTEM FOR FINDING BEST FIT TO THE MEASURED INITIAL IMPERFECTIONS

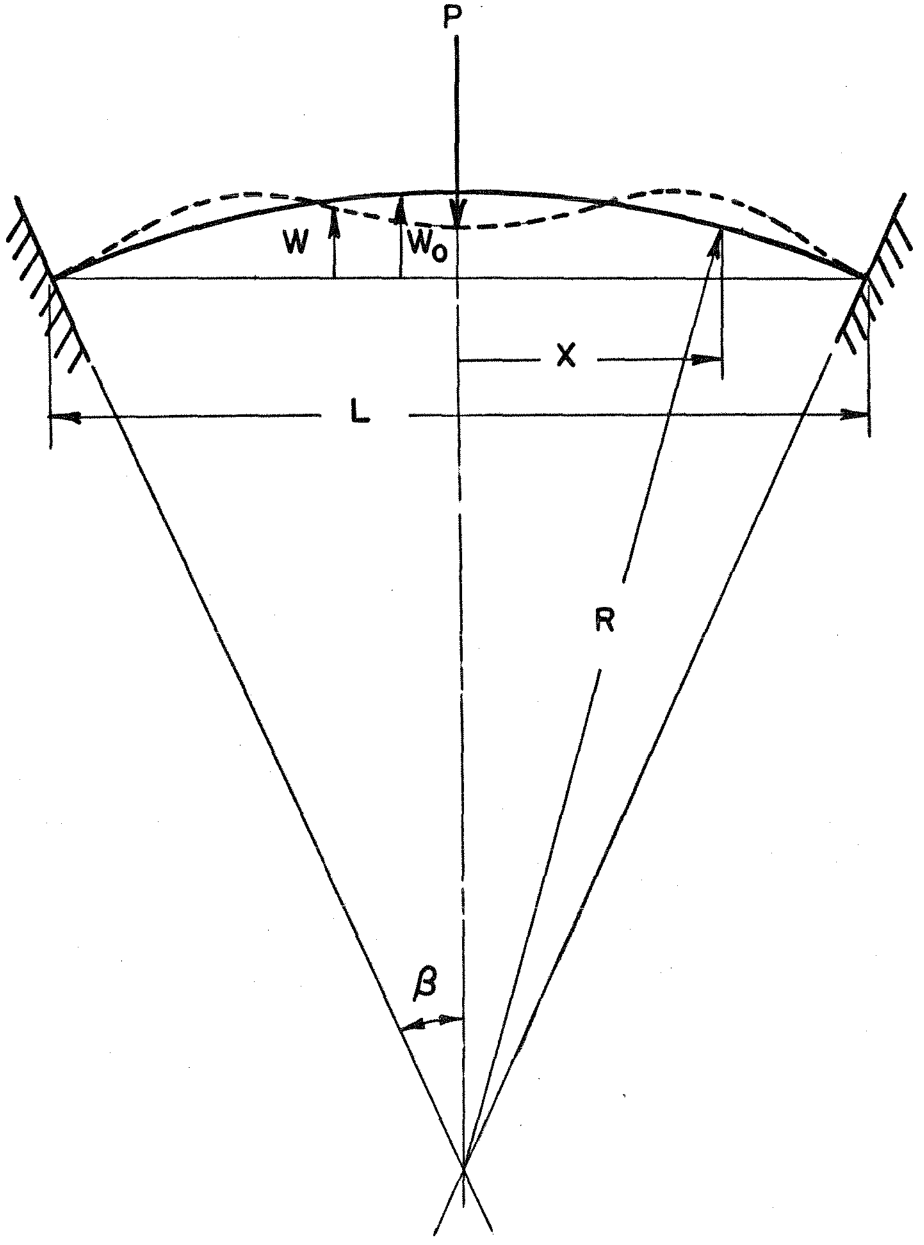

FIG. 30 COORDINATE SYSTEM FOR THE CLAMPED CIRCULAR ARCHES